

CMS-HIG-20-011

CERN-EP-2025-214  
2025/10/10

# Combination of searches for nonresonant Higgs boson pair production in proton-proton collisions at $\sqrt{s} = 13$ TeV

The CMS Collaboration

## Abstract

This paper presents a combination of searches for the nonresonant production of Higgs boson pairs (HH) in proton-proton collisions at a centre-of-mass energy of 13 TeV. The data set was collected by the CMS experiment at the LHC from 2016 to 2018 and corresponds to a total integrated luminosity of  $138 \text{ fb}^{-1}$ . The observed (expected) upper limit on the inclusive HH production cross section relative to the standard model (SM) prediction is found to be 3.5 (2.5). Assuming all other Higgs boson couplings are equal to their SM values, the Higgs boson trilinear self-coupling modifier  $\kappa_\lambda = \lambda_3/\lambda_3^{\text{SM}}$  is constrained in the range  $-1.35 \leq \kappa_\lambda \leq 6.37$  at 95% confidence level. Similarly, for the coupling modifier  $\kappa_{2V}$ , which governs the interaction between two vector bosons and two Higgs bosons, we have excluded  $\kappa_{2V} = 0$  at more than 5 standard deviations for all values of  $\kappa_\lambda$ . At 95% confidence level assuming other couplings are equal to their SM values,  $\kappa_{2V}$  is constrained in the range  $0.64 \leq \kappa_{2V} \leq 1.40$ . This work also studies HH production in several new physics scenarios, using the Higgs effective field theory (HEFT) framework. The HEFT framework is further exploited to study various ultraviolet complete models with an extended Higgs sector and set constraints on specific parameters. An extrapolation of the results to the integrated luminosity expected after the high-luminosity upgrade of the LHC is reported as well.

*Submitted to Reports on Progress in Physics*



## 1 Introduction

In 2012, the ATLAS and CMS Collaborations at the CERN LHC discovered a new particle with a mass of approximately 125 GeV [1–3]. Extensive measurements of its properties, including the mass, spin, parity, couplings to other standard model (SM) particles, and decay width, have revealed that this particle is compatible with the SM Higgs boson ( $H$ ) [4, 5]. However, the question of the Higgs boson self-interaction remains unresolved. Measurements of the Higgs boson trilinear ( $\lambda_3$ ) and quartic self-couplings ( $\lambda_4$ ) provide valuable information about the Brout–Englert–Higgs mechanism, the process by which a complex scalar doublet field—the Higgs doublet—generates the masses of the  $W$  and  $Z$  bosons through spontaneous electroweak (EW) symmetry breaking. The findings will confirm the SM or point to new physics scenarios, such as extended Higgs sectors [6–15]. Beyond particle physics, the true nature of electroweak phase transition will shed light on cosmological questions related to inflation, gravitational waves, and baryogenesis [16–22]. While the quartic coupling is challenging to measure at the LHC and requires future colliders [23–26], the trilinear coupling can be directly accessed by studying Higgs boson pair production.

At the LHC, pairs of SM Higgs bosons ( $HH$ ) are primarily produced via gluon-gluon fusion (ggF), with a cross section of  $31.05^{+0.06}_{-0.23}$  fb [27, 28] at next-to-next-to-leading order (NNLO) in quantum chromodynamics (QCD) for a centre-of-mass energy of 13 TeV and a Higgs boson mass of 125 GeV, which is the assumed value for the studies in this paper. At leading order (LO), two amplitudes contribute to the ggF  $HH$  production cross section, namely the Higgs boson self-interaction ('triangle diagram') and the top quark loop ('box diagram'), represented by the Feynman diagrams in Fig. 1. The triangle diagram amplitude is proportional to the Higgs boson trilinear self-coupling, or in the theoretical framework described in Section 3, to the coupling modifier  $\kappa_\lambda = \lambda_3 / \lambda_3^{\text{SM}}$ , where  $\lambda_3^{\text{SM}}$  is the Higgs boson trilinear self-coupling in the SM. The triangle and box diagram amplitudes interfere destructively, leading to a significant reduction in the ggF cross section for certain values of  $\kappa_\lambda$ .

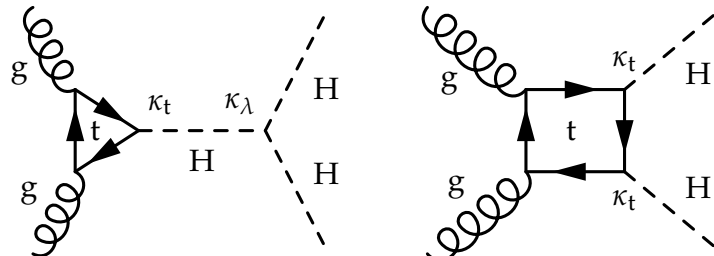


Figure 1: Leading-order Feynman diagrams of nonresonant Higgs boson pair production via gluon-gluon fusion in the SM. The modifiers of the Higgs boson coupling with the top quark and the Higgs boson trilinear self-coupling are shown as  $\kappa_t$  and  $\kappa_\lambda$ , respectively.

The second to largest production mechanism for  $HH$  events is vector boson fusion (VBF) with a cross section of  $1.726 \pm 0.036$  fb [29] in the SM at  $\sqrt{s} = 13$  TeV and next-to-NNLO ( $N^3\text{LO}$ ) in QCD. The VBF production mode, shown in Fig. 2, gives access to the coupling modifier of the interaction between two vector bosons and two Higgs bosons ( $\kappa_{2V}$ ) and the interaction between a Higgs boson and two vector bosons ( $\kappa_V$ ). The characteristic signature of VBF, two jets in the forward direction, with a large pseudorapidity ( $\eta$ ) separation, allows us to identify the process despite the small cross section. Higgs boson pairs can also be produced in association with a vector boson  $V = W$  or  $Z$  (VHH) with a cross section of approximately half that of the VBF mode,  $0.36^{+0.04}_{-0.03}$  fb for  $ZHH$  and  $0.33^{+0.03}_{-0.05}$  fb for  $WHH$ , as shown in Fig. 3. The VHH production is affected differently by the destructive interference compared to ggF and VBF because of the presence of additional diagrams at next-to-LO (NLO), offering complementary constraints on

$\kappa_\lambda$  especially for  $\kappa_\lambda > 0$  [30].

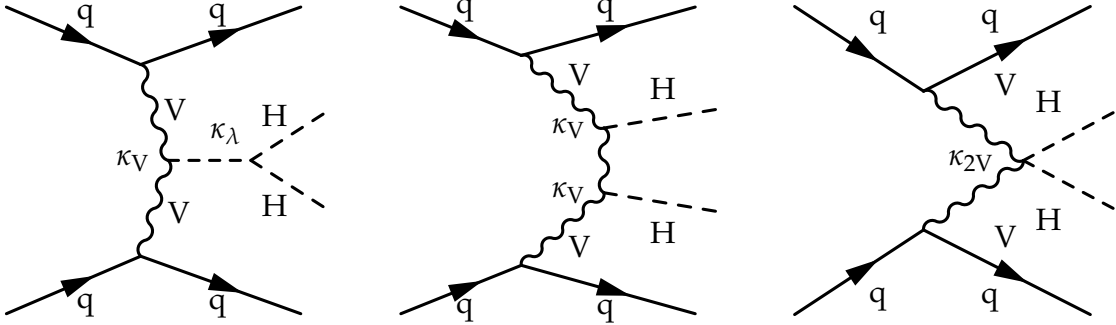


Figure 2: Leading-order Feynman diagrams of nonresonant Higgs boson pair production via vector boson fusion in the SM. The modifiers of the Higgs boson coupling with a vector boson, the Higgs boson trilinear self-coupling, and the coupling between two Higgs bosons and two vector bosons are shown as  $\kappa_V$ ,  $\kappa_\lambda$ , and  $\kappa_{2V}$ , respectively.

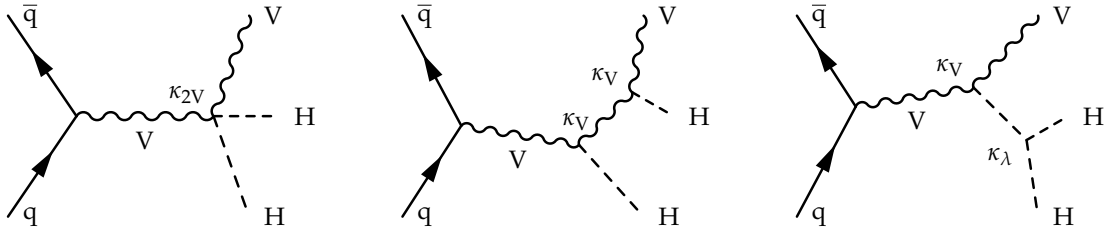


Figure 3: Leading-order Feynman diagrams of nonresonant Higgs boson pair production via associated production with a vector boson in the SM. The modifiers of the Higgs boson coupling with a vector boson, the Higgs boson trilinear self-coupling, and the coupling between two Higgs bosons and two vector bosons are shown as  $\kappa_V$ ,  $\kappa_\lambda$ , and  $\kappa_{2V}$ , respectively.

In new physics models, additional diagrams that include couplings not present in the SM may contribute to  $HH$  production. These can be studied in the context of the Higgs effective field theory (HEFT) [31]. The HEFT Lagrangian extends the SM Lagrangian with additional operators of dimension five or greater that are invariant under  $SU(3)_C \times U(1)_{EM}$  and their corresponding couplings. The anomalous couplings studied in this paper are denoted  $c$  and shown in Fig. 4. Here,  $c_2$  corresponds to the coupling between two top quarks and two Higgs bosons,  $c_g$  to the coupling between a Higgs boson and two gluons, and  $c_{2g}$  to the coupling between two Higgs bosons and two gluons. The HEFT Lagrangian as a function of the anomalous coupling modifiers is:

$$\Delta\mathcal{L}_{\text{HEFT}} = -m_t \left( \kappa_t \frac{h}{v} + c_2 \frac{h^2}{v^2} \right) \bar{t}t - \kappa_\lambda \frac{m_H^2}{2v} h^3 + \frac{\alpha_S}{8\pi} \left( c_g \frac{h}{v} + c_{2g} \frac{h^2}{v^2} \right) G_{\mu\nu}^a G^{a,\mu\nu}. \quad (1)$$

The ATLAS and CMS Collaborations have performed previous  $HH$  searches at  $\sqrt{s} = 8$  and 13 TeV. The ATLAS Collaboration has combined  $HH$  searches in the  $b\bar{b}\gamma\gamma$ ,  $b\bar{b}\tau\tau$ , and  $b\bar{b}b\bar{b}$  final states at 13 TeV and set an upper limit on the inclusive production cross section of 2.9 times the SM expectation at 95% confidence level (CL), with 2.4 expected under the background-only hypothesis [32]. A combined search in the  $b\bar{b}\gamma\gamma$ ,  $b\bar{b}\tau\tau$ ,  $b\bar{b}b\bar{b}$ ,  $b\bar{b}ZZ$ , and multilepton final states by CMS at 13 TeV constrained (expected to constrain) the inclusive  $HH$  production cross section to less than 3.4 (2.5) times the SM expectation at 95% CL [4]. This paper supersedes

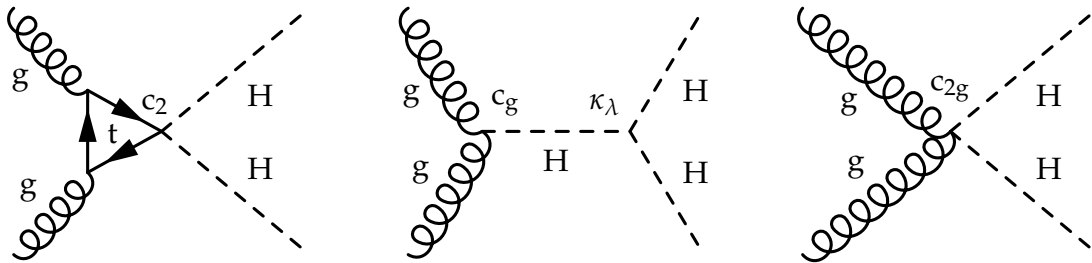


Figure 4: Leading-order Feynman diagrams of nonresonant Higgs boson pair production via gluon-gluon fusion with anomalous Higgs boson couplings  $c_2$ ,  $c_g$ , and  $c_{2g}$ . The Higgs boson trilinear self-coupling modifier is shown as  $\kappa_\lambda$ .

previous results by introducing additional channels, including the  $b\bar{b}WW$ ,  $WW\gamma\gamma$ , and  $\tau\tau\gamma\gamma$  final states and VHH production mode in the  $b\bar{b}b\bar{b}$  final state, to perform a variety of parameter scans, as well as searches for anomalous Higgs boson couplings in the HEFT approach. The HEFT parametrisation is further exploited to constrain parameters in specific ultraviolet (UV) complete models. The results presented in this paper and provided in the corresponding HEP-Data record [33] are based on the data set of proton-proton (pp) collisions at 13 TeV collected by the CMS experiment from 2016 to 2018 (Run 2), corresponding to an integrated luminosity of  $138 \text{ fb}^{-1}$ .

## 2 The CMS detector and event reconstruction

The CMS apparatus [34, 35] is a multipurpose, nearly hermetic detector, designed to trigger on [36–38] and identify electrons, muons, photons, and (charged and neutral) hadrons [39–41]. Its central feature is a superconducting solenoid of 6 m internal diameter, providing a magnetic field of 3.8 T. Within the solenoid volume are a silicon pixel and strip tracker, a lead tungstate crystal electromagnetic calorimeter (ECAL), and a brass and scintillator hadron calorimeter (HCAL), each composed of a barrel and two endcap sections. Forward calorimeters extend the pseudorapidity coverage provided by the barrel and endcap detectors. Muons are reconstructed using gas-ionisation detectors embedded in the steel flux-return yoke outside the solenoid. More detailed descriptions of the CMS detector, together with a definition of the coordinate system used and the relevant kinematic variables, can be found in Refs. [34, 35].

Events of interest are selected using a two-tiered trigger system. The first level, composed of custom hardware processors, uses information from the calorimeters and muon detectors to select events at a rate of around 100 kHz within a fixed latency of  $4 \mu\text{s}$  [36]. The second level, known as the high-level trigger, consists of a farm of processors running a version of the full event reconstruction software optimised for fast processing, and reduces the event rate to a few kHz before data storage [37, 38].

A particle-flow (PF) algorithm [42] aims to reconstruct and identify each particle in an event (PF candidate), with an optimised combination of information from the various elements of the CMS detector. The primary vertex (PV) is taken to be the vertex corresponding to the hardest scattering in the event, evaluated using tracking information alone, as described in Section 9.4.1 of Ref. [43]. The energy of photons is obtained from the ECAL measurement. The energy of electrons is determined from a combination of the track momentum at the PV the corresponding ECAL cluster energy, and the energy sum of all bremsstrahlung photons attached to the track. The momentum of muons is obtained from the curvature of the corresponding track. The energy of charged hadrons is determined from a combination of the track momentum and the corresponding ECAL and HCAL energies, corrected for the response function of

the calorimeters to hadronic showers. Finally, the energy of neutral hadrons is obtained from the corresponding corrected ECAL and HCAL energies.

Small-radius jets are reconstructed from PF candidates, using the anti- $k_T$  clustering algorithm [44, 45] with a distance parameter  $R = 0.4$  (AK4 jets). Charged particles not originating from the PV are excluded from the jet clustering, and an offset correction is applied to correct for remaining contributions. Higgs boson decays into a pair of b quarks with high transverse momentum ( $p_T$ ) result in final states with large Lorentz boost, and as a result, the b jets are overlapping, forming one large merged jet (“large-radius jet”) and substructure, i.e., the two overlapping jets are “subjets” of the large-radius jet. The jets are reconstructed using the anti- $k_T$  algorithm with a distance parameter  $R = 0.8$  (AK8 jets).

The missing transverse momentum vector  $\vec{p}_T^{\text{miss}}$  is computed as the negative vector  $p_T$  sum of all the PF candidates in an event, and its magnitude is denoted as  $p_T^{\text{miss}}$  [46]. The  $\vec{p}_T^{\text{miss}}$  is modified to account for corrections to the energy scale of the reconstructed jets in the event.

The searches presented in this paper use a variety of object identification techniques and algorithms, tailored to their specific characteristics.

### 3 Signal modelling

The dependence of the ggF HH cross section on  $\kappa_\lambda$  and  $\kappa_t$  can be written as

$$\sigma(\kappa_\lambda, \kappa_t) = \kappa_\lambda^2 \kappa_t^2 t + \kappa_t^4 b + \kappa_\lambda \kappa_t^3 i, \quad (2)$$

where  $t = |T|^2$ ,  $b = |B|^2$ , and  $i = |TB^* + B^*T|$ , are the three amplitudes that correspond to the triangle and box diagrams shown in Fig. 1, and their interference, respectively [47].

The same formula holds for every differential cross section  $d\sigma/dx$  for ggF HH production. At higher order in the QCD perturbative expansion,  $T$  and  $B$  correspond to the sum of all diagrams of the same order in  $\kappa_\lambda$  and  $\kappa_t$ , and the polynomial relation in Eq. (2) remains valid. Since the ggF cross section can be expressed as a polynomial in  $\kappa_\lambda$  and  $\kappa_t$  with three independent terms, we can model the ggF signal over a wide range of  $\kappa_\lambda$  and  $\kappa_t$  by evaluating the cross section at three different combinations of values for  $(\kappa_\lambda, \kappa_t)$ , namely (1, 1), (2.45, 1) and (5, 1), and performing a linear combination. In our case, we use the information from three simulated data samples for the linear combination and that allows us to perform scans in the  $\kappa_\lambda$  and  $\kappa_t$  parameters.

In order to study modified values for the SM couplings as well as couplings not present in the SM we use an event-level reweighting method. The reweighting is based on a parameterisation of the differential cross section as a function of the generator-level invariant mass of the HH system and the angular distance between the two Higgs bosons in the azimuthal plane, which are sufficient to characterise the hard scattering as it only has two degrees of freedom. This allows modelling any combination of coupling modifiers  $(\kappa_\lambda, \kappa_t, c_2, c_g, c_{2g})$  present in the  $\Delta\mathcal{L}_{\text{HEFT}}$  (1), even for values that are not used in the sample generation. The method used to derive the reweighting factors is described in Refs. [48, 49]. The procedure is similar to the recommendation by the LHC Higgs Working Group 4 [31]. In our derivation, we use finer bins for high values of the invariant mass of the HH system. The method is used for all HH decay channels except the  $b\bar{b}b\bar{b}$  channel with high Lorentz boost, where the reweighting factors are not precise enough because of the limited number of simulated events in the high  $m_{\text{HH}}$  bins. Therefore, all necessary Monte Carlo (MC) simulated samples for each benchmark are produced.

Two sets of benchmarks are produced using the reweighting method. The first set defines thirteen benchmark scenarios [50] spanning a broad range of the coupling values in the HEFT parameterisation at LO precision, noted as JHEP04(2016)126. The second set [51], noted as JHEP03(2020)091, was derived with NLO precision and considers direct and indirect constraints on the allowed range for the coupling values. The aim of both sets of benchmarks is to sample the parameter space describing the signal according to kinematic features of the final state. The values of the coupling modifiers corresponding to each benchmark are shown in Tables 1 and 2.

We further study the  $c_2$  modifier and perform scans with  $c_2$  as the parameter of interest. While  $c_2$ ,  $\kappa_t$ , and  $\kappa_\lambda$  are free parameters in the HEFT Lagrangian it is of interest to check for correlations.

Finally, constraints are set on specific UV complete models. The parameters of each model can be written in terms of  $\kappa_\lambda$ ,  $\kappa_t$ , and  $c_2$  based on a mapping described in Ref. [49]. Three types of models are studied in this paper: models with one additional scalar [6, 7], models with two Higgs doublets (2HDM) [8–11], and composite Higgs models [12–15].

The scans in the parameters of interest  $\kappa_\lambda$ ,  $\kappa_t$ ,  $\kappa_V$ , and  $\kappa_{2V}$  are performed using a linear combination of a set of VBF and VHH samples, similar to what is done for ggF. Modifications of Higgs boson couplings to other particles that affect HH and single Higgs boson production are taken into account in all cases [52].

The simulated events for ggF production are produced using NLO matrix elements with the model described in Ref. [47], implemented in POWHEG v2 [53–55]. The cross section is corrected to the NNLO value as a function of  $\kappa_\lambda$  according to Refs. [30, 56]. Four ggF samples are produced with different values of the trilinear coupling modifier ( $\kappa_\lambda = 0, 2.45, 5.0$ , and  $1.0$ ). The simulated signal samples for VBF and VHH production modes are generated at LO using MADGRAPH5\_aMC@NLO 2.6.5 [57–59]. Seven VBF samples are generated with different values of the coupling modifiers  $(\kappa_V, \kappa_{2V}, \kappa_\lambda) = (1, 1, 1), (1, 1, 0), (1, 1, 2), (1, 0, 1), (1, 2, 1), (0.5, 1, 1)$ , and  $(1.5, 1, 1)$ , and eight VHH samples are generated with the same coupling modifier values plus  $(\kappa_V, \kappa_{2V}, \kappa_\lambda) = (1, 1, 20)$ . This last benchmark is used in the VHH case where  $\kappa_\lambda$  is less constrained, therefore we need to model large values of  $\kappa_\lambda$ . The total cross section is corrected to the corresponding NNLO cross section [60, 61]. The parton shower and hadronisation are simulated with PYTHIA 8.230 [62] using the CUETP8M1 set of tuned parameters for 2016 simulations and the CP5 tune set in 2017 and 2018 simulations. The simulated samples produced by PYTHIA with the CUETP8M1 tune use the NNPDF3.0 parton distribution functions (PDFs), whereas the samples produced with the CP5 tune use the NNPDF3.1 set [63–65]. Finally, the samples produced by MADGRAPH5\_aMC@NLO and POWHEG v2, use the NNPDF3.1 set. The response of the CMS detector is modelled using the GEANT4 toolkit [66].

Table 1: Values of the effective Lagrangian couplings for the Higgs effective field theory benchmarks proposed in Ref. [50] and referred to in this paper as JHEP04(2016)126.

	1	2	3	4	5	6	7	8	9	10	11	12	8a
$\kappa_\lambda$	7.5	1.0	1.0	-3.5	1.0	2.4	5.0	15.0	1.0	10.0	2.4	15.0	1.0
$\kappa_t$	1.0	1.0	1.0	1.5	1.0	1.0	1.0	1.0	1.0	1.5	1.0	1.0	1.0
$c_2$	-1.0	0.5	-1.5	-3.0	0.0	0.0	0.0	0.0	1.0	-1.0	0.0	1.0	0.5
$c_g$	0.0	-0.8	0.0	0.0	0.8	0.2	0.2	-1.0	-0.6	0.0	1.0	0.0	0.27
$c_{2g}$	0.0	0.6	-0.8	0.0	-1.0	-0.2	-0.2	1.0	0.6	0.0	-1.0	0.0	0.0

Table 2: Values of the effective Lagrangian couplings for the Higgs effective field theory benchmarks proposed in Ref. [51] and referred to in this paper as JHEP03(2020)091.

	1	2	3	4	5	6	7
$\kappa_\lambda$	3.94	6.84	2.21	2.79	3.95	5.68	-0.10
$\kappa_t$	0.94	0.61	1.05	0.61	1.17	0.83	0.94
$c_2$	-0.33	0.33	-0.33	0.33	-0.33	0.33	1.0
$c_g$	0.75	0.0	0.75	-0.75	0.25	-0.75	0.25
$c_{2g}$	-1	1	-1.5	-0.5	1.5	-1	1

## 4 Analysis strategy

The list of HH analyses considered in this combination, along with a summary of results, are listed in Table 3. A brief description of each analysis is given later in this section. More details can be found in the respective publications. For the purposes of this combination, extensive studies were performed in order to avoid double counting of events among the different analysis. Specific actions taken by the various analyses are described in each section. Two channels,  $b\bar{b}WW$ ,  $WW \rightarrow 4q$  and  $WW\gamma\gamma$ , have not been previously published, and therefore more details are provided in the corresponding sections. The  $b\bar{b}WW$  analysis is the first search for  $HH \rightarrow b\bar{b}WW$  in the all-hadronic final state.

Table 3: Summary of results for the HH analyses included in this combination. The second column is the observed (expected) 95% CL upper limit on the inclusive signal strength  $\mu = \sigma_{HH}/\sigma_{HH}^{SM}$ , with one exception where  $\mu_{VHH} = \sigma_{VHH}/\sigma_{VHH}^{SM}$  is shown. The third (fourth) column is the allowed 68% CL interval for the coupling modifier  $\kappa_\lambda$  ( $\kappa_{2V}$ ). The last column indicates whether the analysis is included in the results using the HEFT parametrisation.

Analysis	$\mu$	$\kappa_\lambda$	$\kappa_{2V}$	HEFT
$b\bar{b}bb$ , resolved jets [67]	3.9 (7.8)	[-2.3, 9.4]	[-0.1, 2.2]	✓
$b\bar{b}bb$ , merged jets [68]	9.9 (5.1)	[-9.9, 16.9]	[0.62, 1.41]	✓
$VHH$ , $HH \rightarrow b\bar{b}bb$ [69]	$\mu_{VHH} < 294$ (124)	[-37.7, 37.2]	[-12.2, 8.9]	—
$b\bar{b}\tau\tau$ [70]	3.3 (5.2)	[-1.7, 8.7]	[-0.4, 2.6]	✓
$b\bar{b}\gamma\gamma$ [71]	7.7 (5.2)	[-3.3, 8.5]	[-1.3, 3.5]	✓
$b\bar{b}WW$ , $WW \rightarrow \ell\nu qq/2\ell 2\nu$ [72]	14 (18)	[-7.2, 13.8]	[-8.7, 15.2]	✓
$b\bar{b}WW$ , $WW \rightarrow 4q$	141 (69)	—	[-0.04, 2.05]	—
$HH$ multilepton [73]	21.3 (19.4)	[-6.9, 11.1]	—	✓
$\tau\tau\gamma\gamma$ [74]	33 (26)	[-13, 18]	—	—
$b\bar{b}ZZ$ [75]	32.4 (39.6)	[-8.8, 13.4]	—	—
$WW\gamma\gamma$	97 (53)	[-25.8, 14.4]	—	✓

Where required, the event selection of each analysis was modified for the combination to prevent double counting of events. The strategy for this overlap removal is based upon work done for the combinations in Ref. [4].

## 4.1 $\text{HH} \rightarrow \text{b}\bar{\text{b}}\text{b}\bar{\text{b}}$

The  $\text{b}\bar{\text{b}}\text{b}\bar{\text{b}}$  decay channel has the largest HH branching fraction (33.6%) among the HH decays to SM particles. Three analyses target the  $\text{b}\bar{\text{b}}\text{b}\bar{\text{b}}$  decay channel. The first two search for HH pair produced via ggF or VBF. In one case the topology of the b jets is resolved while in the other the b jets are produced with high Lorentz boost resulting in a merged signature, where pairs of jets are reconstructed as a single large radius jets. The third analysis is dedicated to the search for VHH production. In this case, the final state is characterised by the decay mode of the vector boson. Figure 5 illustrates the topology of each analysis.

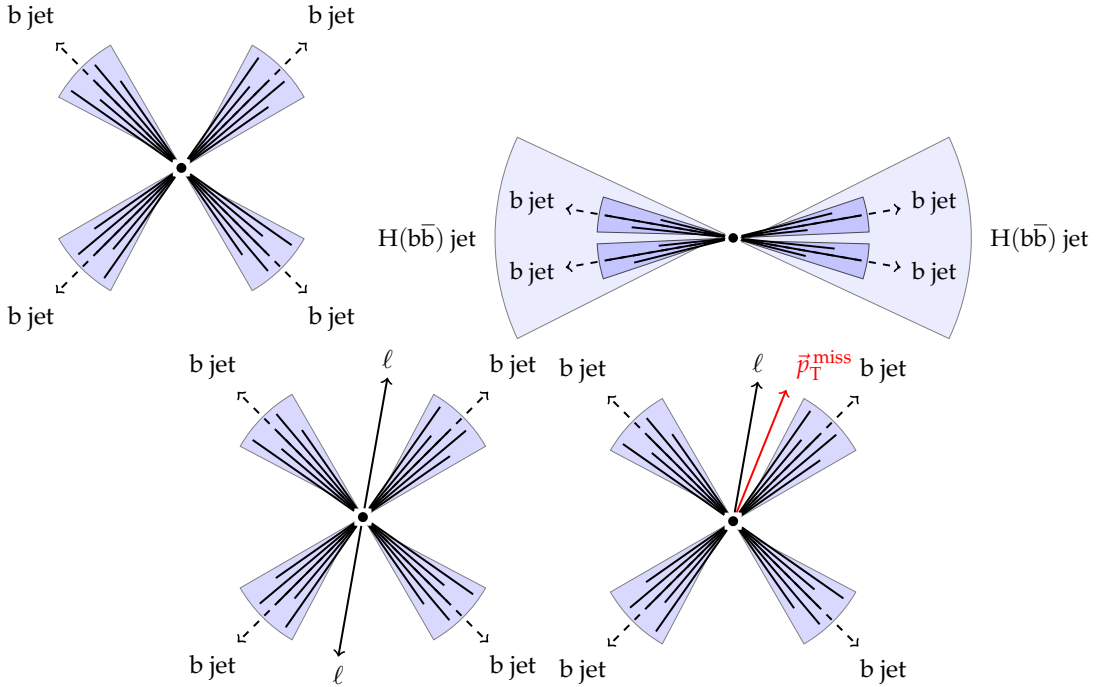


Figure 5: Illustrations of the resolved (upper left) and boosted (upper right) topologies of the  $\text{b}\bar{\text{b}}\text{b}\bar{\text{b}}$  decay channel. The topology of VHH production when all Higgs bosons decay to b jets and the vector boson is either a Z boson that decays into two leptons (lower left) or a W boson decaying into a lepton and a neutrino, giving missing transverse momentum (lower right).

### 4.1.1 $\text{HH} \rightarrow \text{b}\bar{\text{b}}\text{b}\bar{\text{b}}$ resolved

The resolved search [67] focuses on the kinematic phase space where each Higgs boson is reconstructed from two small-radius b-tagged jets. It explores both the ggF and VBF HH production modes. The VBF topology is characterised by two additional jets with high invariant mass and large pseudorapidity separation  $\Delta\eta$ . The online trigger selection requires the presence of at least four jets, satisfying thresholds on jet  $p_T$  and  $H_T$ , defined as the scalar  $p_T$  sum of all the jets. These thresholds vary depending on the data-taking year between 30 and 90 GeV for  $p_T$  and 300 to 330 GeV for  $H_T$ . Consequently, data collected in 2016 are analysed separately from those collected in 2017 and 2018.

Events selected offline contain at least four jets. Jets originating from a b quark decay are identified using the DEEPJET [76] algorithm. The four jets with the highest DEEPJET score are chosen as b jet candidates. The  $p_T$  of the four b jets is corrected using a multivariate regression method based on a deep neural network (DNN) [77]. At least three b jets must satisfy the DEEPJET medium working point (WP) DEEPJET [76], which corresponds to a b jet identification efficiency of about 75% and a misidentification rate for light-flavour quark and gluon jets of

about 1%. The VBF jet candidates are the two highest  $p_T$  non-b jets located in opposite  $\eta$  hemispheres. Events that contain any isolated electrons or muons are rejected.

There are three possible ways to pair the four b jets in order to reconstruct two Higgs boson candidates. For each pairing, a distance parameter  $d = |m_{H_1} - km_{H_2}| / \sqrt{1 + k^2}$  is calculated, where  $m_{H_1}$  is the mass of the Higgs boson candidate with the highest  $p_T$ ,  $m_{H_2}$  is the mass of the other Higgs boson, and  $k = 1.04$ . The constant  $k$  is the ratio of the expected peak positions of the reconstructed Higgs boson masses for events that are correctly paired. Its value differs from 1 because of the residual dependence of the multivariate energy regression on the jet  $p_T$  that more strongly impacts the softer H candidate. If the difference between the two smallest distance parameters is larger than 30 GeV, then the pairing with the smallest distance parameter is selected. Otherwise, between the two pairings with the smallest distance, the one maximising the  $p_T$  of the two H candidates in the four-jet centre-of-mass frame is chosen. This procedure results in a correct jet pairing of about 82–96 (91–98)% of the selected events for the different couplings studied in ggF (VBF) simulated signal events.

Events that do not have a VBF jet pair are assigned to the ggF event category. A  $BDT_{ggF/VBF}$  discriminant is trained to separate ggF and VBF HH signals in events that contain the VBF jet pair. The  $BDT_{ggF/VBF}$  is trained using SM ggF signal and VBF signal with  $\kappa_{2V} = 2$ . A threshold on the  $BDT_{ggF/VBF}$  score is used to classify those events into the ggF or VBF event categories. The ggF and VBF categories are each further divided into subcategories to optimise the search sensitivity to anomalous coupling hypotheses. In the ggF category, events are separated into low-mass and high-mass categories using a 450 GeV threshold on the Higgs boson pair invariant mass  $m_{HH}$ . In the VBF category, events are divided into “SM-like” and anomalous- $\kappa_{2V}$  categories using a threshold on  $BDT_{ggF/VBF}$ .

The dominant background source is from SM events composed uniquely of jets produced through the strong interaction, referred to as QCD multijet events. The analysis signal region (SR) contains at least four b jet candidates satisfying the DEEPJET medium WP. The background of this ‘4b’ region is estimated using events from an orthogonal region in which the fourth-highest b-tagged jet fails the medium WP (or ‘3b’ region). The transfer function to model the 4b background from the 3b data, comprises a BDT reweighting and a transfer factor (TF) for reshaping and normalisation corrections.

To remove overlapping events between this analysis and the analysis of  $b\bar{b}b\bar{b}$  events in the boosted topology described in Section 4.1.2, an event veto is applied for the combination described in this paper. Events containing two massive large-radius jets with  $p_T > 300$  GeV and at least two subjets are removed from this analysis. The  $p_T$  threshold was optimised based on the expected HH signal strength.

#### 4.1.2 $HH \rightarrow b\bar{b}b\bar{b}$ boosted

The search in the  $b\bar{b}b\bar{b}$  boosted final state [68] focuses on the phase space region where both Higgs bosons are highly Lorentz boosted so that each Higgs boson is reconstructed as a large-radius jet. The search is sensitive to modified coupling scenarios that enhance the production of highly boosted Higgs boson pairs, including through the VBF production.

A combination of several trigger algorithms is used with requirements on the total  $H_T$  or a large-radius jet  $p_T$  to be above a given threshold. This search uses the soft-drop (SD) algorithm [78] to reconstruct the masses of the two Higgs boson candidates.

The graph neural network (NN) algorithm [79–82] known as PARTICLENET [80, 83] is used to discriminate between  $H \rightarrow b\bar{b}$  and QCD-induced jets. To improve the jet mass estimation,

a regression algorithm based on the PARTICLENET graph NN architecture is introduced to predict the jet mass ( $m_{\text{reg}}$ ) [84].

Events are required to have at least two large-radius jets and then grouped into mutually exclusive ggF and VBF categories. The VBF categories are designed to select VBF signal events with the characteristic signature of two additional small-radius jets in the opposite forward regions of the detector. Three VBF event categories (high, medium, and low purity) are defined based on the PARTICLENET discriminant ( $D_{\text{b}\bar{\text{b}}}$ ) scores of the two Higgs boson candidate jets.

Events not sorted into the VBF categories are considered for the ggF categories. A BDT is trained to discriminate between the HH signal and QCD multijet or  $t\bar{t}$  background processes based on the kinematic and substructure properties of the two Higgs boson candidate jets and the  $m_{\text{SD}}$ ,  $\eta$ , and  $D_{\text{b}\bar{\text{b}}}$  of the  $D_{\text{b}\bar{\text{b}}}$ -leading jet. Three SRs targeting the ggF production are constructed depending on the BDT output score and the  $D_{\text{b}\bar{\text{b}}}$ -subleading large-radius jet  $D_{\text{b}\bar{\text{b}}}$  score. The  $m_{\text{reg}}$  distribution of the  $D_{\text{b}\bar{\text{b}}}$ -subleading jet is used to extract the signal.

The dominant SM backgrounds are  $t\bar{t}$  and QCD multijet production. Control regions (CRs) enriched in QCD multijet events are selected by changing the requirement on the  $D_{\text{b}\bar{\text{b}}}$  discriminant. The QCD multijet background in the SRs is estimated using the data in the CRs and fitted TFs [85–87]. An auxiliary sample enriched in  $t\bar{t}$  events containing one leptonically decaying W boson is used to extract corrections for the  $t\bar{t}$  background estimate [88].

#### 4.1.3 VHH, $\text{HH} \rightarrow \text{b}\bar{\text{b}}\text{b}\bar{\text{b}}$

This analysis [69] focuses on the final state with both Higgs bosons decaying into a b quark-antiquark pair. All decay modes of vector bosons Z and W are considered. Experimentally, the events are divided into four categories based on the presence of a light lepton  $\ell$  ( $=\mu, e$ ) and jets: 2 leptons, 1 lepton,  $p_{\text{T}}^{\text{miss}}$  and fully hadronic channel, corresponding to the  $Z \rightarrow \ell\ell, W \rightarrow \ell\nu, Z \rightarrow \nu\nu$ , and  $Z/W \rightarrow \text{qq}$  processes, respectively. Because of the large overlap with the ggF and VBF  $\text{b}\bar{\text{b}}\text{b}\bar{\text{b}}$  channels, the VHH fully hadronic channel is removed from this combination. Two event topologies are explored in this analysis: one involving four small-radius b jets, and the other with two large-radius jets, each from an  $H \rightarrow \text{b}\bar{\text{b}}$  decay.

In the leptonic channels, events are selected using triggers requiring isolated leptons or large  $p_{\text{T}}^{\text{miss}}$ . In the resolved topology, at least three AK4 jets are required to pass the medium WP of the DEEPJET b tagging algorithm. If there are more than four b-tagged jets, the ones with the highest b tagging scores are selected. An energy-regression method [77] is applied to the b jets in order to improve the resolution of the dijet mass. The two Higgs boson candidates are reconstructed by pairing the four jets with the same method used in the resolved  $\text{b}\bar{\text{b}}\text{b}\bar{\text{b}}$  analysis. In the boosted topology, two AK8 jets are required to have PARTICLENET  $D_{\text{b}\bar{\text{b}}}$  scores greater than 0.8. Given the higher sensitivity in the boosted topology, it is given priority if an event can be assigned to both topologies.

A categorisation BDT is trained to divide events into regions sensitive to  $\kappa_{\lambda}$  and  $\kappa_{2V}$ . In each region, another BDT is trained using all the signal processes in order to optimise the signal versus background discrimination. The final signal strength is extracted by fitting the BDT score distribution in the signal and CRs.

## 4.2 $\text{HH} \rightarrow \text{b}\bar{\text{b}}\tau\tau$

In the  $\text{b}\bar{\text{b}}\tau\tau$  channel [70], the events are characterised by the decay mode of the two  $\tau$  leptons. With branching fraction 7.3%, this channel combines relatively large branching fraction and

easy to reconstruct final states. This analysis studies final states where at least one of the  $\tau$  leptons decays hadronically, i.e.  $\tau_\mu \tau_h$ ,  $\tau_e \tau_h$ , and  $\tau_h \tau_h$ . The light leptons and  $\tau_h$  candidates must have opposite electric charges. The  $\tau_h$  candidates are reconstructed using the DEEPTAU algorithm [89], an NN method discriminating  $\tau_h$  candidates from jets, electrons, and muons. Events are required to have at least two b jets identified using the DEEPJET algorithm.

The events are selected by triggers requiring a single light lepton, or a lepton accompanied by a  $\tau_h$  candidate or two  $\tau_h$  candidates. A trigger dedicated to the VBF topology was introduced in late 2017, requiring two  $\tau_h$  candidates and two additional jets.

For each event, all b jet candidates are assigned a score by an NN trained to recognise the  $H \rightarrow b\bar{b}$  topology. The two jets with the highest score are selected as the b jets from the Higgs boson decays. The events that have two additional small-radius jets are identified as originating from the VBF process.

After the event selection, the events are divided into categories. The first set of categories splits the events according to the number and topology of the jets. Events with two small-radius jets separated by  $\Delta R = \sqrt{\Delta\eta^2 + \Delta\phi^2} < 0.4$  are classified in the boosted category. All remaining events are classified in the resolved categories. The resolved category is further split according to whether one or both jets pass the medium WP of the DEEPJET b tagging algorithm. Finally, an additional VBF category selects events with at least two VBF jet candidates. The contamination of this category from ggF events with an extra jet is significant; therefore, a multiclassifier DNN is trained. The DNN splits the events in the VBF category into signal-like VBF events, ggF contamination,  $t\bar{t}H$ ,  $t\bar{t}$ , and Drell–Yan (DY) background events.

All selected events are subject to a selection on the two-dimensional plane of the invariant mass of the dijet ( $m_{b\bar{b}}$ ) and ditau ( $m_{\tau\tau}$ ) systems, where the  $m_{\tau\tau}$  is reconstructed using the SVFIT algorithm [90]. This selection is optimised separately for the resolved and the boosted categories, and is not applied to the VBF categories.

The eight event categories defined earlier are used for the signal extraction using a DNN developed to identify  $HH \rightarrow b\bar{b}\tau\tau$  events. The DNN is trained to classify the events from each event category as signal or background-like by assigning a single prediction per event. The maximum likelihood fit for signal extraction is performed using the DNN distribution simultaneously for all categories and all channels.

The main background processes for this search,  $t\bar{t}$ , DY, and QCD multijet, are estimated using control samples in data. The shapes of the  $t\bar{t}$  and DY processes are taken from the simulation and then scaled using background-enriched regions. The scaling is extracted with a simultaneous fit over all the CRs and applied to the simulated events in the SR.

The QCD multijet process is entirely determined from data in jet-enriched regions where two selection requirements for the  $\tau$  pair are inverted. The event yield and shape are obtained in a region where the  $\tau_h$  is not required to be isolated from other tracks. In  $\tau_h \tau_h$  events, only the  $\tau_h$  with the lowest  $p_T$  is allowed to not be isolated. Then, the yield is scaled by the ratio of event yield in a region where the opposite charge requirement is inverted and a region where both the charge and the isolation are inverted. The contributions from other backgrounds are subtracted. The QCD multijet background is estimated after the  $t\bar{t}$  background has been scaled.

### 4.3 $HH \rightarrow b\bar{b}\gamma\gamma$

The  $b\bar{b}\gamma\gamma$  final state [71] despite the small branching fraction (0.26%), profits from the good mass resolution of the diphoton system. The parameters of interest of the model are extracted

from a two-dimensional fit to the invariant mass distributions of the photon pair ( $m_{\gamma\gamma}$ ) and b jet pair ( $m_{\text{b}\bar{\text{b}}}$ ). The HH signal can be identified as a peak in the ( $m_{\gamma\gamma}$ ,  $m_{\text{b}\bar{\text{b}}}$ ) distribution at the value of the Higgs boson mass. Jets originating from the b quark decay are identified using the DEEPJET algorithm. The background is dominated by the  $\gamma\gamma$ +jets and  $\gamma$ +jets continuum, and is modelled from the data sidebands of the  $m_{\gamma\gamma}$  and  $m_{\text{b}\bar{\text{b}}}$  distributions. Other important background sources are the single Higgs boson production processes, in which the Higgs boson decays into a photon pair ( $\text{H} \rightarrow \gamma\gamma$ ). The largest  $\text{H} \rightarrow \gamma\gamma$  background is the  $\text{t}\bar{\text{t}}\text{H}(\gamma\gamma)$  process because of the sizable cross section and the b jets in the final state from the  $\text{t}\bar{\text{t}}$  decay. The  $\text{H} \rightarrow \gamma\gamma$  processes are modelled using MC simulations.

Exclusive categories targeting specific HH production modes are defined to maximise the sensitivity to the signal. The SR targeting the VBF mechanism has requirements on the two additional jets. The VBF event candidates are classified into two exclusive categories depending on the value of the reduced four-body mass  $M_X$ , defined as  $M_X = m_{\text{bb}\gamma\gamma} - m_{\gamma\gamma} - m_{\text{b}\bar{\text{b}}} + 250 \text{ GeV}$ , where  $m_{\text{bb}\gamma\gamma}$  is the four-body invariant mass of the pairs of photons and b jets. A BDT classifier is defined to isolate the VBF signal from the ggF signal and the continuum background. For the ggF-enriched categories, a BDT classifier is used to reject the continuum background. The values of the BDT score and  $M_X$  are used to classify the events in twelve ggF-enriched categories. The number and boundaries of the categories are optimised to maximise the expected significance of the SM HH signal.

Furthermore, a DNN is trained to separate the HH signal from the  $\text{t}\bar{\text{t}}\text{H}(\gamma\gamma)$  process. The selection on the DNN output score reduces the  $\text{t}\bar{\text{t}}\text{H}$  background by between 80 and 85% and provides an efficiency between 90 and 95% for the HH signal, depending on the analysis category.

## 4.4 $\text{HH} \rightarrow \text{b}\bar{\text{b}}\text{WW}$

The  $\text{b}\bar{\text{b}}\text{WW}$  decay mode has the second largest branching fraction (24.8%) among all HH decay modes. Two different analyses target the  $\text{b}\bar{\text{b}}\text{WW}$  decay channel. The analyses address distinct final states and experimental signatures. The first is a search for the  $\text{WW} \rightarrow \ell\nu\text{qq}/2\ell 2\nu$  final state. The Higgs boson candidates decaying to b quarks can lead to either resolved or boosted topologies, i.e. forming two narrow-radius b jets or one large-radius b jet. The second analysis is a search for  $\text{WW} \rightarrow 4\text{q}$  studied only in boosted topologies. All four jets from the W decays are expected to be overlapping and form one large-radius jet. The accompanying pair of b jets is also merged into one large-radius jet. Figure 6 illustrates the final states of the two analyses.

### 4.4.1 $\text{HH} \rightarrow \text{b}\bar{\text{b}}\text{WW}, \text{WW} \rightarrow \ell\nu\text{qq}/2\ell 2\nu$

While  $\text{b}\bar{\text{b}}\text{WW}$  is the dominant channel in this final state,  $\text{b}\bar{\text{b}}\text{ZZ}$  and  $\text{b}\bar{\text{b}}\tau\tau$  decays of the HH system that result in a pair of b quarks and one or two light leptons are also included in the signal. The analysis [72] considers two final states: single-lepton ( $1\ell$ )  $\text{b}\bar{\text{b}}\ell\nu\text{qq}$  and dilepton ( $2\ell$ )  $\text{b}\bar{\text{b}}2\ell 2\nu$ . The most significant background contribution is the  $\text{t}\bar{\text{t}}$  process, while other backgrounds include events with misidentified leptons, and the DY process and W+jets process for the  $2\ell$  and  $1\ell$  channels, respectively.

The data are collected using single- and double-lepton triggers. The event selection criteria require the presence of one isolated lepton in the  $1\ell$  channel or two isolated leptons of opposite charge in the  $2\ell$  channel, originating from the W leptonic decays. The  $\text{H} \rightarrow \text{b}\bar{\text{b}}$  system is characterised by two jets. In the resolved category these are small-radius jets, and for the signal they are both originating from b quark. In the event selection at least one must be classified as a b jet by the DEEPJET algorithm. If the  $\text{H} \rightarrow \text{b}\bar{\text{b}}$  system is produced with high momentum, the two

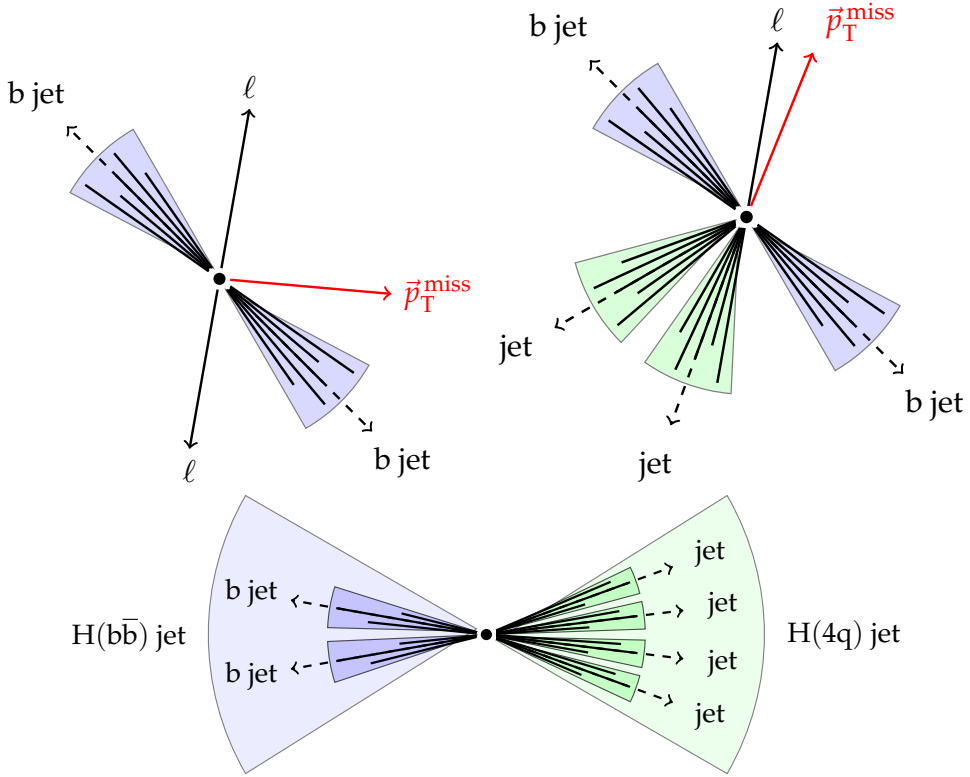


Figure 6: Illustrations of the resolved topology of the  $b\bar{b}WW$  decay channel in the final state with two leptons (upper left) and one lepton (upper right). The boosted topology of the fully hadronic  $b\bar{b}WW$  decay channel (lower).

$b$  jets are Lorentz boosted and can be reconstructed as one large-radius jet with substructure. In the  $1\ell$  case, the events must have at least one more small-radius jet present, corresponding to the hadronic  $W$  decay.

To avoid event overlap with the  $b\bar{b}\tau\tau$  analysis, this analysis vetoes events containing at least one  $\tau_h$  candidate, as defined in Ref. [70]. The events are classified using multiclass DNNs, trained separately for the  $1\ell$  and  $2\ell$  cases. The DNNs are trained using high-level features, such as invariant masses, hadronic activity, and the output of a Lorentz-boost network that performs automated feature engineering using the four-momenta of selected leptons and jets. The DNN training data set includes signal samples with SM and anomalous  $\kappa_\lambda$  values to ensure good performance on the full model spectrum.

The multiclass DNNs have different output nodes corresponding to several background processes and two signal processes: ggF and VBF HH production. The DNNs provide a score for each node that can be interpreted as the probability of each event to belong to that class. The events are categorised according to the node with the highest score. The resulting background categories are: DY or  $W+jets$  for the  $2\ell$  or  $1\ell$  channel, respectively, and  $t\bar{t}$  for both channels. The two signal categories are further divided into subcategories according to the  $b$  jet multiplicity and topology into resolved-1 $b$ , resolved-2 $b$ , and boosted.

The background contribution from misidentified leptons is estimated using the misidentification factor method [91]. In the  $2\ell$  channel, the DY background is estimated using data. Events with zero  $b$ -tagged jets are weighted by TFs extracted from events with the dilepton invariant mass inside the  $Z$  boson mass window. All other backgrounds are estimated using simulated events. The signal extraction is performed using a simultaneous maximum likelihood fit to the

distributions of the DNN outputs in the signal and background event categories.

#### 4.4.2 $\text{HH} \rightarrow b\bar{b}\text{WW}, \text{WW} \rightarrow 4q$

The all-hadronic  $b\bar{b}\text{WW}$  search targets highly Lorentz-boosted pairs of Higgs bosons produced via ggF and VBF. The  $b\bar{b}$  quark pair is reconstructed as a large-radius jet and all four quarks from the W decays form another large-radius jet. This analysis focuses mainly on the  $b\bar{b}\text{WW}$  decays, however, HH decays into  $b\bar{b}\text{ZZ}$  in the fully hadronic final state are also included in the signal. The MC samples used for the modeling of the backgrounds are the same as in Ref. [72].

The primary physics objects considered are two AK8 jets representing the two Higgs bosons. Additional AK4 jets are also used in the online selection and to identify VBF HH production, while events containing any isolated electrons and muons are vetoed. The online selection is based on the combination of high hadronic activity and the presence of AK8 jets.

Offline, the  $H \rightarrow b\bar{b}$  and  $H \rightarrow \text{WW}$  decays are targeted through a selection of two AK8 jets with  $p_T > 300 \text{ GeV}$  and  $|\eta| < 2.4$ . The PARTICLENET algorithm [80] is used to isolate the signal  $H \rightarrow b\bar{b}$  jets against background QCD using a discriminant,  $D_{b\bar{b}}$ , derived from its outputs, while to identify the  $H \rightarrow \text{WW} \rightarrow 4q$  jet, a new attention-based NN, based on the “particle transformer” (PART) architecture [92, 93] is used. Both networks have been decorrelated from the mass of their respective AK8 jets by enforcing a uniform distribution in jet mass and  $p_T$  in the training samples [83], to aid with their calibration and background estimation. Additionally, as the jet mass resolution is crucial to the sensitivity of the search, the mass reconstruction for all AK8 jets is optimised using a PARTICLENET-based regression algorithm trained to learn the “true”, or event-generator-level, jet mass [84], the output of which we refer to as  $m_{\text{reg}}$ . The jet with the higher (lower)  $D_{b\bar{b}}$  score is considered the  $b\bar{b}$ - (WW-) candidate jet.

The VBF process produces two jets in opposite forward regions of the detector, with a large invariant mass and large  $\Delta\eta$ . To identify this mode, up to two AK4 jets are selected per event, required to have  $p_T > 25 \text{ GeV}$ ,  $|\eta| < 4.7$ , and a  $\Delta R$  of at least 1.2 and 0.8 from the  $b\bar{b}$ - and WW-candidate AK8 jets, respectively. Out of the selected events, the two highest  $p_T$  AK4 jets are considered the VBF jet candidates, and their invariant mass and  $\Delta\eta$  are used as input variables in a BDT to discriminate against QCD and other backgrounds. Other input variables include outputs from the PART tagger and the two selected AK8 jets’ kinematics. The variables are optimised to provide the highest BDT performance while remaining decorrelated from the  $b\bar{b}$ -candidate jet’s mass.

The BDT is optimised simultaneously for both the SM ggF and BSM VBF  $\kappa_{2V} = 0$  signals, and separate “ggF” and “VBF” SRs are defined using the BDT probabilities for the respective processes, referred to as  $\text{BDT}_{\text{ggF}}$  and  $\text{BDT}_{\text{VBF}}$ . Separate BDTs for the two processes were also tested, and the difference in performance was negligible.

The VBF region is defined by selections on the  $D_{b\bar{b}}$  score of the  $b\bar{b}$ -candidate jet ( $D_{b\bar{b}}^{b\bar{b}}$ ) and the  $\text{BDT}_{\text{VBF}}$  discriminant, corresponding to VBF signal (background) efficiencies of 40% ( $\approx 0.1\%$ ) and 20% ( $\approx 0.003\%$ ), respectively, chosen to optimise the expected exclusion limit on the VBF signal. The ggF region is defined by a veto on events passing the VBF selections along with selections on the  $D_{b\bar{b}}^{b\bar{b}}$  and  $\text{BDT}_{\text{ggF}}$  discriminants, corresponding to ggF signal (background) efficiencies of 60% ( $\approx 0.3\%$ ) and 7% ( $\approx 0.01\%$ ), respectively, similarly chosen to optimise the limit on the ggF signal. The uncertainty in the BDT signal efficiency is dominated by that of the PART tagger, which is calibrated based on a new technique [94] using the ratio of the primary Lund jet plane [95] densities of each quark subjet.

The search is performed in the two SRs using a one-dimensional likelihood model binned in the  $m_{\text{reg}}^{\text{bb}}$  of the  $\text{bb}$ -candidate jet ( $m_{\text{reg}}^{\text{bb}}$ ). The background in these regions is dominated by QCD multijet events, and is estimated through data in a “fail” region, defined using the same baseline selections on the two AK8 jets, but with the  $D_{\text{bb}}$  selection inverted. The QCD multijet yield in the SRs is estimated as the product of data in the fail region and polynomial TFs [85–87]. Other minor backgrounds include top quark and vector boson backgrounds, which are estimated using MC simulation and whose systematic and statistical uncertainties are incorporated in the final statistical analysis. The resulting  $m_{\text{reg}}^{\text{bb}}$  in the SRs, after a maximum likelihood fit to the data of the background model and SM HH signal, are shown in Fig. 7.

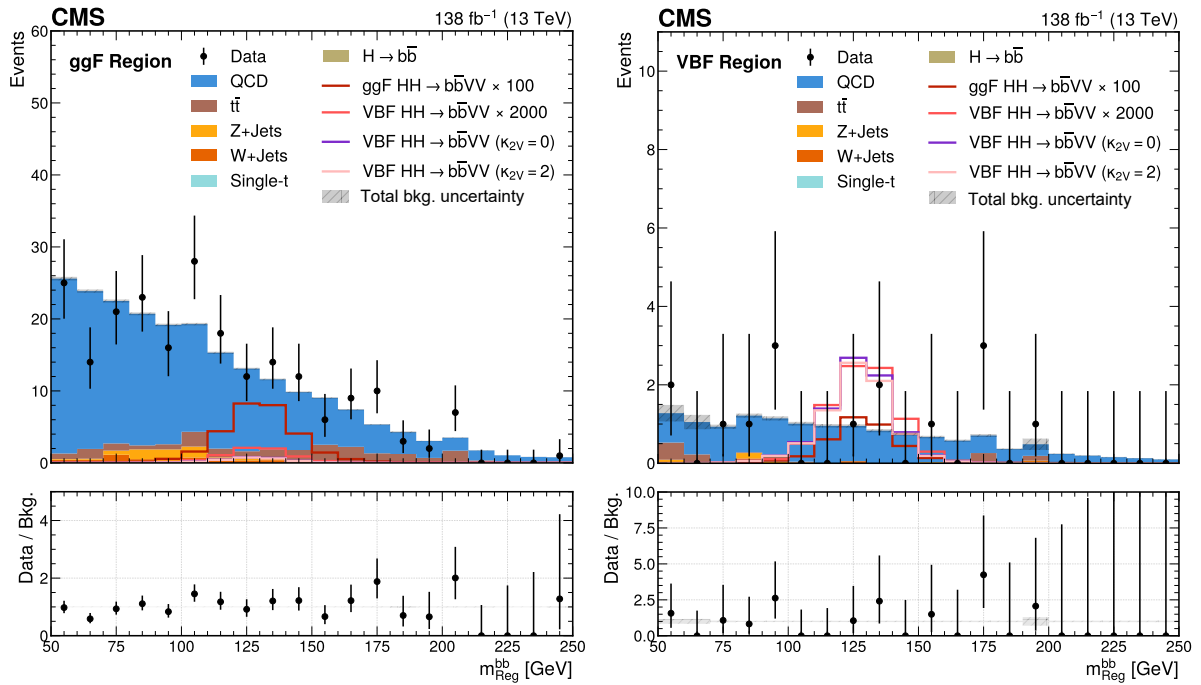


Figure 7: Distributions of the  $m_{\text{reg}}^{\text{bb}}$  observable in the ggF (left) and VBF (right) signal regions of the all-hadronic  $\text{bbWW}$  search, after a maximum likelihood fit of the background and SM HH signal to the data.

#### 4.5 $\text{HH} \rightarrow \text{multilepton}$

The HH multilepton analysis [73] focuses on HH decays into the 4W, 2W2 $\tau$ , and 4 $\tau$  channels. Events are selected using a set of single, double, and triple lepton triggers, as well as lepton and  $\tau_h$  triggers and double  $\tau_h$  triggers. The leptons and  $\tau_h$  candidates are reconstructed with a set of special identification (ID) criteria originally developed for the CMS  $\text{ttH}$  multilepton analysis [96]. These IDs are customised for the use of the misidentification factor method [91] used for the estimation of the background with misidentified lepton or  $\tau_h$  candidates from control samples in data. For electrons and muons, these two IDs also make use of a specialised multivariate analysis specifically trained to recognise genuine leptons that originate from vector boson and  $\tau$  lepton decays. All categories veto events containing at least one b jet identified with the medium WP of the DEEPJET algorithm and events containing at least two b jets identified with the loose WP, corresponding to a b jet selection efficiency of about 84% and a misidentification rate for light-flavour quark and gluon jets of about 11%. This reduces contributions from top quark related backgrounds, such as  $\text{tt}$  and makes this analysis orthogonal to the HH analyses requiring b jets.

The events are split into seven mutually exclusive event categories with final states containing multiple leptons  $\ell$  ( $\mu$ ,  $e$ ) or hadronically decaying  $\tau$  leptons ( $\tau_h$ ):  $2\ell$  with the same electric charge (SS),  $3\ell$ ,  $4\ell$ ,  $3\ell+1\tau_h$ ,  $2\ell+2\tau_h$ ,  $1\ell+3\tau_h$  and  $4\tau_h$ . All categories require the specified number of final-state light leptons and  $\tau_h$ . The  $2\ell$  SS and  $3\ell$  categories additionally require the presence of jets originating from hadronic  $W$  boson decays. The primary background in most categories is given by events containing misidentified  $\ell$  or  $\tau_h$  candidates. All categories also contain a sizable contribution of genuine multiboson backgrounds from  $ZZ$  and  $WZ$  decays. Therefore, two kinematic distributions in  $WZ$  and  $ZZ$  CRs are included in the fit. The categories are constructed by inverting the  $Z$  boson veto in the  $3\ell$  and  $4\ell$  categories, respectively. The inclusion of these two CRs helps to constrain the two main diboson backgrounds, as well as the corresponding systematic uncertainties.

The analysis makes use of a parameterised BDT tuning the sensitivity to the SM and to the EFT benchmark set JHEP04(2016)126 described in Section 3. The maximum likelihood fit for the signal extraction is performed simultaneously on the seven event categories. The results for each benchmark point are extracted from the corresponding BDT output. For the benchmarks not included in the BDT training, the most similar one based on the shape of the parton-level  $m_{\text{HH}}$  spectrum is used during inference.

## 4.6 $\text{HH} \rightarrow \tau\tau\gamma\gamma$

The search for  $\text{HH}$  production in the  $\tau\tau\gamma\gamma$  final state aims to cover both the hadronic and leptonic decay modes of the  $\tau$  lepton. Despite the small  $\text{HH} \rightarrow \tau\tau\gamma\gamma$  branching fraction in the SM ( $2.85 \times 10^{-4}$ ), the diphoton pair offers a clean experimental signature to trigger on with a good mass resolution, while the additional tau leptons in the event help to further isolate signal from background. The target of the search is the nonresonant  $\text{HH}$  production via  $ggF$ . The  $VBF$  production is not considered in this analysis.

Events are selected online using a diphoton trigger with asymmetric photon  $p_T$  thresholds of 30 and 18 GeV. All events are required to have at least one diphoton candidate, and in the case where more than one candidate exists, the candidate with the highest scalar  $p_T$  sum of the photons is chosen.

Events are required to have at least one  $\tau$  lepton candidate. Both hadronic and leptonic decay modes of the  $\tau$  lepton are considered. A  $\tau\tau$  candidate can be identified from any of the following pairs of reconstructed objects:  $\tau_h\tau_h$ ,  $\tau_h\mu$ ,  $\tau_h e$ ,  $\mu e$ ,  $\mu\mu$ ,  $ee$ ,  $\tau_h$ +isolated track. The DEEPTAU discriminant is used to select  $\tau_h$  candidates. Events consistent with a  $Z \rightarrow \ell\ell$  or  $Z \rightarrow \ell\ell\gamma$  decay are rejected.

A BDT classifier is used to further isolate events with signal-like characteristics from the background. Hadronic jets in the event are only used in the BDT to reject backgrounds like  $t\bar{t}$ . To reduce the probability of creating an artificially peaking structure, the  $m_{\gamma\gamma}$  is not included as an input feature to the BDT, and the  $p_T$  of the photon candidates are divided by  $m_{\gamma\gamma}$  to reduce correlations between the photon  $p_T$  and  $m_{\gamma\gamma}$ . Sequential boundaries are placed on the BDT output to define event categories of different signal purity, where the boundary positions are chosen to maximise the signal sensitivity.

The  $m_{\gamma\gamma}$  distribution is used in the maximum likelihood fit for each event category. The smoothly falling background (continuum) is modelled directly from the data. The signal and the single Higgs boson production, which is a resonant background, are modelled using simulation.

## 4.7 $\text{HH} \rightarrow \text{b}\bar{\text{b}}\text{ZZ}$

This analysis [75] focuses on ggF HH production where one Higgs bosons decays to a Z boson pair, which subsequently decays to  $4\ell$ , and the other to  $\text{b}\bar{\text{b}}$ , hadronising into jets. The  $4\ell$  in the final state form a clean signature, while the high branching fraction of the  $\text{b}\bar{\text{b}}$  decay channel partially compensates for the small branching fraction of the  $4\ell$  channel. The final state consists of at least two pairs of oppositely charged isolated electrons or muons and at least two jets. The  $4\ell$  signal region is defined by requiring the four-lepton invariant mass  $m(4\ell)$  to be within the Higgs boson mass window. Events outside this range are included in the  $4\ell$  CR.

The dominant  $\text{Z}+X$  background is characterised by non-prompt and misidentified leptons, mainly from decays of heavy-flavour hadrons, misidentified jets, and electrons from photon conversions. The  $\text{Z}+X$  background is estimated in a data-driven way, using a CR, and the probabilities of a light lepton to be misidentified. The dominant systematic uncertainty in the reducible background estimation arises mainly from the limited number of events in both the CR and the sample used for the computation of the misidentification rates. Uncertainties from the difference in the sample composition used to calculate the misidentification rate are also considered.

A BDT is used to further discriminate signal from backgrounds. The BDT is trained using simulated events in the  $4\ell$  SR; training is done using the ggF HH process as signal and all other processes as background. A maximum likelihood fit to the BDT output distribution is performed to set constraints on the parameters of interest.

## 4.8 $\text{HH} \rightarrow \text{WW}\gamma\gamma$

This analysis studies three WW decay modes: semileptonic ( $1\ell$ ), fully hadronic, and fully leptonic ( $2\ell$ ) decays. Events are selected using double-photon triggers with thresholds on the leading (subleading) photon  $p_{\text{T}}$  of  $p_{\text{T}}^{\gamma} > 30$  (18) GeV for the data collected during 2016 and  $p_{\text{T}}^{\gamma} > 30$  (22) GeV for 2017 and 2018. The MC samples used in this analysis are the same as the ones used in the  $\text{b}\bar{\text{b}}\gamma\gamma$  analysis [71]. The continuum background is modelled from data using the  $m_{\gamma\gamma}$  distribution. The single Higgs boson background is modeled using simulated samples.

A BDT classifier is trained for photon-jet separation, resulting in a photon identification score. The jets from the hadronisation of bottom quarks are identified using the DEEPJET algorithm. The number of light leptons is used to maintain orthogonality in all three analyses. We assign an event to the fully hadronic channel if it has no leptons, to the  $1\ell$  channel if it has exactly one lepton, and to the  $2\ell$  channel if it has two leptons. Each channel requires a diphoton candidate, which is defined as a pair of two photons.

The  $1\ell$  channel uses a multiclassifier DNN to differentiate between signal, single Higgs boson, and background events, as shown in Fig. 8, upper left.

The  $\text{b}\bar{\text{b}}\gamma\gamma$  signal contaminates the  $\text{WW}\gamma\gamma$  phase space in the fully hadronic channel. Therefore, two binary classifiers are used for the fully hadronic channel, one acting as a  $\text{b}\bar{\text{b}}\gamma\gamma$  discriminator and the other distinguishing between signal and background events, the latter shown in Fig. 8, upper right. A specific challenge in the fully hadronic channel is differentiating between the  $\text{ZZ}\gamma\gamma$  and the  $\text{WW}\gamma\gamma$  signal processes, due to the identical experimental signatures of the hadronic Z and W decays. There are residual  $\text{b}\bar{\text{b}}\gamma\gamma$  events that pass the  $\text{WW}\gamma\gamma$  event selection but are not favoured by the  $\text{b}\bar{\text{b}}\gamma\gamma$  analysis because of low  $\text{b}\bar{\text{b}}\gamma\gamma$  discriminator scores. Therefore, the combination of  $\text{WW}\gamma\gamma$ ,  $\text{ZZ}\gamma\gamma$ , and residual  $\text{b}\bar{\text{b}}\gamma\gamma$  processes is considered signal in this analysis. Finally, because of the limited size of the samples available for

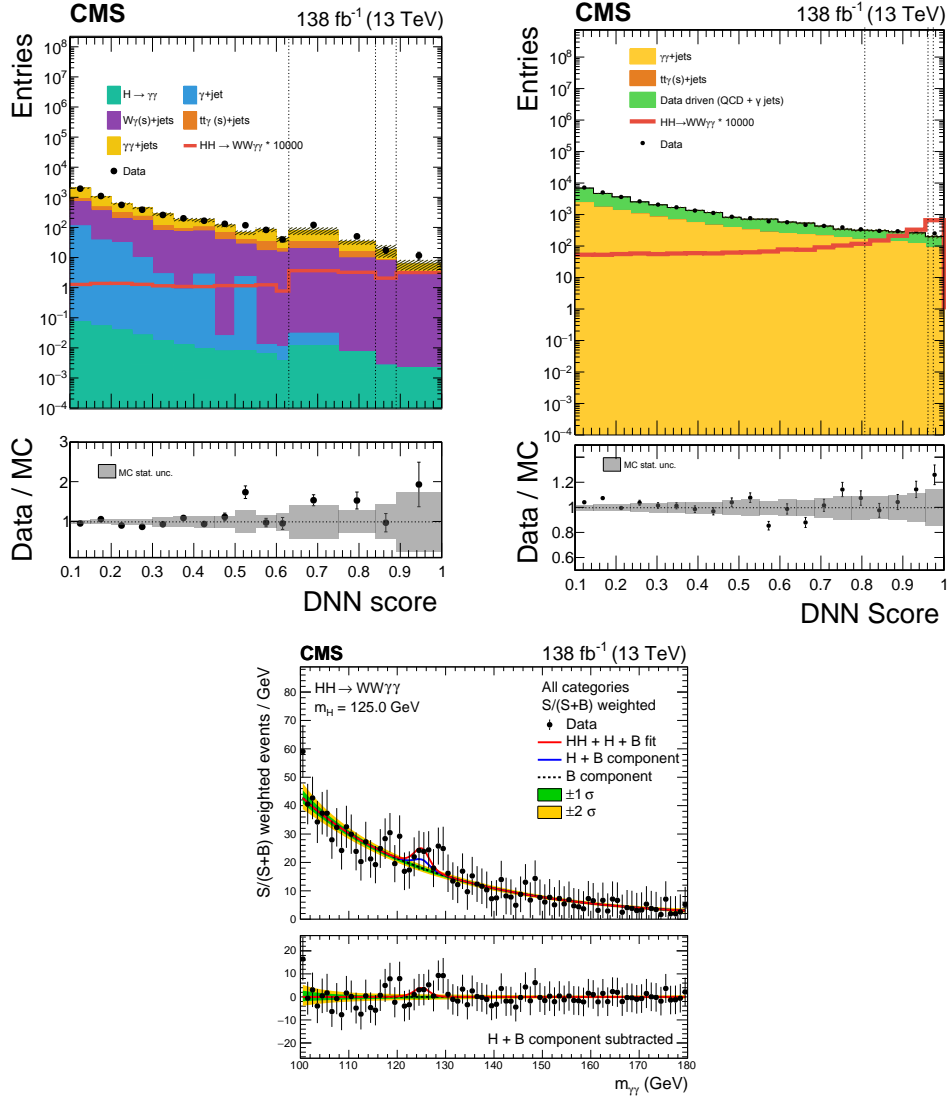


Figure 8: The distributions of DNN scores for the signal and main backgrounds in the  $1\ell$  (upper left) and fully hadronic (upper right) channels of the  $\text{WW}\gamma\gamma$  analysis. The signal-plus-background (red), single  $H$  plus continuum background (blue), and continuum background (dashed black) fits for all channels weighted by  $S/(S + B)$  (lower).

training and validating a multivariate event classifier, a selection based on traditional variables is adopted for the  $2\ell$  channel. The diphoton invariant mass distribution is used for the signal extraction across all channels. The signal-plus-background and background-only fits for all channels weighted by  $S/(S+B)$  are shown in Fig. 8, lower.

## 5 Systematic uncertainties

A number of systematic uncertainties are considered, affecting HH signal and background processes' yields (i.e. normalisation uncertainties) and/or shapes (i.e. shape uncertainties). The systematic uncertainties are introduced as nuisance parameters in the maximum likelihood fit used to extract the results. Common uncertainties among different analyses are fully correlated, while others specific to each analysis are treated as uncorrelated.

### 5.1 Theory uncertainties

Theoretical uncertainties on the renormalisation and factorisation scale, strong coupling constant  $\alpha_S$ , and PDFs affecting the cross section of all the simulated processes are included. Other uncertainties considered concern EW corrections for the  $t\bar{t}Z$ ,  $t\bar{t}W$ ,  $q\bar{q}ZZ$ , and  $ggZZ$  processes. Theoretical uncertainties in the Higgs boson branching fractions [97] are applied to both the HH signal and single-Higgs backgrounds. The assigned uncertainties are 1.2% for  $H \rightarrow b\bar{b}$ , 1.5% for  $H \rightarrow WW$  and  $H \rightarrow ZZ$ , 2.1% for  $H \rightarrow \gamma\gamma$ , and 1.6% for  $H \rightarrow \tau\tau$ . These uncertainties are treated as correlated across all channels. The uncertainty in the rate of Higgs boson production associated with heavy-flavour jets is assumed to be 50% [98].

Theoretical uncertainties on the nonresonant HH cross section via  $ggF$  is applied as a function of  $\kappa_\lambda$  and include a combination of uncertainties in the renormalisation and factorisation scales, as well as the uncertainty in the top quark mass. In the SM case when  $\kappa_\lambda = 1$ , this combined uncertainty corresponds to  $-23\% / +6\%$ . The PDF uncertainty is 3% [99]. Uncertainties for VBF production include  $+0.03\% / -0.04\%$  (scales) and 2.1% (PDF+ $\alpha_S$ ) [60, 100]. An additional scale uncertainty is applied to the  $b\bar{b}\tau\tau$ ,  $b\bar{b}WW$  and multilepton analyses related to PYTHIA and the colour-correlated recoil effect. This effect was found to be negligible in other analyses.

Some analyses suffer from a significant  $t\bar{t}$  background contribution ( $b\bar{b}WW$ , multilepton, and  $b\bar{b}\tau\tau$ ) and a shape uncertainty that corresponds to the NNLO correction on the top quark  $p_T$  is applied to the  $t\bar{t}$  simulated samples [101]. The  $b\bar{b}WW$  and multilepton analyses include additional uncertainties on the parton shower initial- and final-state radiation for background processes, on the top quark mass for the  $t\bar{t}$  background, as well as renormalisation and factorisation scale uncertainties for  $t\bar{t}$  and single top quark production.

### 5.2 Experimental uncertainties

The integrated luminosities for the 2016, 2017, and 2018 data-taking years have 1.2–2.5% uncertainty per year [102–104], while the overall uncertainty for the 2016–2018 period is 1.6%. The number of  $pp$  interactions is calculated from the instantaneous luminosity and an estimated inelastic  $pp$  collision cross section with 4.6% uncertainty [105]. An uncertainty in the shape of the distribution of the mean number of  $pp$  interactions per bunch crossing (pileup) is also applied to all simulated samples. The trigger selection efficiency is corrected in each analysis to account for the differences between the data and simulation, and a corresponding uncertainty is applied.

When identification criteria are applied to muons, electrons, and  $\tau_h$  candidates, the identification efficiencies in the simulated samples are corrected to match those in data. The uncertain-

ties related to these corrections affect the shapes of the kinematic distributions. For analyses that use the same selection criteria, these uncertainties are treated as correlated. For analyses that use photons, the shape uncertainties related to the photon identification efficiency are also considered.

Similarly, the uncertainties in the efficiency of the jet selection criteria in simulation, are considered as uncertainties on the shape of the kinematic distributions. Nuisance parameters that affect the shape of the jet flavour discriminant are also included. Different types of flavour contamination are treated with separate parameters. Uncertainties in the jet energy scale and resolution are used as shape uncertainties for all simulated samples. For analyses where  $p_T^{\text{miss}}$  is relevant, uncertainties related to the unclustered energy reconstruction efficiency are taken into account as correlated uncertainties in  $p_T^{\text{miss}}$  distribution shapes in simulated samples.

During data collection in 2016 and 2017, a gradual change in the timing of the ECAL first-level trigger inputs in the region with  $|\eta| > 2.0$  caused a specific trigger inefficiency. For events containing an electron (jet) with  $p_T \gtrsim 50$  (100) GeV in the region  $2.5 < |\eta| < 3.0$  the efficiency loss is approximately 10–20%, depending on  $p_T$ ,  $\eta$ , and time. Correction factors are computed from data and applied to the acceptance evaluated from simulation. In addition, a normalisation uncertainty is included in the global maximum likelihood fit, described in Section 6.

A correction factor is applied to simulated data for the 2018 era to account for two HCAL modules being switched off, and an associated shape uncertainty is introduced which is treated as correlated among most analyses. Analyses that perform data-driven background estimation methods include dedicated uncertainties, which are treated as uncorrelated.

Finally, uncertainties from the limited number of simulated events are taken into account using the Barlow–Beeston approach [106]. These uncertainties are not considered in the case of the HL-LHC projections, as it is assumed that we will have sufficient simulated data at the time.

## 6 Results

Upper limits on HH production cross sections and constraints on coupling modifiers that contribute to SM HH production are derived based on the asymptotic formulae for the profile likelihood ratio test statistic  $-2\Delta \ln(L)$  [107, 108] and the  $\text{CL}_s$  [109, 110] criterion. Generally, the test statistic is defined as

$$-2\Delta \ln(L) \equiv -2 \ln \left( \frac{L(\vec{\mu}, \hat{\vec{\nu}}(\vec{\mu}))}{L(\hat{\vec{\mu}}, \hat{\vec{\nu}})} \right), \quad (3)$$

where  $L$  is the combined likelihood function,  $\vec{\mu}$  are the parameters of interest, such as signal strengths or coupling modifiers,  $\hat{\vec{\mu}}$  are the best fit values of  $\vec{\mu}$ ,  $\hat{\vec{\nu}}(\vec{\mu})$  is the maximum likelihood estimator of the nuisance parameters for a given set of values of  $\vec{\mu}$ , and  $\hat{\vec{\nu}}$  is the global maximum likelihood estimator of the nuisance parameters for the best fit values of  $\vec{\mu}$ . The results of the different analyses described in this paper have been statistically combined in a global maximum likelihood fit. The HEFT parametrisation is used to provide constraints on a number of different BSM scenarios. In all cases, expected limits are derived under the background-only hypothesis. The results have been determined using the CMS statistical analysis tool COMBINE [111], which is based on the ROOFIT [112] and ROOSTATS [113] frameworks.

The upper limit at 95% CL on the inclusive HH production cross section is observed (expected) to be 3.5 (2.5) times the SM prediction, while the equivalent upper limit for the VBF alone is 79 (91) times the SM prediction. The limits on the HH cross section divided by the SM prediction,

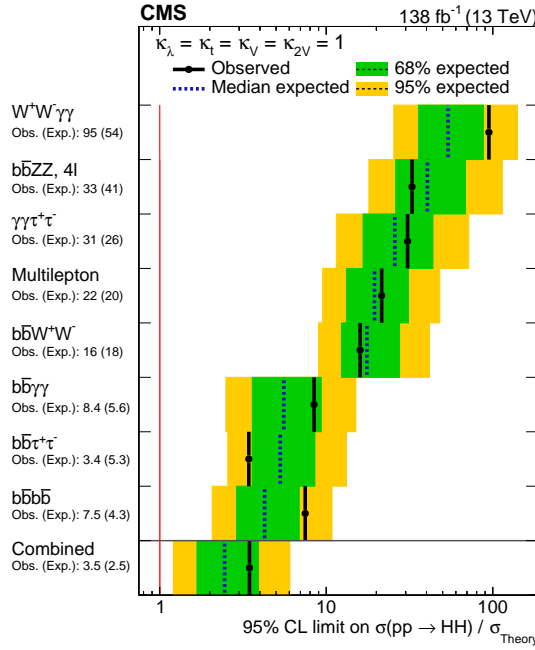


Figure 9: The upper limits at 95% CL on the inclusive signal strength  $\mu = \sigma_{\text{HH}} / \sigma_{\text{HH}}^{\text{SM}}$  for each channel and their combination. The inner (green) and outer (yellow) bands indicate the 68 and 95% CL intervals, respectively, under the background-only hypothesis. The individual contributions within the  $bbbb$  and  $bbWW$  channels have been combined in order to simplify the presentation of results.

i.e. the signal strength  $\mu$ , for each contributing channel and their combination are shown in Figs. 9 and 10 for the inclusive and VBF cases, respectively.

The  $-2\Delta \ln(L)$  scans as a function of  $\kappa_\lambda$  and  $\kappa_{2V}$  is shown in Fig. 11. Besides the ones varied as shown, all other couplings are set to the values expected by the SM. All eight channels are included in the combination. The best fit value of  $\kappa_\lambda$  is found to be 1.51 and  $\kappa_\lambda$  is constrained at 68% CL to be within  $-0.07$  and  $4.18$ , while the expected constraint is from  $-0.87$  to  $6.31$ . At 95% CL,  $\kappa_\lambda$  is constrained to be within  $-1.35$  to  $6.37$ , with an expected constraint of  $-2.24$  to  $7.89$ .

For  $\kappa_{2V}$ , the best fit value is at  $1.02$ , the 68% CL interval is from  $0.81$  to  $1.23$  ( $0.77$  to  $1.26$  expected), and the 95% CL interval is from  $0.64$  to  $1.40$  ( $0.62$  to  $1.41$  expected). The value of  $\kappa_{2V} = 0$  is excluded with a significance of 6.6 standard deviations. This level of significance marks a decisive step in establishing the presence of quartic Higgs-vector boson interactions in nature.

In Fig. 12, the upper limits at 95% CL on the HH cross section are shown as functions of  $\kappa_\lambda$  (left) and  $\kappa_{2V}$  (right), respectively. We exclude HH production when  $\kappa_\lambda$  is outside the range between  $-1.39$  and  $7.02$  at 95% CL. The expected range is between  $-1.02$  and  $7.19$ . Similarly, we exclude HH production when the  $\kappa_{2V}$  coupling modifier is outside the range between  $0.62$  and  $1.42$ , with the expected range between  $0.69$  and  $1.35$ .

The summary of the constraints on the coupling modifiers  $\kappa_\lambda$  and  $\kappa_{2V}$  is given in Table 4.

Figure 13 shows the 68 and 95% CL contours of  $-2\Delta \ln(L)$  in the  $(\kappa_\lambda, \kappa_{2V})$ ,  $(\kappa_V, \kappa_{2V})$ , and  $(\kappa_\lambda, \kappa_t)$  planes for the combination of all contributing channels. In the  $(\kappa_\lambda, \kappa_{2V})$  and  $(\kappa_V, \kappa_{2V})$  planes, the 5 standard deviation CL contours are also shown. All the other parameters, besides the ones scanned, are set to the values expected by the SM. The value of  $\kappa_{2V} = 0$  is excluded at a

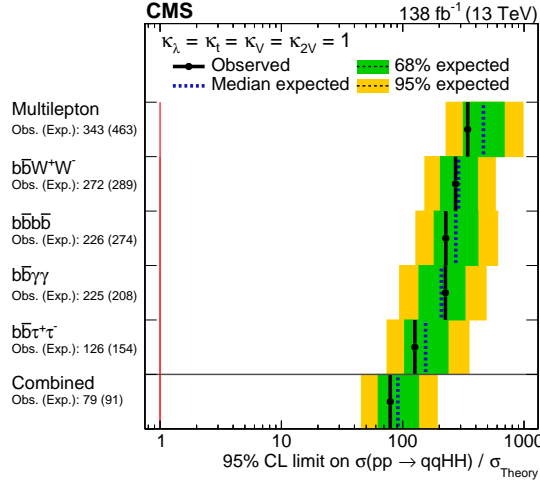


Figure 10: The upper limits at 95% CL on the VBF signal strength  $\mu_{\text{VBF HH}} = \sigma_{\text{VBF HH}} / \sigma_{\text{VBF HH}}^{\text{SM}}$  for each channel and their combination. The inner (green) and outer (yellow) bands indicate the 68 and 95% CL intervals, respectively, under the background-only hypothesis. The five contributing channels are indicated in the figure. The individual contributions within the  $b\bar{b}b\bar{b}$  and  $b\bar{b}WW$  channels have been combined in order to simplify the presentation of results.

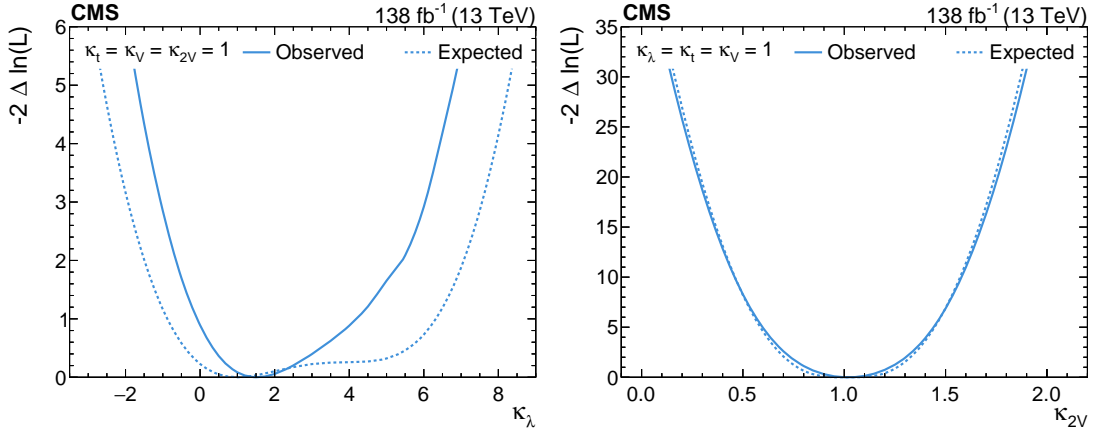


Figure 11: The  $-2\Delta \ln(L)$  scan as functions of coupling modifiers  $\kappa_\lambda$  (left) and  $\kappa_{2V}$  (right) for the combination of all channels when all the other parameters are fixed to their SM values.

CL of more than 5 standard deviations, for every value of  $\kappa_\lambda$ , adding to the robustness of this exclusion. No significant deviation from the SM is observed.

Table 4: Summary of results on constraints to the coupling modifiers  $\kappa_\lambda$  and  $\kappa_{2V}$ . The ranges are either extracted using either the  $-2\Delta \ln(L)$  scan at 68% and 95% CL, or upper limits on the signal strength  $\mu$  at 95% CL. The theoretical uncertainties in the ggF and VBF HH signal cross sections are considered in all results tabulated here.

Method	$\kappa_\lambda$ observed (expected)	$\kappa_{2V}$ observed (expected)
$-2\Delta \ln(L)$ scan, 68% CL	$[-0.07, 4.18]$ ( $[-0.87, 6.31]$ )	$[0.81, 1.23]$ ( $[0.77, 1.26]$ )
$-2\Delta \ln(L)$ scan, 95% CL	$[-1.35, 6.35]$ ( $[-2.24, 7.89]$ )	$[0.64, 1.40]$ ( $[0.62, 1.41]$ )
Limits on $\mu$ , 95% CL	$[-1.39, 7.02]$ ( $[-1.02, 7.19]$ )	$[0.62, 1.42]$ ( $[0.69, 1.35]$ )

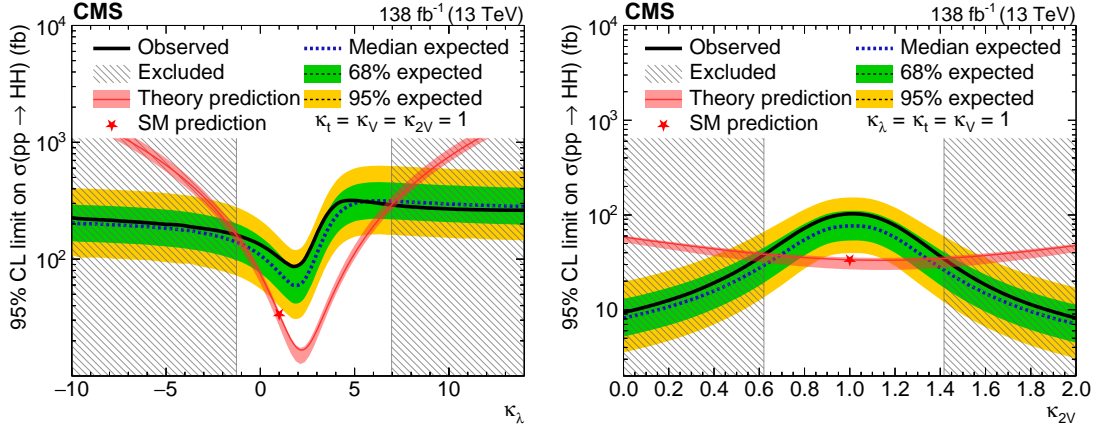


Figure 12: The 95% CL upper limits on the inclusive HH cross section as functions of  $\kappa_\lambda$  (left) and  $\kappa_{2V}$  (right). All other couplings are set to the values predicted by the SM. The theoretical uncertainties in the ggF and VBF HH signal cross sections are not considered because here we directly constrain the measured cross section. The inner (green) band and the outer (yellow) band indicate the 68 and 95% CL intervals, respectively, under the background-only hypothesis. The star shows the limit at the SM value for  $\kappa_\lambda$  and  $\kappa_{2V}$ .

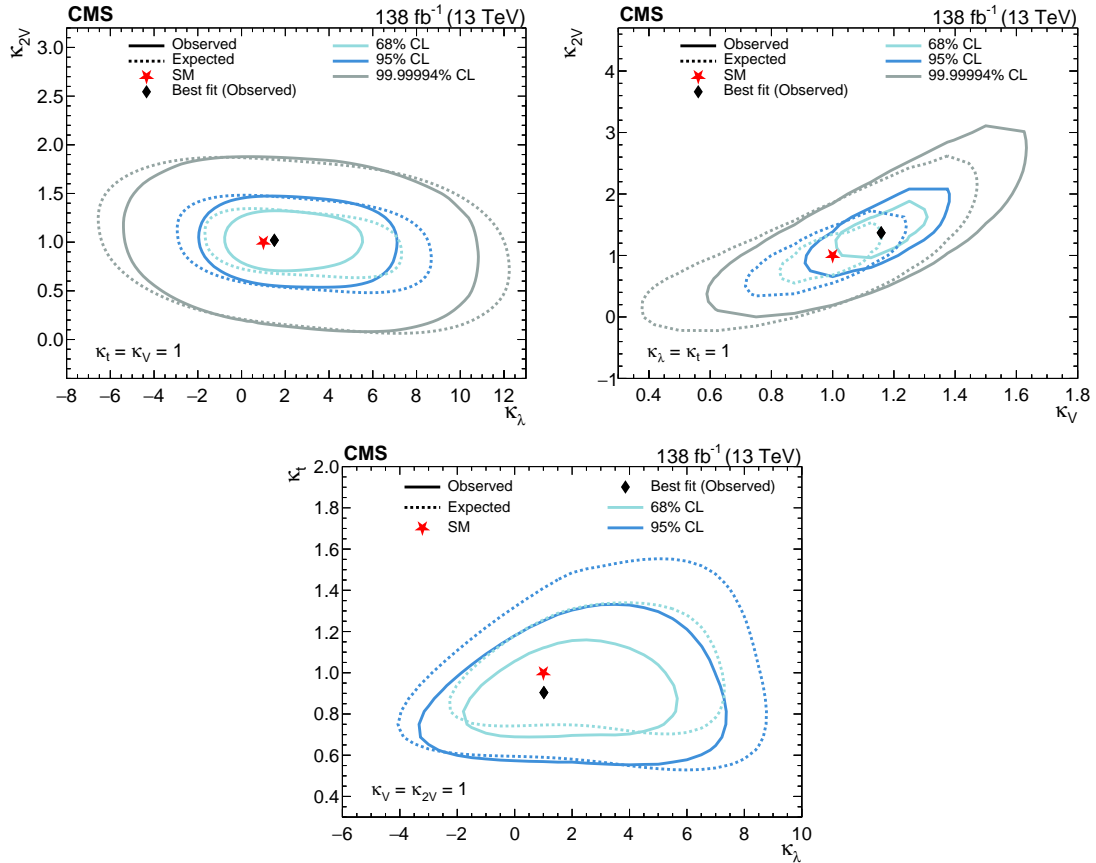


Figure 13: The 68 and 95% CL contours of  $-2\Delta \ln(L)$  in the  $(\kappa_\lambda, \kappa_{2V})$  (upper left),  $(\kappa_V, \kappa_{2V})$  (upper right), and  $(\kappa_\lambda, \kappa_t)$  (lower) planes for the combination of all channels when all the other parameters are fixed to their SM values. In the  $(\kappa_\lambda, \kappa_{2V})$  and  $(\kappa_V, \kappa_{2V})$  planes, the 5 standard deviation CL contours are also shown.

Beyond varying  $\kappa_\lambda$ ,  $\kappa_{2V}$ ,  $\kappa_V$ , and  $\kappa_t$ , we interpret the data in terms of couplings that are not predicted in the SM, namely  $c_2$ ,  $c_g$ , and  $c_{2g}$ . All BSM interpretations studied in this paper only alter the ggF production, while the VBF production is assumed to be as predicted by the SM. The channels contributing to the BSM interpretations are  $b\bar{b}\gamma\gamma$ ,  $b\bar{b}b\bar{b}$  boosted and resolved,  $b\bar{b}\tau\tau$ ,  $b\bar{b}WW$ , multilepton,  $WW\gamma\gamma$ , and  $\tau\tau\gamma\gamma$ .

First, we interpret the results in the context of two sets of benchmarks, JHEP04(2016)126 [50] and JHEP03(2020)091 [51], combinations of the coupling modifiers ( $\kappa_\lambda, \kappa_t, c_2, c_g, c_{2g}$ ) as described in Section 3. The  $\tau\tau\gamma\gamma$  channel only contributes to the results for the benchmarks JHEP04(2016)126, while the rest of the channels contribute to both sets. The upper limits on the HH cross section at 95% CL are shown in Fig. 14. No significant deviations from expectations are observed, but there is an overall excess in all benchmarks, between 68% and 95% CL, consistent with excesses observed in the most sensitive channels, namely  $b\bar{b}\gamma\gamma$  and  $b\bar{b}b\bar{b}$  especially in the boosted topology, visible in Fig. 9.

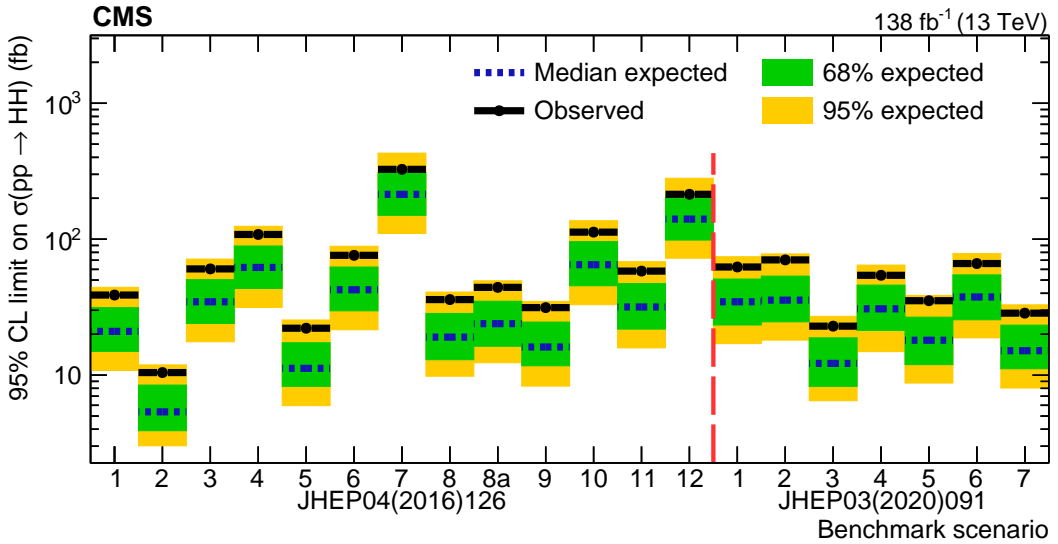


Figure 14: The upper limits at 95% CL on the HH production cross section for the two sets of HEFT benchmarks. The theoretical uncertainties in the ggF HH signal cross section are not considered because we directly constrain the measured cross section.

In the HEFT Lagrangian, the term containing  $\kappa_t$  is correlated with the coupling modifier  $c_2$ , which corresponds to the BSM coupling between two top quarks and two Higgs bosons. Figure 15 shows the  $-2\Delta \ln(L)$  scan for  $c_2$  on the left and the upper limits on the HH cross section as a function of  $c_2$  on the right. For  $c_2$ , the best fit to the data is found to be 0.40, the 68% CL interval is from 0.20 to 0.52 (−0.15 to 0.42 expected), and the 95% CL interval is from −0.29 to 0.63 (−0.27 to 0.56 expected). Taking into account the theoretical uncertainties in the ggF and VBF HH signal cross sections, we exclude HH production at 95% CL for  $c_2$  values outside the range from −0.28 to 0.59. The corresponding expected range is between −0.17 and 0.47. Figure 16 shows the two-dimensional contours of  $-2\Delta \ln(L)$  in the  $(c_2, \kappa_\lambda)$  and  $(c_2, \kappa_t)$  planes for the combination of all contributing channels.

The data are further interpreted in the context of several UV complete models, exploiting the HEFT parametrisation described in Section 3. Experimental constraints on the parameters that characterise each model are extracted, using a mapping between  $\kappa_\lambda, \kappa_t$ , and  $c_2$  and the specific model parameters.

The simplest extensions of the SM Higgs sector, are models with the addition of a single new

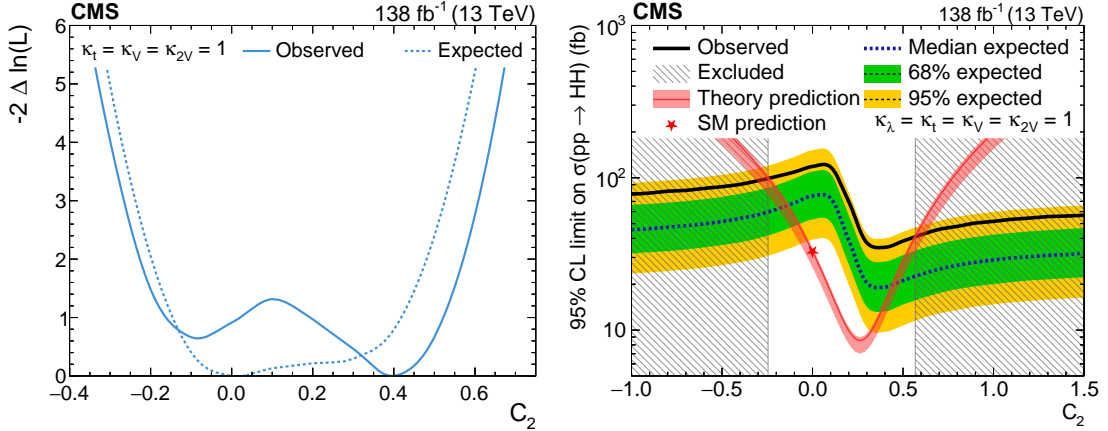


Figure 15: The upper limits at 95% CL on the HH cross section as a function of the  $c_2$  coupling modifier (left). The theoretical uncertainties in the ggF HH signal cross section are not considered because we directly constrain the measured cross section. The  $-2\Delta \ln(L)$  scan as a function of the  $c_2$  coupling modifier (right).

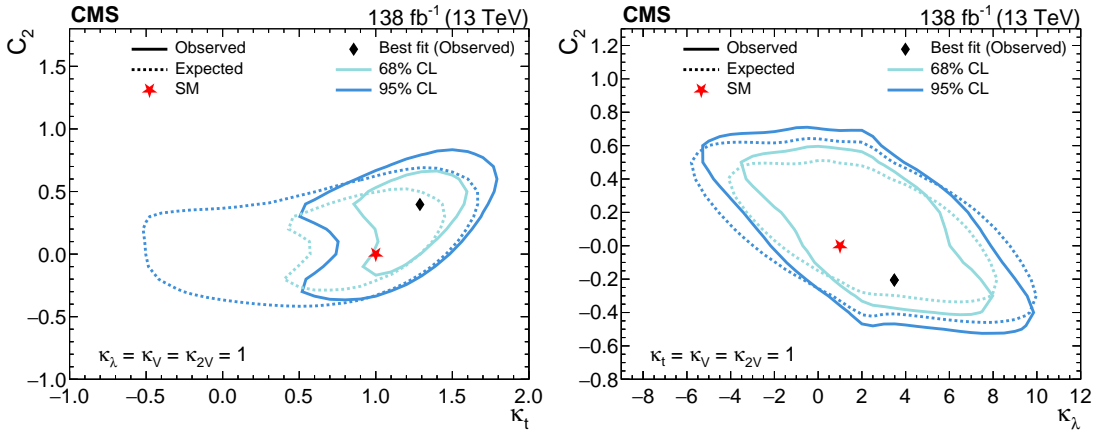


Figure 16: The 68 and 95% CL contours of  $-2\Delta \ln(L)$  in the  $(c_2, \kappa_t)$  (left) and  $(c_2, \kappa_\lambda)$  (right) planes for the combination of all channels when all the other parameters are fixed to their SM values.

scalar  $\phi$  with couplings to the Higgs doublet [6, 7]. For the following we consider both the case where the  $Z_2$  symmetry of the resulting potential  $V(\phi, H)$  is either explicitly or spontaneously broken. In the explicit case the modifications of Higgs boson interactions can be written in terms of  $\alpha$ , the mixing angle of the new scalar with the Higgs doublet,  $m_2$ , the coefficient of the triple singlet coupling and  $\lambda_\alpha$  the coefficient of the biquadratic term between scalar and Higgs potentials. In the spontaneously broken symmetry case, the modifications depend only on  $\alpha$ . Figure 17 shows the  $-2\Delta \ln(L)$  scan as a function of  $|\cos \alpha|$  and the 95% CL contour in the  $(|\cos \alpha|, \lambda_{\text{eff}})$  plane, where  $\lambda_{\text{eff}} = \lambda_\alpha - \tan(\alpha) \frac{m_2}{v}$ , for singlet extensions of the SM with both explicit and spontaneous  $Z_2$  symmetry breaking. For the spontaneous case, the allowed range of  $|\cos \alpha|$  at 68% CL is between 0.92 and 1 (expected 0.86 and 1) and at 95% CL is between 0.79 and 1 (expected 0.82 and 1). The strongest constraints come from the  $b\bar{b}\tau\tau$  and  $b\bar{b}b\bar{b}$  boosted channels.

In the 2HDM additional bosons arise from the introduction of a second complex Higgs doublet that mixes with the SM Higgs doublet [8–11]. Four cases are considered, based on which of the two doublets the SM fermions couple to. For ‘Type-I’, the charged fermions only couple

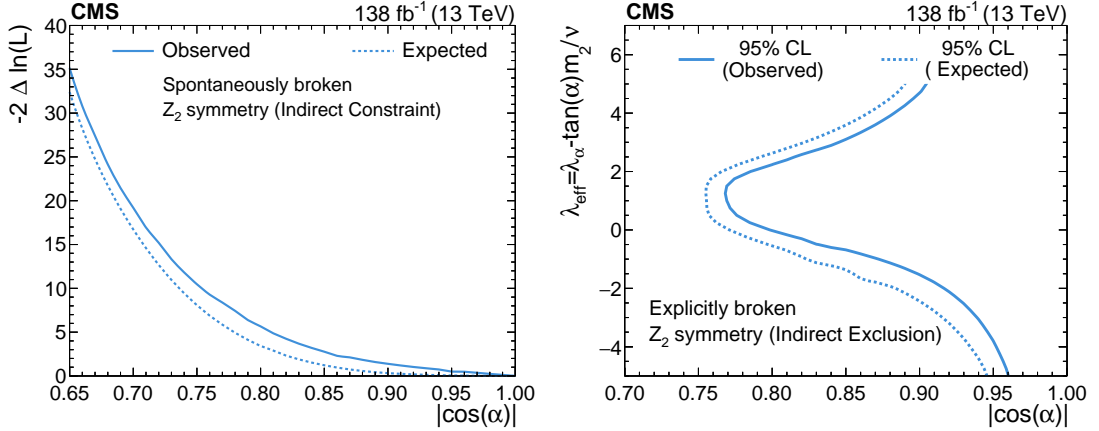


Figure 17: The  $-2\Delta \ln(L)$  scan for the combination of all channels as a function of  $|\cos \alpha|$  for singlet extensions of the SM with spontaneous  $Z_2$  symmetry breaking (left). The  $|\cos \alpha|$  is constrained at 95% CL between 0.79 and 1. The 95% CL contour of  $-2\Delta \ln(L)$  in the  $(|\cos \alpha|, \lambda_{\text{eff}})$  plane (right), where  $\lambda_{\text{eff}} = \lambda_\alpha - \tan(\alpha) \frac{m_2}{v}$ . The ranges of  $|\cos \alpha|$  and  $\lambda_{\text{eff}}$  are chosen to guarantee the validity of the models. The excluded regions are below and to the left of the curves shown.

to the second doublet, for ‘Type-II’, up- and down- type fermions couple to different doublets, in ‘Type-X’, charged leptons couple to the first doublet and both up- and down- type quarks couple to the second doublet, and finally for ‘Type-Y’ up-type quarks and charged leptons couple to the second doublet, while down type quarks couple to the first. Based on the mixing of the two doublets, five scalar bosons arise: a CP even scalar  $H$ , a CP odd scalar  $A$ , both of which are usually heavy; a light SM-like Higgs boson  $h$ , and two charged Higgs bosons  $H^\pm$ . The model is characterised by the masses of these five bosons, the mixing angle of the CP-even Higgs fields  $\alpha$ , the ratio of the vacuum expectation values in the two associated Higgs potentials  $\tan \beta = \frac{v_2}{v_1}$  and the mass mixing parameter  $m_{12}$ . The masses of the heavy scalars  $H$  and  $A$  are considered to be equal and noted as  $m_A$ .

Figures 18 and 19 show the results of the combination in the  $(m_H, \tan \beta)$  and  $(|\cos(\beta - \alpha)|, \tan \beta)$  planes, respectively. On the left are the observed and expected 95% CL contours for the 2HDM-I case, while the right shows the observed contours in all 2HDM cases. The excluded regions are below the curves shown. The results are derived under the assumption that we are not sensitive to the direct features of the resonant signal and that the interference effects between the resonant and nonresonant signal are negligible. Therefore, no interference effects are taken into account in this study.

Another simple extension of the SM is the minimal composite Higgs model (MCHM) [12–15]. Two cases are studied, MCHM<sub>4</sub> and MCHM<sub>5</sub>, where the SM fermions either transform as spinor or fundamental representations of the underlying SO(5) symmetry. These models are characterised by the compactness parameter  $\xi = (\frac{v}{f})^2$  with  $v$  being the vacuum expectation value and  $f$  the strong dynamics scale.

Figure 20 shows the observed and expected  $-2\Delta \ln(L)$  scan as a function of  $\xi$  for MCHM<sub>4</sub> and MCHM<sub>5</sub>. For MCHM<sub>4</sub>, the best fit is  $\xi = 0.0$ , while the observed (expected) 68 and 95% CL ranges are found to be between 0 and 0.18 (0 and 0.35) and 0 and 0.45 (0 and 0.55), respectively. The strongest constraints come from the  $WW\gamma\gamma$  and  $b\bar{b}WW$  channels. Likewise, for MCHM<sub>5</sub>, the best fit is  $\xi = 0.05$ , while the observed (expected) 68 and 95% CL ranges are found to be between 0 and 0.15 (0 and 0.13) and 0 and 0.26 (0 to 0.21), respectively. In this case, the strongest constraints come from the multilepton and  $WW\gamma\gamma$  channels.

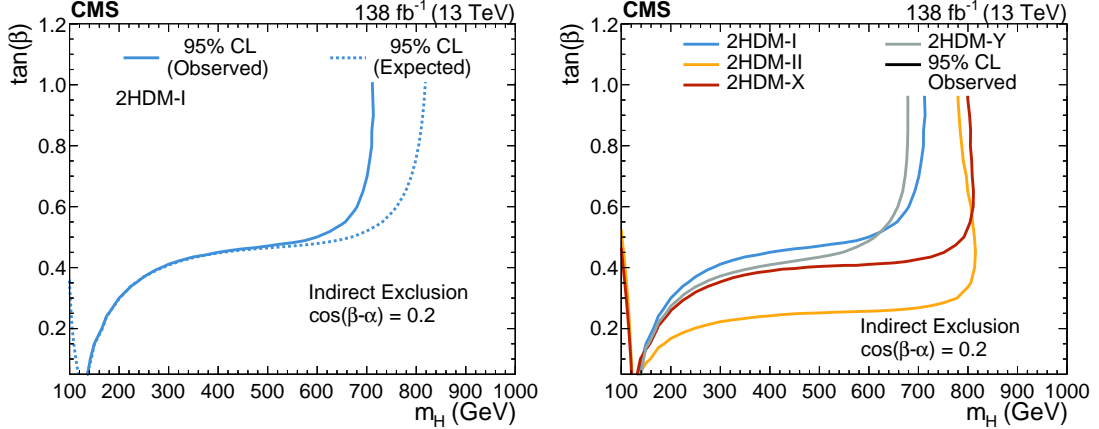


Figure 18: The 95% CL contour of  $-2\Delta \ln(L)$  for the combination of all channels in the  $(m_H, \tan \beta)$  plane for a fixed value of  $|\cos(\beta - \alpha)| = 0.2$  in the 2HDM-I model (left) and the four considered 2HDM models (right). In these and all other cases considered in this paper,  $m_H = m_A$ . The ranges of  $m_H$  and  $\tan \beta$  are chosen to guarantee the validity of the models. The excluded regions are below the curves shown. The value  $\tan \beta = 0.5$  is excluded for  $m_H > 800$  GeV for all models considered.

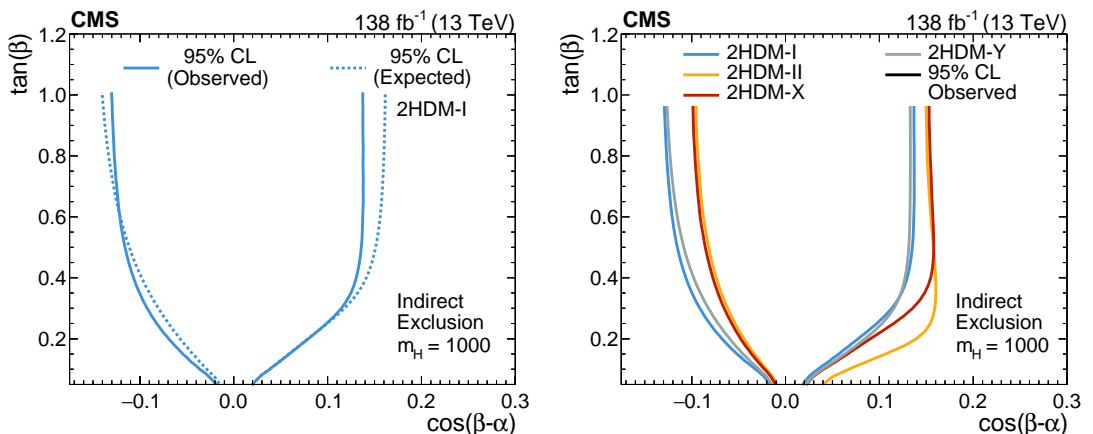


Figure 19: The 95% CL contour of  $-2\Delta \ln(L)$  for the combination of all channels in the  $(\cos(\beta - \alpha), \tan \beta)$  plane for a fixed value of  $m_H = 1000$  GeV in the 2HDM-I model (left) and the four considered 2HDM models (right). In these and all other cases considered in this paper,  $m_H = m_A$ . The ranges of  $\cos(\beta - \alpha)$  and  $\tan \beta$  are chosen to guarantee the validity of the model. The excluded regions are below the curves shown. The value  $\tan \beta = 0.5$  is excluded for  $\cos(\beta - \alpha) > 0.16$  and  $\cos(\beta - \alpha) < -0.13$  for all models considered.

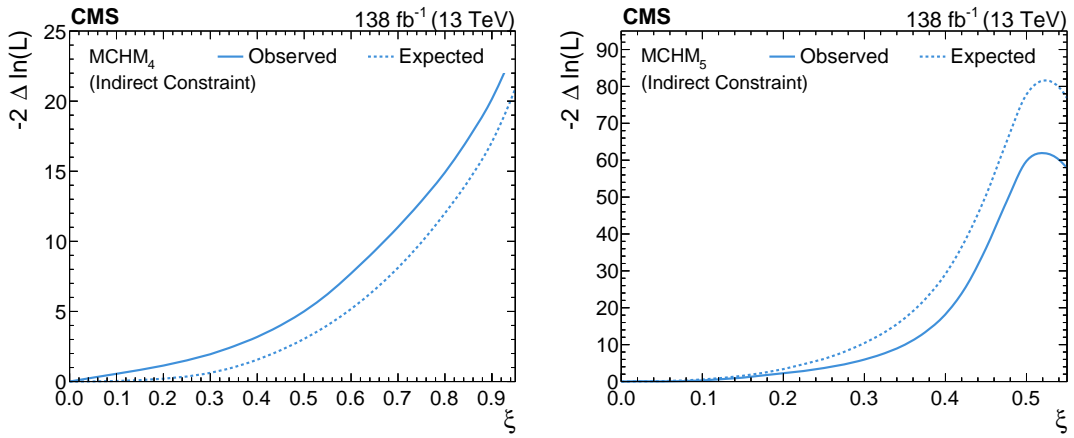


Figure 20: The  $-2\Delta \ln(L)$  scan for the combination of all channels as a function of  $\xi$  for MCHM<sub>4</sub> (left) and MCHM<sub>5</sub> (right). The range of  $\xi$  is chosen to guarantee the validity of the model. At 95% CL,  $\xi$  is constrained to be between 0 and 0.45 in MCHM<sub>4</sub> and 0 and 0.26 in MCHM<sub>5</sub>.

## 7 Projections for the HL-LHC

To further probe the SM, with particular interest in the Higgs boson self-coupling, the High-Luminosity LHC (HL-LHC) [114] operation is currently scheduled to begin in 2030. An integrated luminosity up to  $3000 \text{ fb}^{-1}$  is expected to be collected over the anticipated ten years of data taking. This unparalleled data set will open a unique window on the weak-scale nature of the universe, and the study of the Higgs boson self-coupling represents one of the most important targets of the HL-LHC. It is therefore of interest to extrapolate the current results to predict the sensitivity that can be achieved at the HL-LHC.

The results are projected to different integrated luminosity values, i.e. 300, 1000, 2000, and  $3000 \text{ fb}^{-1}$  to track the evolution during the data taking. In the projection studies, only the  $b\bar{b}\gamma\gamma$ ,  $b\bar{b}\tau\tau$ ,  $b\bar{b}b\bar{b}$ , multilepton, and  $b\bar{b}WW$  channels are included as they are the ones with the greatest sensitivity. The procedure for the statistical combination is the same as described in Sections 5 and 6.

The extrapolation of the Run-2 results to the HL-LHC follows the same strategy used in previous projections of Higgs boson searches and measurements [24]. For the projections to a certain integrated luminosity  $L$ , the Run-2 signal and background yields, as well as the selected data events, are scaled up by a factor  $k_L$  equal to the increase of integrated luminosity with respect to Run 2. The scaling of the data events is necessary for those analyses that rely on the data to properly model the backgrounds in the fit. The efficiency of the physics object reconstruction and identification is assumed to be the same as in Run 2. The same assumption is made regarding the experimental energy or momentum resolution of the physics objects. This is based on the premise that the upgraded CMS detector will ensure performance comparable to Run 2, despite the larger pileup and radiation damage to the detector components.

The exact nature and sizes of the systematic uncertainties in CMS during the HL-LHC are unknown. Therefore, we derive the projections in three different scenarios of systematic uncertainties:

- “S1”: The systematic uncertainties are assumed to be at the same level of Run 2.
- “S2”: The systematic uncertainties with a statistical origin, e.g. statistical uncertainties in data/MC scale factors, are reduced by a factor  $\sqrt{k_L}$ , until “floor” values are reached. The “floor” values prevent uncertainties from becoming unreasonably small and are based on studies in Ref. [24]. The theoretical uncertainties in the signal and background cross sections are halved to account for the expected progress in the theoretical calculations throughout the next years. The uncertainties originating from the limited size of the MC samples are also removed under the assumption of very large MC data sets.
- “stat. only”: No systematic uncertainties are considered in the fit.

It should be noted that the systematic uncertainties related to specific detector issues encountered in Run 2 have been removed from all three scenarios, including S1. The nominal scenario for the HL-LHC conditions is S2.

The treatment of the uncertainties common to multiple analysis channels is summarised in Table 5. The analysis-specific uncertainties are treated case by case.

The projected upper limits on the HH signal strength for the statistical combination of the considered HH channels at different integrated luminosities are shown in the left panel of Fig. 21. We will become sensitive to SM HH production at a 95% CL for integrated luminosities larger

Table 5: Treatment of most important common systematic uncertainties in the S2 scenario.

Uncertainty	Scaling with respect to Run 2
Theoretical uncertainties	1/2
Stat. uncertainties in MC simulation	Removed
b-tagging efficiency stat. component	$1/\sqrt{k_L}$
b-tagging efficiency (nonstat. component)	Unchanged
AK4 jet absolute energy scale	$\max(0.3, 1/\sqrt{k_L})$
AK4 jet energy scale dependence on flavour	$\max(0.5, 1/\sqrt{k_L})$
AK4 jet relative energy scale	$\max(0.2, 1/\sqrt{k_L})$
AK4 jet energy scale method	$1/\sqrt{k_L}$
AK4 jet energy resolution	$\max(0.5, 1/\sqrt{k_L})$
$E_T^{\text{miss}}$	$\max(0.5, 1/\sqrt{k_L})$
Luminosity	0.6
$\tau_h$ ID	Unchanged
$\tau_h$ energy scale	Unchanged
Pileup	Unchanged
Run-2 issues	Removed

than  $1000 \text{ fb}^{-1}$ , when the expected upper limit drops below one. The projections at  $3000 \text{ fb}^{-1}$  under the different systematic uncertainty scenarios are shown in the right panel of Fig. 21.

The projected  $\kappa_\lambda$  likelihood scans are shown in Fig. 22. In the S2 scenario, the expected 1 standard deviation uncertainty on  $\kappa_\lambda$  is  $+80\%/-60\%$  and  $+60\%/-50\%$  for an integrated luminosity of  $2000$  and  $3000 \text{ fb}^{-1}$ , respectively.

The expected significance for the HH signal strength assuming SM values for all parameters is summarised in Table 6. Before the end of the HL-LHC, the CMS experiment will have evidence for HH production with a significance of 3.5 standard deviations for  $2000 \text{ fb}^{-1}$  in the nominal systematic uncertainty scenario and assuming that the signal is SM-like. Figure 23 on the left shows the significance that can be achieved for the SM signal as a function of the integrated luminosity. On the right, the significance is shown as a function of  $\kappa_\lambda$ . The sensitivity to the HH signal varies with  $\kappa_\lambda$  due to the effects of the interference between the box and triangle diagrams, discussed in Section 1. The two diagrams have different kinematic properties, therefore, the interference varies not only the HH cross section but the HH signal acceptance rate as well. In particular, for  $\kappa_\lambda < 1$  and  $\kappa_\lambda > 5$ , the destructive interference is reduced, leading to an enhancement of the cross section relative to the SM expectation. In these regimes, evidence for the HH process could be established with smaller data sets compared to the SM case. The HH signal is suppressed for  $1 < \kappa_\lambda < 5$ , and the significance will be lower than expected, with minimum significance at  $\kappa_\lambda = 3.4$ . The projections presented here do not take into account potential improvements in triggering [115, 116], object reconstruction and selection such as b tagging, or analysis techniques. Historically, advancements in software and analysis methods have allowed us to exceed expectations, therefore the projections shown in this paper are most likely conservative. Results from Run 3 will also add valuable information regarding the potential improvements for measuring the HH process. If the trend of improvement continues, an observation of HH production by the end of the HL-LHC is within reach.

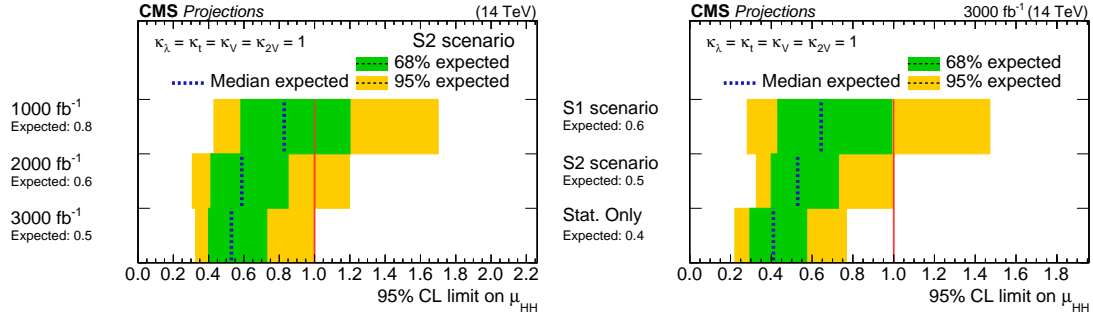


Figure 21: The expected upper limits at 95% CL on the HH signal strength from the combination of all the considered channels projected to different integrated luminosities (left), and under different assumptions on the systematic uncertainties for an integrated luminosity of  $3000 \text{ fb}^{-1}$  (right).

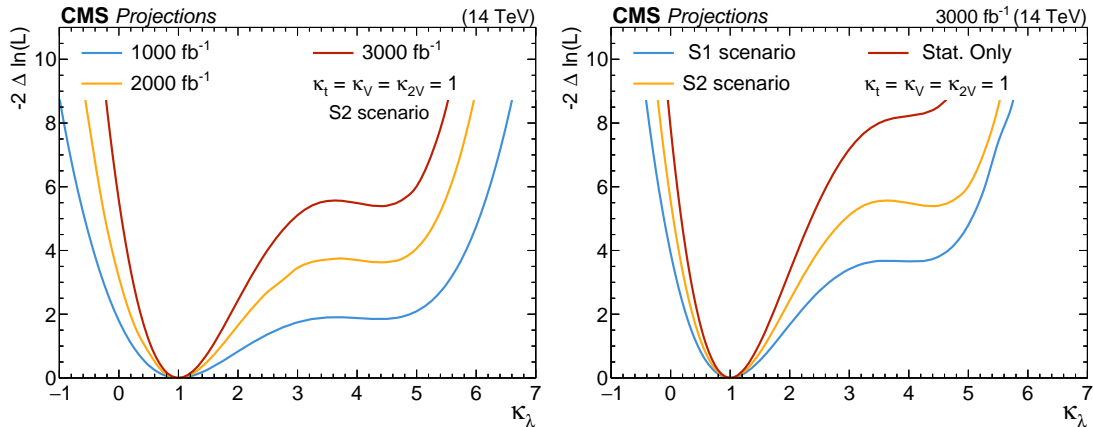


Figure 22: The expected  $-2\Delta \ln(L)$  scan as a function of coupling modifier  $\kappa_\lambda$  for the combination of all contributing channels, projected to different integrated luminosities (left), and under different assumptions on the systematic uncertainties for an integrated luminosity of  $3000 \text{ fb}^{-1}$  (right). All other parameters are fixed to their SM values.

Table 6: Expected significance for the HH signal projected to  $2000$  or  $3000 \text{ fb}^{-1}$  under different assumptions of systematic uncertainties.

	Significance ( $\sigma$ ) at $2000 \text{ fb}^{-1}$		Significance ( $\sigma$ ) at $3000 \text{ fb}^{-1}$	
	S2	Stat. only	S2	Stat. only
bb̄bb̄ resolved jets	1.0	1.4	1.2	1.7
bb̄bb̄ merged jets	1.8	1.9	2.2	2.3
bb̄ττ	1.9	2.1	2.4	2.6
bb̄γγ	2.0	2.0	2.4	2.5
bb̄WW	0.3	0.8	0.3	1.0
HH multilepton	0.4	0.6	0.5	0.8
Combination	3.5	3.9	4.2	4.8

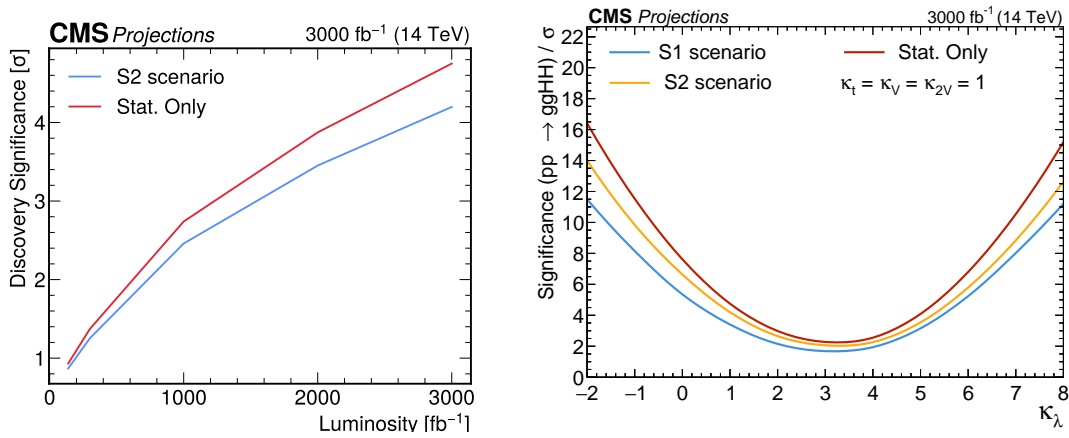


Figure 23: The expected signal significance as a function of integrated luminosity for the nominal systematic uncertainty scenario S2 and for the scenario with statistical uncertainties only (left). The expected signal significance as a function of  $\kappa_\lambda$  under different assumptions on the systematic uncertainties for an integrated luminosity of  $3000 \text{ fb}^{-1}$  (right).

## 8 Summary

A combined search for nonresonant Higgs boson pair (HH) production was performed using the proton-proton collision data set produced by the LHC at  $\sqrt{s} = 13$  TeV, and collected by the CMS experiment from 2016 to 2018 (Run 2), which corresponds to an integrated luminosity of  $138\text{ fb}^{-1}$ . Searches for HH production via gluon-gluon (ggF) and vector boson fusion (VBF) production, were carried out in the  $b\bar{b}\gamma\gamma$ ,  $b\bar{b}\tau\tau$ ,  $b\bar{b}b\bar{b}$ ,  $bbWW$ , and multilepton channels. Additionally, searches for ggF HH production were conducted in the  $b\bar{b}ZZ$  (with both Z bosons decaying to leptons),  $WW\gamma\gamma$ , and  $\tau\tau\gamma\gamma$  final states, which have clean signatures but relatively small branching fractions. We searched for the associated production mechanism with a vector boson in the  $b\bar{b}b\bar{b}$  final state, which has the largest branching fraction. The analyses of these channels were combined to probe the Higgs boson trilinear self-coupling and the quartic coupling between two vector bosons and two Higgs bosons (VVHH), and to search for beyond the standard model (SM) physics scenarios in the Higgs effective field theory (HEFT) approach.

The observed and expected upper limits at 95% confidence level (CL) on the cross section of ggF HH production were found to be 3.5 and 2.5 times the SM expectation, respectively. For VBF production, the observed and expected 95% CL upper limits are 79 and 91 times the SM expectation, respectively. When all other parameters are set to their SM values, we constrain the Higgs boson trilinear self-coupling modifier  $\kappa_\lambda$  in the range from  $-1.35$  to  $6.37$  at 95% CL (expected 95% CL range is  $-2.24$  to  $7.89$ ). Likewise, the VVHH coupling modifier  $\kappa_{2V}$  is constrained in the range from  $0.64$  to  $1.40$  ( $0.62$  to  $1.41$  expected).

Two-dimensional measurements were also performed, including simultaneous measurements of  $\kappa_\lambda$  and  $\kappa_{2V}$ ,  $\kappa_\lambda$  and the modifier of the Higgs boson coupling to the top quark ( $\kappa_t$ ), and  $\kappa_{2V}$  and the modifier of the Higgs boson coupling to vector bosons ( $\kappa_V$ ). The results are in agreement with the SM predictions.

Under the HEFT framework, the cross section of the nonresonant ggF HH pair production was parametrized as a function of anomalous couplings of the Higgs boson, involving the contact interactions between two Higgs and two top quarks, between two gluons and two Higgs bosons, and between two gluons and a Higgs boson. We performed searches for benchmark signals under different anomalous coupling scenarios and set upper limits on their cross sections at 95% CL. We exclude HH production at 95% CL when the coupling modifier of the contact interaction between two Higgs bosons and two top quarks is outside the range from  $-0.28$  to  $0.59$  (expected 95% CL range is  $-0.17$  to  $0.47$ ). The HEFT parametrisation is also exploited to study various ultraviolet complete models with an extended Higgs sector and set constraints on specific parameters.

These results constitute the most stringent limits and constraints obtained from the searches for nonresonant HH production using the LHC Run-2 data set collected by the CMS experiment. Extrapolating our current results to the integrated luminosity anticipated of the High-Luminosity LHC, it is expected to see first evidence for HH production with  $\approx 2000\text{ fb}^{-1}$  of data.

## Acknowledgments

We congratulate our colleagues in the CERN accelerator departments for the excellent performance of the LHC and thank the technical and administrative staffs at CERN and at other CMS institutes for their contributions to the success of the CMS effort. In addition, we gratefully

---

acknowledge the computing centres and personnel of the Worldwide LHC Computing Grid and other centres for delivering so effectively the computing infrastructure essential to our analyses. Finally, we acknowledge the enduring support for the construction and operation of the LHC, the CMS detector, and the supporting computing infrastructure provided by the following funding agencies: SC (Armenia), BMBWF and FWF (Austria); FNRS and FWO (Belgium); CNPq, CAPES, FAPERJ, FAPERGS, and FAPESP (Brazil); MES and BNSF (Bulgaria); CERN; CAS, MoST, and NSFC (China); MINCIENCIAS (Colombia); MSES and CSF (Croatia); RIF (Cyprus); SENESCYT (Ecuador); ERC PRG, TARISTU24-TK10 and MoER TK202 (Estonia); Academy of Finland, MEC, and HIP (Finland); CEA and CNRS/IN2P3 (France); SRNSF (Georgia); BMFTR, DFG, and HGF (Germany); GSRI (Greece); NKFH (Hungary); DAE and DST (India); IPM (Iran); SFI (Ireland); INFN (Italy); MSIT and NRF (Republic of Korea); MES (Latvia); LMTLT (Lithuania); MOE and UM (Malaysia); BUAP, CINVESTAV, CONACYT, LNS, SEP, and UASLP-FAI (Mexico); MOS (Montenegro); MBIE (New Zealand); PAEC (Pakistan); MES, NSC, and NAWA (Poland); FCT (Portugal); MESTD (Serbia); MICIU/AEI and PCTI (Spain); MOSTR (Sri Lanka); Swiss Funding Agencies (Switzerland); MST (Taipei); MHESI (Thailand); TUBITAK and TENMAK (Türkiye); NASU (Ukraine); STFC (United Kingdom); DOE and NSF (USA).

Individuals have received support from the Marie-Curie programme and the European Research Council and Horizon 2020 Grant, contract Nos. 675440, 724704, 752730, 758316, 765710, 824093, 101115353, 101002207, 101001205, and COST Action CA16108 (European Union); the Leventis Foundation; the Alfred P. Sloan Foundation; the Alexander von Humboldt Foundation; the Science Committee, project no. 22rl-037 (Armenia); the Fonds pour la Formation à la Recherche dans l'Industrie et dans l'Agriculture (FRIA) and Fonds voor Wetenschappelijk Onderzoek contract No. 1228724N (Belgium); the Beijing Municipal Science & Technology Commission, No. Z191100007219010, the Fundamental Research Funds for the Central Universities, the Ministry of Science and Technology of China under Grant No. 2023YFA1605804, the Natural Science Foundation of China under Grant No. 12061141002 and USTC Research Funds of the Double First-Class Initiative No. YD2030002017 (China); the Ministry of Education, Youth and Sports (MEYS) of the Czech Republic; the Shota Rustaveli National Science Foundation, grant FR-22-985 (Georgia); the Deutsche Forschungsgemeinschaft (DFG), among others, under Germany's Excellence Strategy – EXC 2121 "Quantum Universe" – 390833306, and under project number 400140256 - GRK2497; the Hellenic Foundation for Research and Innovation (HFRI), Project Number 2288 (Greece); the Hungarian Academy of Sciences, the New National Excellence Program - ÚNKP, the NKFH research grants K 131991, K 133046, K 138136, K 143460, K 143477, K 146913, K 146914, K 147048, 2020-2.2.1-ED-2021-00181, TKP2021-NKTA-64, and 2021-4.1.2-NEMZ-KI-2024-00036 (Hungary); the Council of Science and Industrial Research, India; ICSC – National Research Centre for High Performance Computing, Big Data and Quantum Computing, FAIR – Future Artificial Intelligence Research, and CUP I53D23001070006 (Mission 4 Component 1), funded by the NextGenerationEU program (Italy); the Latvian Council of Science; the Ministry of Education and Science, project no. 2022/WK/14, and the National Science Center, contracts Opus 2021/41/B/ST2/01369, 2021/43/B/ST2/01552, 2023/49/B/ST2/03273, and the NAWA contract BPN/PPO/2021/1/00011 (Poland); the Fundação para a Ciência e a Tecnologia, grant CECIND/01334/2018 (Portugal); the National Priorities Research Program by Qatar National Research Fund; MICIU/AEI/10.13039/501100011033, ERDF/EU, "European Union NextGenerationEU/PRTR", and Programa Severo Ochoa del Principado de Asturias (Spain); the Chulalongkorn Academic into Its 2nd Century Project Advancement Project, the National Science, Research and Innovation Fund program IND\_FF\_68\_369\_2300\_097, and the Program Management Unit for Human Resources & Institutional Development, Research and Innovation, grant

B39G680009 (Thailand); the Kavli Foundation; the Nvidia Corporation; the SuperMicro Corporation; the Welch Foundation, contract C-1845; and the Weston Havens Foundation (USA).

## References

- [1] CMS Collaboration, “Observation of a new boson at a mass of 125 GeV with the CMS experiment at the LHC”, *Phys. Lett. B* **716** (2012) 30, doi:10.1016/j.physletb.2012.08.021, arXiv:1207.7235.
- [2] CMS Collaboration, “Observation of a new boson with mass near 125 GeV in pp collisions at  $\sqrt{s} = 7$  and 8 TeV”, *JHEP* **06** (2013) 081, doi:10.1007/JHEP06(2013)081, arXiv:1303.4571.
- [3] ATLAS Collaboration, “Observation of a new particle in the search for the standard model Higgs boson with the ATLAS detector at the lhc”, *Phys. Lett. B* **716** (2012) 1, doi:10.1016/j.physletb.2012.08.020, arXiv:1207.7214.
- [4] CMS Collaboration, “A portrait of the Higgs boson by the CMS experiment ten years after the discovery”, *Nature* **607** (2022) 60, doi:10.1038/s41586-022-04892-x, arXiv:2207.00043. [Erratum: doi:10.1038/s41586-023-06164-8].
- [5] ATLAS Collaboration, “A detailed map of Higgs boson interactions by the ATLAS experiment ten years after the discovery”, *Nature* **607** (2022) 52, doi:10.1038/s41586-022-04893-w, arXiv:2207.00092. [Erratum: doi:10.1038/s41586-023-06248-5].
- [6] S. Dawson and C. W. Murphy, “Standard model EFT and extended scalar sectors”, *Phys. Rev. D* **96** (2017) 015041, doi:10.1103/PhysRevD.96.015041, arXiv:1704.07851.
- [7] J. de Blas, M. Chala, M. Perez-Victoria, and J. Santiago, “Observable effects of general new scalar particles”, *JHEP* **04** (2015) 078, doi:10.1007/JHEP04(2015)078, arXiv:1412.8480.
- [8] T. D. Lee, “A theory of spontaneous  $T$  violation”, *Phys. Rev. D* **8** (1973) 1226, doi:10.1103/PhysRevD.8.1226.
- [9] G. C. Branco et al., “Theory and phenomenology of two-Higgs-doublet models”, *Phys. Rep.* **516** (2012) 1, doi:10.1016/j.physrep.2012.02.002, arXiv:1106.0034.
- [10] H. E. Haber and O. Stål, “New LHC benchmarks for the  $CP$ -conserving two-Higgs-doublet model”, *Eur. Phys. J. C* **75** (2015) 491, doi:10.1140/epjc/s10052-015-3697-x, arXiv:1507.04281. [Erratum: doi:10.1140/epjc/s10052-016-4151-4].
- [11] F. Kling, J. M. No, and S. Su, “Anatomy of exotic Higgs decays in 2HDM”, *JHEP* **09** (2016) 093, doi:10.1007/JHEP09(2016)093, arXiv:1604.01406.
- [12] G. F. Giudice, C. Grojean, A. Pomarol, and R. Rattazzi, “The strongly-interacting light Higgs”, *JHEP* **06** (2007) 045, doi:10.1088/1126-6708/2007/06/045, arXiv:hep-ph/0703164.
- [13] R. Gröber and M. Mühlleitner, “Composite Higgs boson pair production at the LHC”, *JHEP* **06** (2011) 020, doi:10.1007/JHEP06(2011)020, arXiv:1012.1562.

- [14] R. Contino et al., “Effective Lagrangian for a light Higgs-like scalar”, *JHEP* **07** (2013) 035, doi:10.1007/JHEP07(2013)035, arXiv:1303.3876.
- [15] R. Contino, “The Higgs as a composite Nambu–Goldstone boson”, in *Theoretical Advanced Study Institute in Elementary Particle Physics: Physics of the Large and the Small*, p. 235. 2011. arXiv:1005.4269. doi:10.1142/9789814327183\_0005.
- [16] P. Huang, A. J. Long, and L.-T. Wang, “Probing the electroweak phase transition with Higgs factories and gravitational waves”, *Phys. Rev. D* **94** (2016) 075008, doi:10.1103/PhysRevD.94.075008, arXiv:1608.06619.
- [17] M. J. Ramsey-Musolf, I. Tenkanen, Tuomas V. and V. Q. Tran, “Refining gravitational wave and collider physics dialogue via singlet scalar extension”, 2024. arXiv:2409.17554.
- [18] A. Mazumdar and G. White, “Review of cosmic phase transitions: Their significance and experimental signatures”, *Rep. Prog. Phys.* **82** (2019) 076901, doi:10.1088/1361-6633/ab1f55, arXiv:1811.01948.
- [19] W. Zhang et al., “Probing electroweak phase transition in the singlet standard model via  $bb\gamma\gamma$  and  $4\ell$  channels”, *JHEP* **12** (2023) 018, doi:10.1007/JHEP12(2023)018, arXiv:2303.03612.
- [20] A. V. Bednyakov, A. F. Pikelner, and V. N. Velizhanin, “Stability of the electroweak vacuum: Gauge independence and radiative corrections”, *Phys. Rev. Lett.* **115** (2015) 201802, doi:10.1103/PhysRevLett.115.201802, arXiv:1507.08833.
- [21] P. Basler, L. Biermann, M. Mühlleitner et al., “Electroweak baryogenesis in the CP-violating two-Higgs doublet model”, *Eur. Phys. J. C* **83** (2023) 57, doi:10.1140/epjc/s10052-023-11192-9, arXiv:2108.03580.
- [22] D. E. Morrissey and M. J. Ramsey-Musolf, “Electroweak baryogenesis: A review”, *New J. Phys.* **14** (2012) 125003, doi:10.1088/1367-2630/14/12/125003, arXiv:1206.2942.
- [23] T. Plehn and M. Rauch, “The quartic Higgs coupling at hadron colliders”, *Phys. Rev. D* **72** (2005) 053008, doi:10.1103/PhysRevD.72.053008, arXiv:hep-ph/0507321.
- [24] A. Dainese et al., “Report from Working Group 2: Higgs physics at the HL-LHC and HE-LHC”, *CERN Yellow Rep. Monogr.* **7** (2019) 221, doi:10.23731/CYRM-2019-007.221, arXiv:1902.00134.
- [25] M. Chiesa et al., “Measuring the quartic Higgs self-coupling at a multi-TeV muon collider”, *JHEP* **09** (2020) 098, doi:10.1007/JHEP09(2020)098, arXiv:2003.13628.
- [26] H. Abouabid et al., “HHH whitepaper”, *Eur. Phys. J. C* **84** (2024) 1183, doi:10.1140/epjc/s10052-024-13376-3, arXiv:2407.03015.
- [27] S. Borowka et al., “Higgs boson pair production in gluon fusion at next-to-leading order with full top-quark mass dependence”, *Phys. Rev. Lett.* **117** (2016) 012001, doi:10.1103/PhysRevLett.117.079901, arXiv:1604.06447. [Erratum: doi:10.1103/PhysRevLett.117.079901].

- [28] J. Baglio et al., “Gluon fusion into Higgs pairs at NLO QCD and the top mass scheme”, *Eur. Phys. J. C* **79** (2019) 459, doi:10.1140/epjc/s10052-019-6973-3, arXiv:1811.05692.
- [29] F. A. Dreyer and A. Karlberg, “Vector-boson fusion Higgs pair production at N<sup>3</sup>LO”, *Phys. Rev. D* **98** (2018) 114016, doi:10.1103/PhysRevD.98.114016, arXiv:1811.07906.
- [30] M. Grazzini et al., “Higgs boson pair production at NNLO with top quark mass effects”, *JHEP* **05** (2018) 059, doi:10.1007/JHEP05(2018)059, arXiv:1803.02463.
- [31] L. Alasfar et al., “Effective field theory descriptions of Higgs boson pair production”, *SciPost Phys. Comm. Rep.* (2024) 2, doi:10.21468/SciPostPhysCommRep.2, arXiv:2304.01968.
- [32] ATLAS Collaboration, “Combination of searches for Higgs boson pair production in pp collisions at  $\sqrt{s} = 13$  TeV with the ATLAS detector”, *Phys. Rev. Lett.* **133** (2024) 101801, doi:10.1103/PhysRevLett.133.101801, arXiv:2406.09971.
- [33] “HEPData record for this analysis”, 2025. doi:10.17182/hepdata.165282.
- [34] CMS Collaboration, “The CMS experiment at the CERN LHC”, *JINST* **3** (2008) S08004, doi:10.1088/1748-0221/3/08/S08004.
- [35] CMS Collaboration, “Development of the CMS detector for the CERN LHC Run 3”, *JINST* **19** (2024) P05064, doi:10.1088/1748-0221/19/05/P05064, arXiv:2309.05466.
- [36] CMS Collaboration, “Performance of the CMS Level-1 trigger in proton-proton collisions at  $\sqrt{s} = 13$  TeV”, *JINST* **15** (2020) P10017, doi:10.1088/1748-0221/15/10/P10017, arXiv:2006.10165.
- [37] CMS Collaboration, “The CMS trigger system”, *JINST* **12** (2017) P01020, doi:10.1088/1748-0221/12/01/P01020, arXiv:1609.02366.
- [38] CMS Collaboration, “Performance of the CMS high-level trigger during LHC Run 2”, *JINST* **19** (2024) P11021, doi:10.1088/1748-0221/19/11/P11021, arXiv:2410.17038.
- [39] CMS Collaboration, “Electron and photon reconstruction and identification with the CMS experiment at the CERN LHC”, *JINST* **16** (2021) P05014, doi:10.1088/1748-0221/16/05/P05014, arXiv:2012.06888.
- [40] CMS Collaboration, “Performance of the CMS muon detector and muon reconstruction with proton-proton collisions at  $\sqrt{s} = 13$  TeV”, *JINST* **13** (2018) P06015, doi:10.1088/1748-0221/13/06/P06015, arXiv:1804.04528.
- [41] CMS Collaboration, “Description and performance of track and primary-vertex reconstruction with the CMS tracker”, *JINST* **9** (2014) P10009, doi:10.1088/1748-0221/9/10/P10009, arXiv:1405.6569.
- [42] CMS Collaboration, “Particle-flow reconstruction and global event description with the CMS detector”, *JINST* **12** (2017) P10003, doi:10.1088/1748-0221/12/10/P10003, arXiv:1706.04965.

- [43] CMS Collaboration, “Technical proposal for the Phase-II upgrade of the Compact Muon Solenoid”, CMS Technical Proposal CERN-LHCC-2015-010, CMS-TDR-15-02, 2015.
- [44] M. Cacciari, G. P. Salam, and G. Soyez, “The anti- $k_T$  jet clustering algorithm”, *JHEP* **04** (2008) 063, doi:10.1088/1126-6708/2008/04/063, arXiv:0802.1189.
- [45] M. Cacciari, G. P. Salam, and G. Soyez, “FastJet user manual”, *Eur. Phys. J. C* **72** (2012) 1896, doi:10.1140/epjc/s10052-012-1896-2, arXiv:1111.6097.
- [46] CMS Collaboration, “Performance of missing transverse momentum reconstruction in proton-proton collisions at  $\sqrt{s} = 13$  TeV using the CMS detector”, *JINST* **14** (2019) P07004, doi:10.1088/1748-0221/14/07/P07004, arXiv:1903.06078.
- [47] G. Heinrich et al., “Probing the trilinear Higgs boson coupling in di-Higgs production at NLO QCD including parton shower effects”, *JHEP* **06** (2019) 066, doi:10.1007/JHEP06(2019)066, arXiv:1903.08137.
- [48] D. de Florian et al., “Anomalous couplings in Higgs-boson pair production at approximate NNLO QCD”, *JHEP* **09** (2021) 161, doi:10.1007/JHEP09(2021)161, arXiv:2106.14050.
- [49] A. Carvalho et al., “On the reinterpretation of non-resonant searches for Higgs boson pairs”, *JHEP* **02** (2021) 049, doi:10.1007/JHEP02(2021)049, arXiv:1710.08261.
- [50] A. Carvalho et al., “Higgs pair production: Choosing benchmarks with cluster analysis”, *JHEP* **04** (2016) 126, doi:10.1007/JHEP04(2016)126, arXiv:1507.02245.
- [51] M. Capozi and G. Heinrich, “Exploring anomalous couplings in Higgs boson pair production through shape analysis”, *JHEP* **03** (2020) 091, doi:10.1007/JHEP03(2020)091, arXiv:1908.08923.
- [52] CMS Collaboration, “Constraints on the Higgs boson self-coupling from the combination of single and double Higgs boson production in proton-proton collisions at  $\sqrt{s} = 13$  TeV”, *Phys. Lett. B* **861** (2025) 139210, doi:10.1016/j.physletb.2024.139210, arXiv:2407.13554.
- [53] P. Nason, “A new method for combining NLO QCD with shower Monte Carlo algorithms”, *JHEP* **11** (2004) 040, doi:10.1088/1126-6708/2004/11/040, arXiv:hep-ph/0409146.
- [54] S. Frixione, P. Nason, and C. Oleari, “Matching NLO QCD computations with parton shower simulations: The POWHEG method”, *JHEP* **11** (2007) 070, doi:10.1088/1126-6708/2007/11/070, arXiv:0709.2092.
- [55] S. Alioli, P. Nason, C. Oleari, and E. Re, “A general framework for implementing NLO calculations in shower Monte Carlo programs: The POWHEG BOX”, *JHEP* **06** (2010) 043, doi:10.1007/JHEP06(2010)043, arXiv:1002.2581.
- [56] S. Amoroso et al., “Les Houches 2019: Physics at TeV colliders: Standard model working group report”, in *Proc. 11th Les Houches Workshop on Physics at TeV Colliders: PhysTeV Les Houches*. 2020. arXiv:2003.01700.

[57] J. Alwall et al., “The automated computation of tree-level and next-to-leading order differential cross sections, and their matching to parton shower simulations”, *JHEP* **07** (2014) 079, doi:10.1007/JHEP07(2014)079, arXiv:1405.0301.

[58] J. Alwall et al., “Comparative study of various algorithms for the merging of parton showers and matrix elements in hadronic collisions”, *Eur. Phys. J. C* **53** (2007) 473, doi:10.1140/epjc/s10052-007-0490-5, arXiv:0706.2569.

[59] R. Frederix and S. Frixione, “Merging meets matching in MC@NLO”, *JHEP* **12** (2012) 061, doi:10.1007/JHEP12(2012)061, arXiv:1209.6215.

[60] F. A. Dreyer and A. Karlberg, “Fully differential vector-boson fusion Higgs pair production at next-to-next-to-leading order”, *Phys. Rev. D* **99** (2019) 074028, doi:10.1103/PhysRevD.99.074028, arXiv:1811.07918.

[61] J. Baglio et al., “The measurement of the Higgs self-coupling at the LHC: theoretical status”, *JHEP* **04** (2013) 151, doi:10.1007/JHEP04(2013)151, arXiv:1212.5581.

[62] T. Sjöstrand, S. Mrenna, and P. Z. Skands, “A brief introduction to PYTHIA 8.1”, *Comput. Phys. Commun.* **178** (2008) 852, doi:10.1016/j.cpc.2008.01.036, arXiv:0710.3820.

[63] NNPDF Collaboration, “Parton distributions with QED corrections”, *Nucl. Phys. B* **877** (2013) 290, doi:10.1016/j.nuclphysb.2013.10.010, arXiv:1308.0598.

[64] NNPDF Collaboration, “Parton distributions for the LHC Run II”, *JHEP* **04** (2015) 040, doi:10.1007/JHEP04(2015)040, arXiv:1410.8849.

[65] NNPDF Collaboration, “Parton distributions from high-precision collider data”, *Eur. Phys. J. C* **77** (2017) 663, doi:10.1140/epjc/s10052-017-5199-5, arXiv:1706.00428.

[66] GEANT4 Collaboration, “GEANT4—a simulation toolkit”, *Nucl. Instrum. Meth. A* **506** (2003) 250, doi:10.1016/S0168-9002(03)01368-8.

[67] CMS Collaboration, “Search for Higgs Boson Pair Production in the Four b Quark Final State in Proton-Proton Collisions at  $\sqrt{s} = 13$  TeV”, *Phys. Rev. Lett.* **129** (2022) 081802, doi:10.1103/PhysRevLett.129.081802, arXiv:2202.09617.

[68] CMS Collaboration, “Search for nonresonant pair production of highly energetic Higgs bosons decaying to bottom quarks”, *Phys. Rev. Lett.* **131** (2023) 041803, doi:10.1103/PhysRevLett.131.041803, arXiv:2205.06667.

[69] CMS Collaboration, “Search for Higgs boson pair production with one associated vector boson in proton-proton collisions at  $\sqrt{s} = 13$  TeV”, *JHEP* **10** (2024) 061, doi:10.1007/JHEP10(2024)061, arXiv:2404.08462.

[70] CMS Collaboration, “Search for nonresonant Higgs boson pair production in final state with two bottom quarks and two tau leptons in proton-proton collisions at  $\sqrt{s} = 13$  TeV”, *Phys. Lett. B* **842** (2023) 137531, doi:10.1016/j.physletb.2022.137531, arXiv:2206.09401.

[71] CMS Collaboration, “Search for nonresonant Higgs boson pair production in final states with two bottom quarks and two photons in proton-proton collisions at  $\sqrt{s} = 13$  TeV”, *JHEP* **03** (2021) 257, doi:10.1007/JHEP03(2021)257, arXiv:2011.12373.

[72] CMS Collaboration, “Search for Higgs boson pair production in the  $b\bar{b}W^+W^-$  decay mode in proton-proton collisions at  $\sqrt{s} = 13$  TeV”, *JHEP* **07** (2024) 293, doi:10.1007/JHEP07(2024)293, arXiv:2403.09430.

[73] CMS Collaboration, “Search for Higgs boson pairs decaying to  $WW^*WW^*$ ,  $WW^*\tau\tau$ , and  $\tau\tau\tau\tau$  in proton-proton collisions at  $\sqrt{s} = 13$  TeV”, *JHEP* **07** (2023) 095, doi:10.1007/JHEP07(2023)095, arXiv:2206.10268.

[74] CMS Collaboration, “Search for the nonresonant and resonant production of a Higgs boson in association with an additional scalar boson in the  $\gamma\gamma\tau\tau$  final state in proton-proton collisions at  $\sqrt{s} = 13$  TeV”, 2025. arXiv:2506.23012. Submitted to *JHEP*.

[75] CMS Collaboration, “Search for nonresonant Higgs boson pair production in the four leptons plus two b jets final state in proton-proton collisions at  $\sqrt{s} = 13$  TeV”, *JHEP* **06** (2023) 130, doi:10.1007/JHEP06(2023)130, arXiv:2206.10657.

[76] E. Bols et al., “Jet flavour classification using DEEPJET”, *JINST* **15** (2020) P12012, doi:10.1088/1748-0221/15/12/P12012, arXiv:2008.10519.

[77] CMS Collaboration, “A deep neural network for simultaneous estimation of b jet energy and resolution”, *Comput. Softw. Big Sci.* **4** (2020) 10, doi:10.1007/s41781-020-00041-z, arXiv:1912.06046.

[78] A. J. Larkoski, S. Marzani, G. Soyez, and J. Thaler, “Soft drop”, *JHEP* **05** (2014) 146, doi:10.1007/JHEP05(2014)146, arXiv:1402.2657.

[79] I. Henrion et al., “Neural message passing for jet physics”, in *Deep Learning for Physical Sciences Workshop at 31st Conf. on Neural Information Processing Systems*. Long Beach, CA, USA, 2017.

[80] H. Qu and L. Gouskos, “Jet tagging via particle clouds”, *Phys. Rev. D* **101** (2020) 056019, doi:10.1103/PhysRevD.101.056019, arXiv:1902.08570.

[81] E. A. Moreno et al., “JEDI-net: A jet identification algorithm based on interaction networks”, *Eur. Phys. J. C* **80** (2020) 58, doi:10.1140/epjc/s10052-020-7608-4, arXiv:1908.05318.

[82] E. A. Moreno et al., “Interaction networks for the identification of boosted  $H \rightarrow b\bar{b}$  decays”, *Phys. Rev. D* **102** (2020) 012010, doi:10.1103/PhysRevD.102.012010, arXiv:1909.12285.

[83] CMS Collaboration, “Performance of heavy-flavour jet identification in boosted topologies in proton-proton collisions at  $\sqrt{s} = 13$  TeV”, CMS Physics Analysis Summary CMS-PAS-BTV-22-001, 2023.

[84] CMS Collaboration, “Mass regression of highly-boosted jets using graph neural networks”, CMS Detector Performance Note CMS-DP-2021-017, 2021.

[85] CMS Collaboration, “Search for a massive resonance decaying to a pair of Higgs bosons in the four b quark final state in proton-proton collisions at  $\sqrt{s} = 13$  TeV”, *Phys. Lett. B* **781** (2018) 244, doi:10.1016/j.physletb.2018.03.084, arXiv:1710.04960.

[86] CMS Collaboration, “Search for production of Higgs boson pairs in the four b quark final state using large-area jets in proton-proton collisions at  $\sqrt{s} = 13$  TeV”, *JHEP* **01** (2019) 040, doi:10.1007/JHEP01(2019)040, arXiv:1808.01473.

[87] CMS Collaboration, “Inclusive search for highly boosted Higgs bosons decaying to bottom quark-antiquark pairs in proton-proton collisions at  $\sqrt{s} = 13$  TeV”, *JHEP* **12** (2020) 85, doi:10.1007/JHEP12(2020)085, arXiv:2006.13251.

[88] CMS Collaboration, “Identification of heavy, energetic, hadronically decaying particles using machine-learning techniques”, *JINST* **15** (2020) P06005, doi:10.1088/1748-0221/15/06/P06005, arXiv:2004.08262.

[89] CMS Collaboration, “Identification of hadronic tau lepton decays using a deep neural network”, *JINST* **17** (2022) P07023, doi:10.1088/1748-0221/17/07/P07023, arXiv:2201.08458.

[90] L. Bianchini et al., “Reconstruction of the Higgs mass in events with Higgs bosons decaying into a pair of  $\tau$  leptons using matrix element techniques”, *Nucl. Instrum. Meth. A* **862** (2017) 54, doi:10.1016/j.nima.2017.05.001, arXiv:1603.05910.

[91] CMS Collaboration, “Evidence for associated production of a Higgs boson with a top quark pair in final states with electrons, muons, and hadronically decaying  $\tau$  leptons at  $\sqrt{s} = 13$  TeV”, *JHEP* **08** (2018) 066, doi:10.1007/JHEP08(2018)066, arXiv:1803.05485.

[92] H. Qu, C. Li, and S. Qian, “Particle transformer for jet tagging”, in *Proc. 39th Int. Conf. on Machine Learning*, K. Chaudhuri et al., eds., volume 162, p. 18281. 2022. arXiv:2202.03772.

[93] CMS Collaboration, “Particle transformers for identifying Lorentz-boosted Higgs bosons decaying to a pair of W bosons”, CMS Physics Analysis Summary CMS-PAS-JME-25-001, 2025.

[94] CMS Collaboration, “A new method for correcting the substructure of multi-prong jets using Lund jet plane reweighting in the CMS experiment”, CMS Physics Analysis Summary CMS-PAS-JME-23-001, 2025.

[95] F. A. Dreyer, G. P. Salam, and G. Soyez, “The Lund jet plane”, *JHEP* **12** (2018) 064, doi:10.1007/JHEP12(2018)064, arXiv:1807.04758.

[96] CMS Collaboration, “Measurement of the Higgs boson production rate in association with top quarks in final states with electrons, muons, and hadronically decaying tau leptons at  $\sqrt{s} = 13$  TeV”, *Eur. Phys. J. C* **81** (2021) 378, doi:10.1140/epjc/s10052-021-09014-x, arXiv:2011.03652.

[97] LHC Higgs Cross Section Working Group, “Handbook of LHC Higgs Cross Sections: 4. Deciphering the nature of the Higgs sector”, *CERN Yellow Rep. Monogr.* **2** (2017) doi:10.23731/CYRM-2017-002, arXiv:1610.07922.

[98] S. Manzoni et al., “Taming a leading theoretical uncertainty in HH measurements via accurate simulations for  $bbH$  production”, *JHEP* **09** (2023) 179, doi:10.1007/JHEP09(2023)179, arXiv:2307.09992.

[99] J. Baglio et al., “ $gg \rightarrow HH$ : Combined uncertainties”, *Phys. Rev. D* **103** (2021) 056002, doi:10.1103/PhysRevD.103.056002, arXiv:2008.11626.

- [100] L.-S. Ling et al., “NNLO QCD corrections to Higgs pair production via vector boson fusion at hadron colliders”, *Phys. Rev. D* **89** (2014) 073001, doi:10.1103/PhysRevD.89.073001, arXiv:1401.7754.
- [101] M. Czakon et al., “Top-pair production at the LHC through NNLO QCD and NLO EW”, *JHEP* **10** (2017) 186, doi:10.1007/JHEP10(2017)186, arXiv:1705.04105.
- [102] CMS Collaboration, “Precision luminosity measurement in proton-proton collisions at  $\sqrt{s} = 13$  TeV in 2015 and 2016 at CMS”, *Eur. Phys. J. C* **81** (2021) 800, doi:10.1140/epjc/s10052-021-09538-2, arXiv:2104.01927.
- [103] CMS Collaboration, “CMS luminosity measurement for the 2017 data-taking period at  $\sqrt{s} = 13$  TeV”, CMS Physics Analysis Summary CMS-PAS-LUM-17-004, 2018.
- [104] CMS Collaboration, “CMS luminosity measurement for the 2018 data-taking period at  $\sqrt{s} = 13$  TeV”, CMS Physics Analysis Summary CMS-PAS-LUM-18-002, 2019.
- [105] CMS Collaboration, “Measurement of the inelastic proton-proton cross section at  $\sqrt{s} = 13$  TeV”, *JHEP* **07** (2018) 161, doi:10.1007/JHEP07(2018)161, arXiv:1802.02613.
- [106] R. Barlow and C. Beeston, “Fitting using finite Monte Carlo samples”, *Comput. Phys. Commun.* **77** (1993) 219, doi:10.1016/0010-4655(93)90005-W.
- [107] ATLAS and CMS Collaborations, and LHC Higgs Combination Group, “Procedure for the LHC Higgs boson search combination in Summer 2011”, Technical Report CMS-NOTE-2011-005, ATL-PHYS-PUB-2011-11, 2011.
- [108] G. Cowan, K. Cranmer, E. Gross, and O. Vitells, “Asymptotic formulae for likelihood-based tests of new physics”, *Eur. Phys. J. C* **71** (2011) 1554, doi:10.1140/epjc/s10052-011-1554-0, arXiv:1007.1727. [Erratum: doi:10.1140/epjc/s10052-011-1554-0].
- [109] T. Junk, “Confidence level computation for combining searches with small statistics”, *Nucl. Instrum. Meth. A* **434** (1999) 435, doi:10.1016/S0168-9002(99)00498-2, arXiv:hep-ex/9902006.
- [110] A. L. Read, “Presentation of search results: the  $CL_s$  technique”, *J. Phys. G* **28** (2002) 2693, doi:10.1088/0954-3899/28/10/313.
- [111] CMS Collaboration, “The CMS statistical analysis and combination tool: COMBINE”, *Comput. Softw. Big Sci.* **8** (2024) 19, doi:10.1007/s41781-024-00121-4, arXiv:2404.06614.
- [112] W. Verkerke and D. P. Kirkby, “The RooFit toolkit for data modeling”, *eConf* (2003) arXiv:physics/0306116.
- [113] L. Moneta et al., “The RooStats Project”, *PoS ACAT2010* (2010) 057, doi:10.22323/1.093.0057, arXiv:1009.1003.
- [114] I. Zurbano Fernandez et al., “High-Luminosity Large Hadron Collider (HL-LHC): Technical design report”, *CERN Yellow Rep. Monogr.* **10** (2020) doi:10.23731/CYRM-2020-0010.

- [115] CMS Collaboration, “The Phase-2 upgrade of the CMS level-1 trigger”, CMS Technical Design Report CERN-LHCC-2020-004, CMS-TDR-021, 2020.
- [116] CMS Collaboration, “The Phase-2 upgrade of the CMS data acquisition and high level trigger”, CMS Technical Design Report CERN-LHCC-2021-007, CMS-TDR-022, 2021.

## A Supplementary material

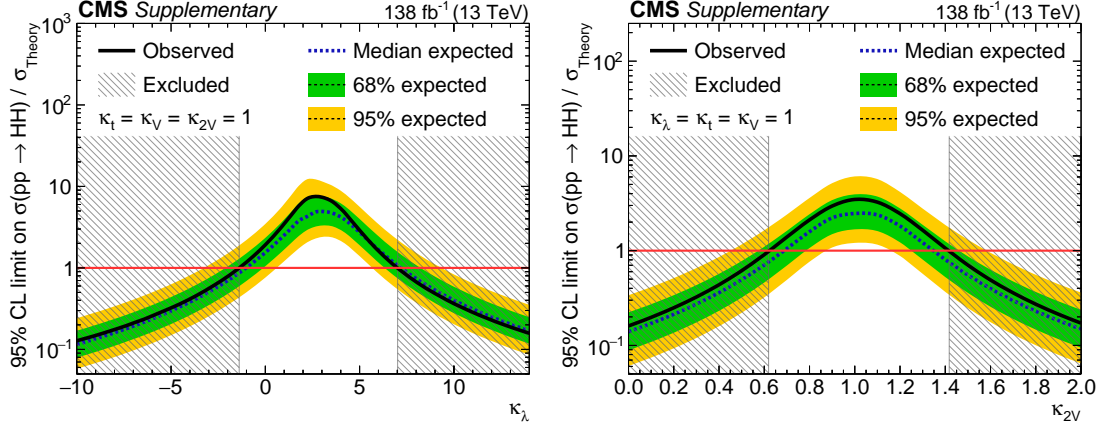


Figure A.1: The 95% CL upper limits on the inclusive HH signal strength as functions of  $\kappa_\lambda$  (left) and  $\kappa_{2V}$  (right). All other couplings are set to the values predicted by the SM. The theoretical uncertainties in the HH ggF and VBF signal cross sections are considered in this case. The inner (green) band and the outer (yellow) band indicate the 68 and 95% CL intervals, respectively, under the background-only hypothesis.

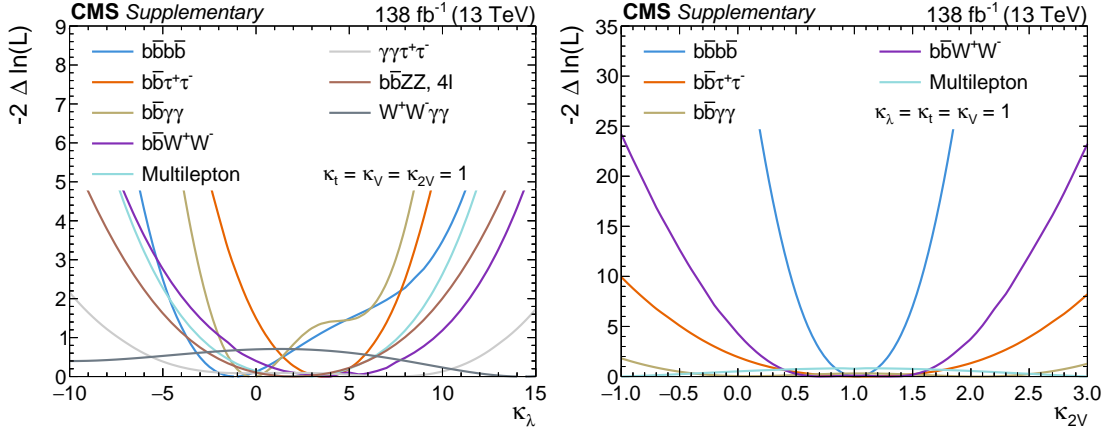


Figure A.2: The  $-2\Delta \ln(L)$  scan as functions of  $\kappa_\lambda$  (left) and  $\kappa_{2V}$  (right) for all channels, when all the other parameters are fixed to their SM value.

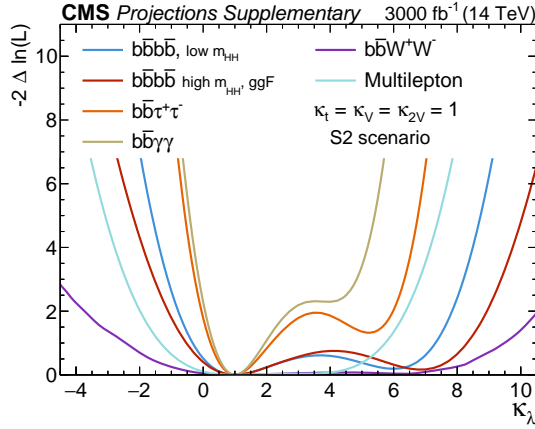


Figure A.3: The expected  $-2\Delta \ln(L)$  scan as a function of coupling modifier  $\kappa_\lambda$  for all channels and an integrated luminosity of  $3000 \text{ fb}^{-1}$ . All the other parameters are fixed to their SM values.

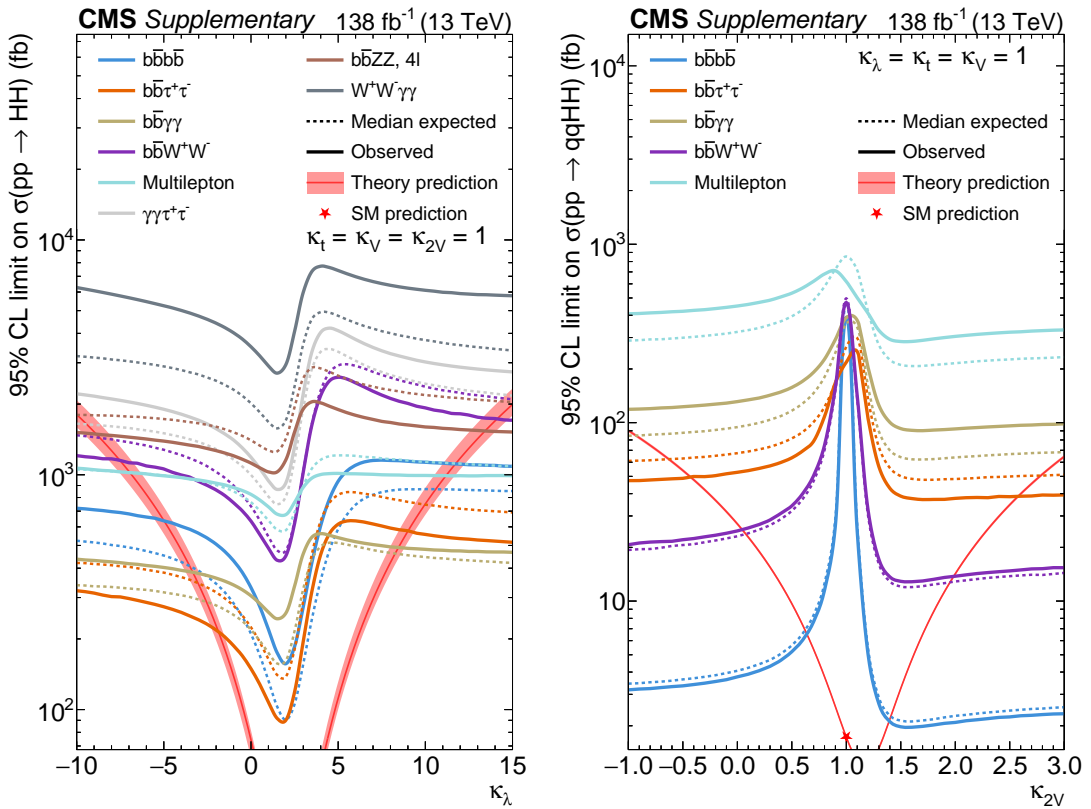


Figure A.4: The 95% CL upper limits on the inclusive (left) and VBF (right) HH cross section as functions of  $\kappa_\lambda$  and  $\kappa_{2V}$ , respectively, for all channels. All other couplings are set to the values predicted by the SM. The theoretical uncertainties in the HH ggF and VBF signal cross sections are not considered because we directly constrain the measured cross section.

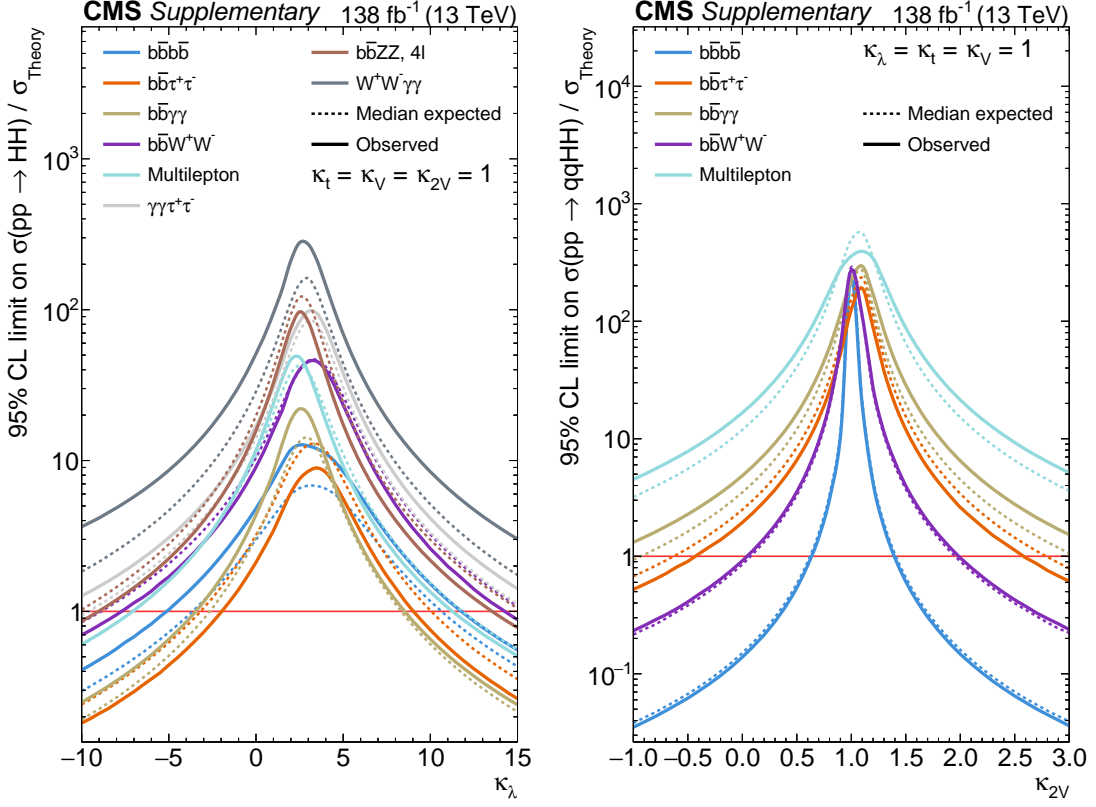


Figure A.5: The 95% CL upper limits on the inclusive (left) and VBF (right) HH signal strength as functions of  $\kappa_\lambda$  and  $\kappa_{2V}$ , respectively, for all channels. All other couplings are set to the values predicted by the SM. The theoretical uncertainties in the HH ggF and VBF signal cross sections are considered in this case.

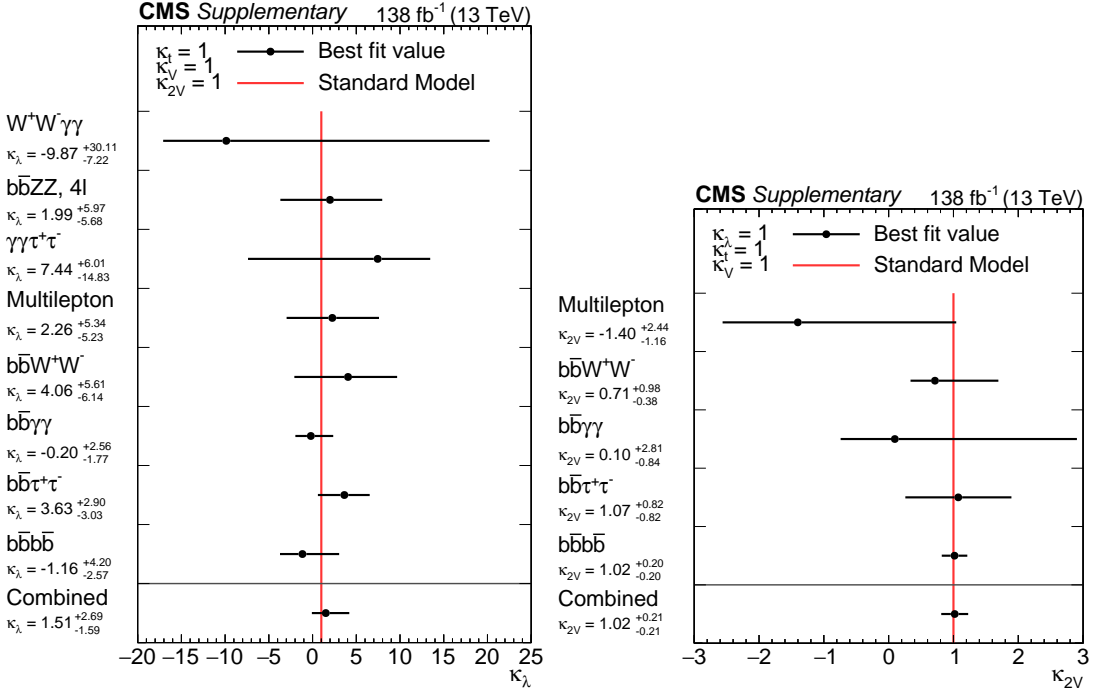


Figure A.6: The best fit value for  $\kappa_\lambda$  (left) and  $\kappa_{2V}$  (right) compared to the SM expectation for all channels and their combination, when all the other parameters are fixed to their SM values.

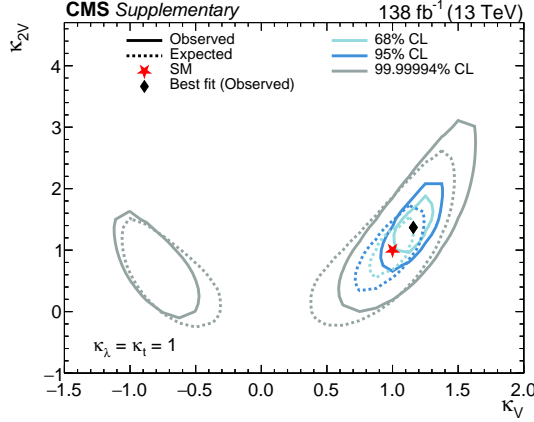


Figure A.7: The 68%, 95%, and 5 standard deviation contours of  $-2\Delta \ln(L)$  in the  $(\kappa_V, \kappa_{2V})$  plane for the combination of all channels when all the other parameters are fixed to their SM values.

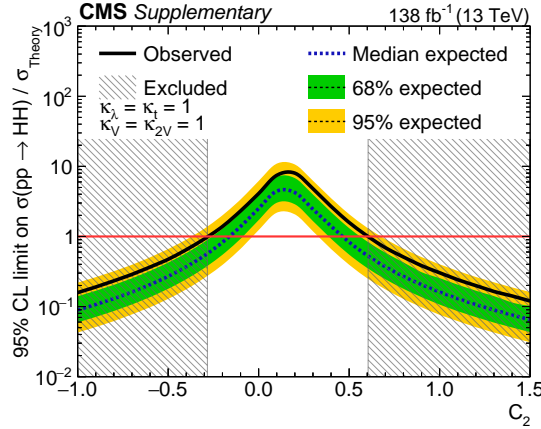


Figure A.8: The 95% CL upper limits on the inclusive HH signal strength as a function of the  $c_2$  coupling modifier. All other couplings are set to the values predicted by the SM. The theoretical uncertainties in the ggF HH signal cross sections are considered in this case. The inner (green) band and the outer (yellow) band indicate the 68 and 95% CL intervals, respectively, under the background-only hypothesis.

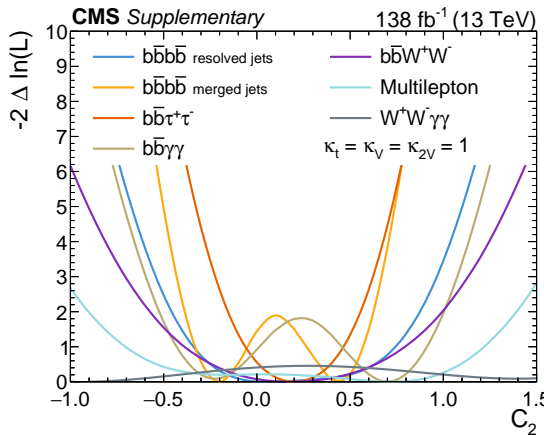


Figure A.9: The  $-2\Delta \ln(L)$  scan as a function of the  $c_2$  coupling modifier for all channels, when all the other parameters are fixed to their SM values.

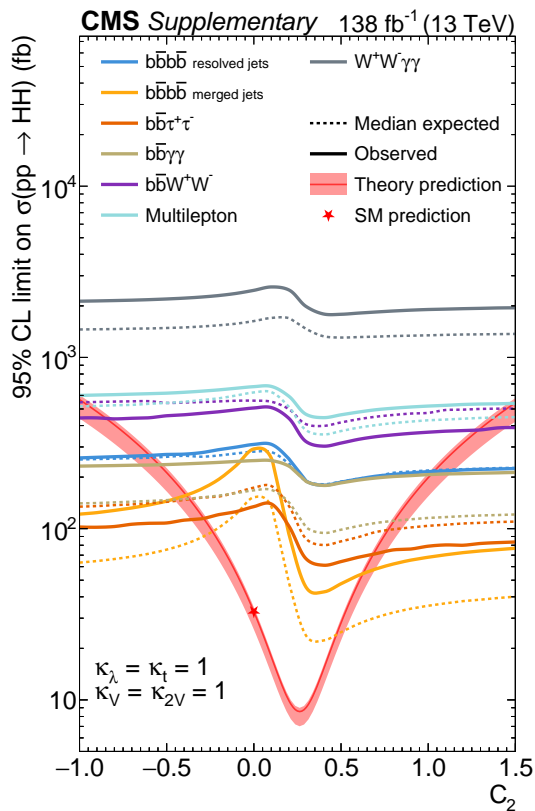


Figure A.10: The 95% CL upper limits on the inclusive HH cross section as a function of the  $c_2$  coupling modifier for all channels. All other couplings are set to the values predicted by the SM. The theoretical uncertainties in the HH ggF signal cross sections are not considered because we directly constrain the measured cross section.

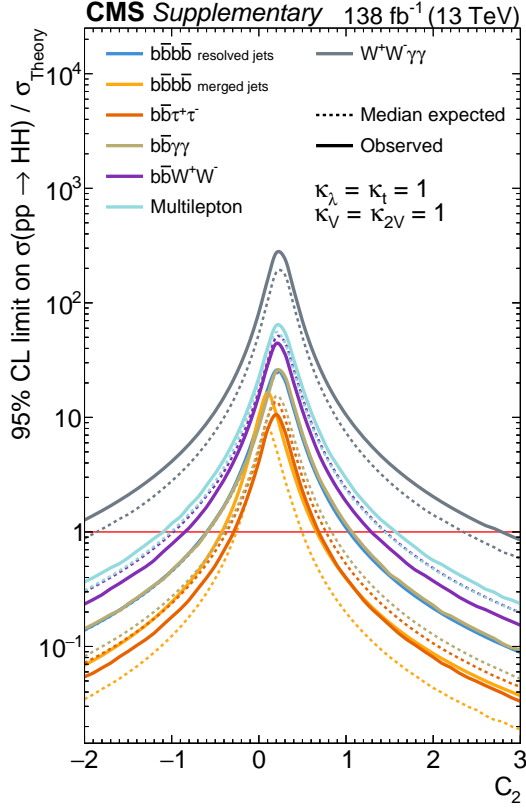


Figure A.11: The 95% CL upper limits on the HH signal strength as a function of the  $c_2$  coupling modifier for all channels. All other couplings are set to the values predicted by the SM. The theoretical uncertainties in the ggF HH signal cross sections are considered in this case.

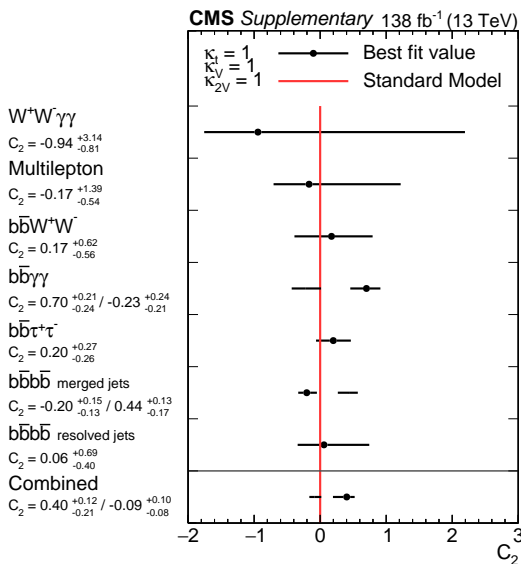


Figure A.12: The best fit value for the  $c_2$  coupling modifier compared to the SM expectation for all channels and their combination, when all the other parameters are fixed to their SM values.

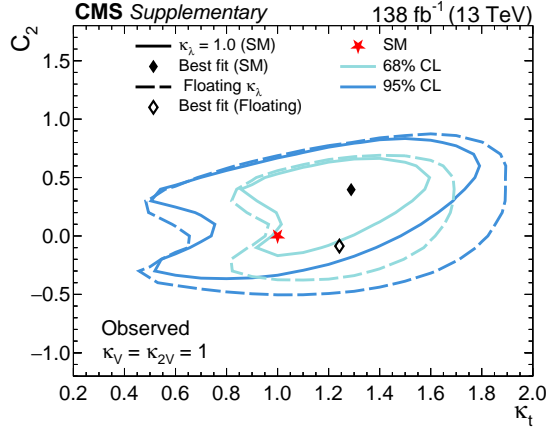


Figure A.13: The observed 68 and 95% CL contours of  $-2\Delta \ln(L)$  in the  $(c_2, \kappa_t)$  plane for the combination of all channels when  $\kappa_\lambda$  is allowed to vary. The range of  $\kappa_\lambda$  is set between  $-15$  and  $15$  to avoid unphysical areas of the phase space. All the other parameters are fixed to their SM values.

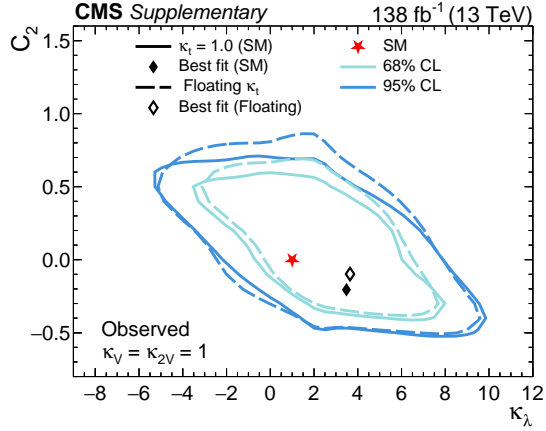


Figure A.14: The observed 68 and 95% CL contours of  $-2\Delta \ln(L)$  in the  $(c_2, \kappa_\lambda)$  plane for the combination of all channels when  $\kappa_t$  is allowed to vary. The range of  $\kappa_t$  is set between  $0.5$  and  $1.5$  to avoid unphysical areas of the phase space. All the other parameters are fixed to their SM values.

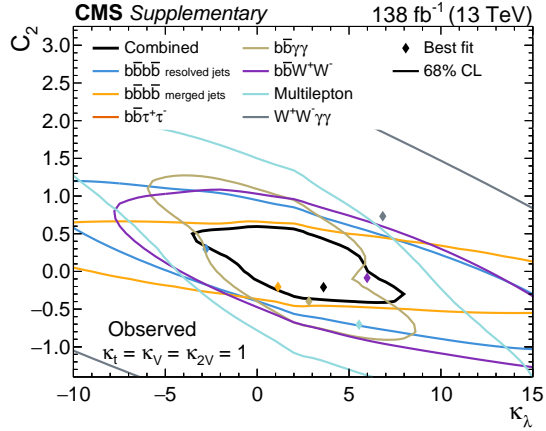


Figure A.15: The observed 68% CL contours of  $-2\Delta \ln(L)$  in the  $(c_2, \kappa_\lambda)$  plane for all channels when all the other parameters are fixed to their SM value. The best fit value and 68% CL contour for the  $b\bar{b}\tau\tau$  channel are not within the range of the figure.

Table A.1: Upper limits on the HH production cross section at 95% CL for the JHEP03(2020)91 BM1 benchmark. The theoretical uncertainties in the ggF HH signal cross section are not considered because we directly constrain the measured cross section.

Analysis	Observed [fb]	Expected [fb]	Expected $-/+68\%$ [fb]	Expected $-/+95\%$ [fb]
$b\bar{b}b\bar{b}$ resolved jets	415.43	468.75	334.27 / 664.94	250.85 / 905.55
$b\bar{b}b\bar{b}$ merged jets	72.51	37.6	25.66 / 56.78	18.51 / 84.21
$b\bar{b}\tau\tau$	146.25	188.96	129.91 / 277.85	94.48 / 392.61
$b\bar{b}\gamma\gamma$	362.99	216.8	141.93 / 336.92	99.93 / 501.86
$b\bar{b}WW$	787.14	910.16	656.67 / 1262.06	494.19 / 1679.63
multilepton	889.66	650.39	452.82 / 948.53	330.28 / 1330.46
$WW\gamma\gamma$	3137.69	2460.94	1703.91 / 3589.02	1249.69 / 5034.18
Combination	62.48	34.67	23.39 / 50.97	17.06 / 74.37

Table A.2: Upper limits on the HH production cross section at 95% CL for the JHEP03(2020)91 BM2 benchmark. The theoretical uncertainties in the HH ggF signal cross section are not considered because we directly constrain the measured cross section.

Analysis	Observed [fb]	Expected [fb]	Expected $-/+68\%$ [fb]	Expected $-/+95\%$ [fb]
$b\bar{b}b\bar{b}$ resolved jets	458.4	460.94	329.27 / 653.86	244.87 / 896.3
$b\bar{b}b\bar{b}$ merged jets	77.49	39.55	27.0 / 60.05	19.47 / 88.75
$b\bar{b}\tau\tau$	150.65	195.31	134.75 / 285.62	98.42 / 402.44
$b\bar{b}\gamma\gamma$	334.07	208.98	138.73 / 322.28	97.96 / 476.44
$b\bar{b}WW$	775.27	828.12	597.49 / 1151.62	449.65 / 1530.63
multilepton	827.61	630.86	436.8 / 920.04	320.36 / 1286.61
$WW\gamma\gamma$	3009.3	2226.56	1541.63 / 3247.21	1130.68 / 4527.21
Combination	70.48	35.64	24.68 / 53.55	18.1 / 77.97

Table A.3: Upper limits on the HH production cross section at 95% CL for the JHEP03(2020)91 BM3 benchmark. The theoretical uncertainties in the ggF HH signal cross section are not considered because we directly constrain the measured cross section.

Analysis	Observed [fb]	Expected [fb]	Expected $-/+68\%$ [fb]	Expected $-/+95\%$ [fb]
$b\bar{b}b\bar{b}$ resolved jets	167.16	189.94	135.69 / 268.68	100.91 / 366.42
$b\bar{b}b\bar{b}$ merged jets	25.99	13.18	9.48 / 20.33	6.59 / 29.9
$b\bar{b}\tau\tau$	56.04	74.22	51.03 / 109.42	37.11 / 154.84
$b\bar{b}\gamma\gamma$	175.39	90.33	58.46 / 142.54	40.58 / 215.84
$b\bar{b}WW$	281.9	351.56	253.65 / 487.49	190.89 / 646.51
multilepton	537.55	292.97	202.13 / 430.77	147.63 / 608.7
$WW\gamma\gamma$	1805.28	1238.28	851.32 / 1830.58	619.14 / 2593.94
Combination	22.94	12.21	8.27 / 18.82	6.48 / 27.11

Table A.4: Upper limits on the HH production cross section at 95% CL for the JHEP03(2020)91 BM4 benchmark. The theoretical uncertainties in the ggF HH signal cross section are not considered because we directly constrain the measured cross section.

Analysis	Observed [fb]	Expected [fb]	Expected $-/+68\%$ [fb]	Expected $-/+95\%$ [fb]
$b\bar{b}b\bar{b}$ resolved jets	185.3	199.22	142.31 / 282.6	105.83 / 384.86
$b\bar{b}b\bar{b}$ merged jets	74.53	38.57	26.03 / 57.33	18.99 / 83.57
$b\bar{b}\tau\tau$	78.63	101.56	70.32 / 148.93	51.57 / 209.52
$b\bar{b}\gamma\gamma$	211.59	122.07	80.43 / 189.7	56.27 / 282.58
$b\bar{b}WW$	370.16	464.84	334.28 / 648.28	250.58 / 866.49
multilepton	559.41	435.55	302.63 / 635.2	222.88 / 888.28
$WW\gamma\gamma$	2394.44	1441.41	990.97 / 2119.38	720.7 / 2994.8
Combination	54.28	30.76	21.34 / 45.97	14.9 / 64.55

Table A.5: Upper limits on the HH production cross section at 95% CL for the JHEP03(2020)91 BM5 benchmark. The theoretical uncertainties in the ggF HH signal cross section are not considered because we directly constrain the measured cross section.

Analysis	Observed [fb]	Expected [fb]	Expected $-/+68\%$ [fb]	Expected $-/+95\%$ [fb]
$b\bar{b}b\bar{b}$ resolved jets	155.28	170.9	121.87 / 242.43	91.46 / 330.15
$b\bar{b}b\bar{b}$ merged jets	39.62	20.02	13.66 / 30.55	10.32 / 45.24
$b\bar{b}\tau\tau$	59.63	78.12	53.9 / 114.56	39.37 / 161.17
$b\bar{b}\gamma\gamma$	177.03	94.24	61.69 / 147.58	43.44 / 221.42
$b\bar{b}WW$	284.75	360.35	259.99 / 501.12	195.66 / 666.04
multilepton	555.86	312.5	215.61 / 456.99	157.47 / 643.9
$WW\gamma\gamma$	1781.23	1160.16	797.61 / 1710.46	580.08 / 2427.49
Combination	35.3	18.07	11.95 / 26.71	8.75 / 38.62

Table A.6: Upper limits on the HH production cross section at 95% CL for the JHEP03(2020)91 BM6 benchmark. The theoretical uncertainties in the HH ggF signal cross section are not considered because we directly constrain the measured cross section.

Analysis	Observed [fb]	Expected [fb]	Expected $-/+68\%$ [fb]	Expected $-/+95\%$ [fb]
$b\bar{b}b\bar{b}$ resolved jets	251.0	267.58	191.15 / 378.5	142.15 / 516.19
$b\bar{b}b\bar{b}$ merged jets	85.91	44.43	30.2 / 66.75	22.22 / 98.53
$b\bar{b}\tau\tau$	103.7	132.81	91.96 / 194.75	67.44 / 273.17
$b\bar{b}\gamma\gamma$	252.23	152.83	100.82 / 236.29	71.64 / 350.52
$b\bar{b}WW$	479.53	572.27	411.53 / 798.09	308.49 / 1066.73
multilepton	659.53	517.58	361.6 / 754.83	264.85 / 1055.58
$WW\gamma\gamma$	2583.26	1734.38	1196.62 / 2557.06	873.96 / 3607.74
Combination	66.25	37.6	25.55 / 54.68	18.8 / 78.45

Table A.7: Upper limits on the HH production cross section at 95% CL for the JHEP03(2020)91 BM7 benchmark. The theoretical uncertainties in the HH ggF signal cross section are not considered because we directly constrain the measured cross section.

Analysis	Observed [fb]	Expected [fb]	Expected $-/+68\%$ [fb]	Expected $-/+95\%$ [fb]
$b\bar{b}b\bar{b}$ resolved jets	128.91	143.07	102.2 / 202.37	76.0 / 275.99
$b\bar{b}b\bar{b}$ merged jets	34.6	18.07	11.95 / 26.42	8.75 / 38.45
$b\bar{b}\tau\tau$	50.3	65.92	45.32 / 96.66	32.96 / 135.99
$b\bar{b}\gamma\gamma$	158.07	82.52	53.61 / 129.56	37.39 / 194.98
$b\bar{b}WW$	261.75	333.98	240.17 / 465.78	180.04 / 618.27
multilepton	525.55	280.27	194.06 / 410.98	142.33 / 578.19
$WW\gamma\gamma$	1640.12	1093.75	751.95 / 1621.28	546.88 / 2307.14
Combination	28.59	15.14	11.15 / 23.34	8.04 / 32.91

Table A.8: Upper limits on the HH production cross section at 95% CL for the JHEP04(2016)126 BM1 benchmark. The theoretical uncertainties in the HH ggF signal cross section are not considered because we directly constrain the measured cross section.

Analysis	Observed [fb]	Expected [fb]	Expected $-/+68\%$ [fb]	Expected $-/+95\%$ [fb]
$b\bar{b}b\bar{b}$ resolved jets	144.69	162.11	115.6 / 229.31	86.75 / 312.73
$b\bar{b}b\bar{b}$ merged jets	48.55	24.9	16.99 / 37.21	12.84 / 54.36
$b\bar{b}\tau\tau$	59.6	77.64	53.56 / 114.46	39.12 / 161.5
$b\bar{b}\gamma\gamma$	188.92	99.12	64.39 / 156.41	44.91 / 235.71
$b\bar{b}WW$	357.64	408.2	295.97 / 569.29	221.64 / 760.91
multilepton	468.68	353.52	246.13 / 514.16	179.52 / 720.09
$WW\gamma\gamma$	1894.82	1339.84	921.14 / 1980.72	669.92 / 2806.69
$\tau\tau\gamma\gamma$	683.75	626.95	410.44 / 984.32	288.99 / 1481.42
Combination	38.85	21.0	14.96 / 31.37	10.83 / 44.31

Table A.9: Upper limits on the HH production cross section at 95% CL for the JHEP04(2016)126 BM2 benchmark. The theoretical uncertainties in the HH ggF signal cross section are not considered because we directly constrain the measured cross section.

Analysis	Observed [fb]	Expected [fb]	Expected $-/+68\%$ [fb]	Expected $-/+95\%$ [fb]
$b\bar{b}b\bar{b}$ resolved jets	129.78	146.97	104.81 / 208.49	78.65 / 285.79
$b\bar{b}b\bar{b}$ merged jets	11.48	6.35	4.12 / 9.18	2.78 / 13.29
$b\bar{b}\tau\tau$	32.86	43.46	29.66 / 63.9	21.39 / 91.36
$b\bar{b}\gamma\gamma$	101.35	52.25	33.68 / 83.48	23.27 / 127.66
$b\bar{b}WW$	171.98	198.24	143.27 / 274.89	106.86 / 364.56
multilepton	204.62	158.69	108.71 / 235.23	78.73 / 335.71
$WW\gamma\gamma$	1240.76	929.69	636.89 / 1381.79	461.21 / 1974.57
$\tau\tau\gamma\gamma$	461.27	431.64	282.58 / 677.68	198.96 / 1019.92
Combination	10.45	5.37	3.9 / 8.45	3.02 / 11.9

Table A.10: Upper limits on the HH production cross section at 95% CL for the JHEP04(2016)126 BM3 benchmark. The theoretical uncertainties in the HH ggF signal cross section are not considered because we directly constrain the measured cross section.

Analysis	Observed [fb]	Expected [fb]	Expected $-/+68\%$ [fb]	Expected $-/+95\%$ [fb]
$b\bar{b}b\bar{b}$ resolved jets	195.41	204.1	146.29 / 289.53	109.23 / 396.88
$b\bar{b}b\bar{b}$ merged jets	85.84	43.46	29.88 / 65.28	21.73 / 95.32
$b\bar{b}\tau\tau$	82.28	106.45	73.7 / 156.09	54.05 / 218.94
$b\bar{b}\gamma\gamma$	216.47	126.46	83.64 / 196.53	58.79 / 292.02
$b\bar{b}WW$	350.21	480.47	347.24 / 670.07	259.0 / 895.62
multilepton	562.38	449.22	312.13 / 655.14	229.87 / 913.38
$WW\gamma\gamma$	2053.45	1507.81	1040.3 / 2223.03	759.8 / 3136.46
$\tau\tau\gamma\gamma$	738.4	662.11	435.12 / 1034.24	307.78 / 1562.05
Combination	60.49	34.67	24.0 / 50.42	17.6 / 71.48

Table A.11: Upper limits on the HH production cross section at 95% CL for the JHEP04(2016)126 BM4 benchmark. The theoretical uncertainties in the HH ggF signal cross section are not considered because we directly constrain the measured cross section.

Analysis	Observed [fb]	Expected [fb]	Expected $-/+68\%$ [fb]	Expected $-/+95\%$ [fb]
$b\bar{b}b\bar{b}$ resolved jets	265.75	278.32	198.82 / 394.81	147.86 / 541.2
$b\bar{b}b\bar{b}$ merged jets	177.25	91.31	63.0 / 136.8	46.01 / 198.98
$b\bar{b}\tau\tau$	122.23	153.81	106.49 / 224.93	78.11 / 315.02
$b\bar{b}\gamma\gamma$	267.77	172.36	114.42 / 265.11	80.8 / 390.58
$b\bar{b}WW$	585.6	619.14	445.23 / 863.46	333.76 / 1154.11
multilepton	677.65	599.61	418.91 / 869.69	306.83 / 1212.4
$WW\gamma\gamma$	2663.19	1890.62	1304.42 / 2772.35	952.7 / 3900.26
$\tau\tau\gamma\gamma$	948.48	839.84	555.43 / 1311.86	390.4 / 1961.96
Combination	108.41	62.01	43.41 / 89.2	31.49 / 124.52

Table A.12: Upper limits on the HH production cross section at 95% CL for the JHEP04(2016)126 BM5 benchmark. The theoretical uncertainties in the HH ggF signal cross section are not considered because we directly constrain the measured cross section.

Analysis	Observed [fb]	Expected [fb]	Expected $-/+68\%$ [fb]	Expected $-/+95\%$ [fb]
$b\bar{b}b\bar{b}$ resolved jets	143.19	161.62	115.25 / 229.27	86.49 / 312.23
$b\bar{b}b\bar{b}$ merged jets	24.86	13.18	8.37 / 19.49	6.18 / 28.18
$b\bar{b}\tau\tau$	49.4	65.92	45.32 / 96.66	32.96 / 136.8
$b\bar{b}\gamma\gamma$	156.84	80.57	52.14 / 126.81	36.19 / 192.36
$b\bar{b}WW$	252.93	318.36	229.7 / 441.45	172.86 / 587.51
multilepton	439.15	262.7	181.24 / 386.25	132.37 / 545.8
$WW\gamma\gamma$	1541.96	1109.38	762.7 / 1644.44	554.69 / 2340.09
$\tau\tau\gamma\gamma$	586.92	533.2	349.07 / 832.88	245.77 / 1257.94
Combination	22.15	11.23	8.27 / 17.32	5.97 / 25.47

Table A.13: Upper limits on the HH production cross section at 95% CL for the JHEP04(2016)126 BM6 benchmark. The theoretical uncertainties in the HH ggF signal cross section are not considered because we directly constrain the measured cross section.

Analysis	Observed [fb]	Expected [fb]	Expected $-/+68\%$ [fb]	Expected $-/+95\%$ [fb]
$b\bar{b}b\bar{b}$ resolved jets	253.42	274.41	195.69 / 389.27	146.85 / 530.13
$b\bar{b}b\bar{b}$ merged jets	100.46	51.76	35.18 / 77.75	25.88 / 112.9
$b\bar{b}\tau\tau$	112.05	145.02	100.05 / 212.65	73.08 / 299.17
$b\bar{b}\gamma\gamma$	299.11	176.76	116.46 / 275.4	81.47 / 410.54
$b\bar{b}WW$	607.27	675.78	485.97 / 942.46	364.29 / 1259.69
multilepton	740.39	583.98	405.77 / 849.35	298.84 / 1185.92
$WW\gamma\gamma$	2841.96	2085.94	1439.17 / 3058.75	1051.12 / 4303.18
$\tau\tau\gamma\gamma$	1118.94	1015.62	669.17 / 1590.49	468.14 / 2397.94
Combination	76.13	42.48	29.74 / 62.46	21.57 / 88.78

Table A.14: Upper limits on the HH production cross section at 95% CL for the JHEP04(2016)126 BM7 benchmark. The theoretical uncertainties in the HH ggF signal cross section are not considered because we directly constrain the measured cross section.

Analysis	Observed [fb]	Expected [fb]	Expected $-/+68\%$ [fb]	Expected $-/+95\%$ [fb]
$b\bar{b}b\bar{b}$ resolved jets	1154.73	1156.25	821.74 / 1644.79	614.26 / 2266.09
$b\bar{b}b\bar{b}$ merged jets	675.53	344.73	237.0 / 516.49	172.36 / 755.37
$b\bar{b}\tau\tau$	537.5	619.14	431.06 / 902.95	314.41 / 1266.54
$b\bar{b}\gamma\gamma$	528.29	449.22	306.64 / 673.04	221.1 / 968.1
$b\bar{b}WW$	2447.17	2234.38	1606.78 / 3116.1	1204.47 / 4164.99
multilepton	1087.9	1160.16	816.12 / 1664.22	602.74 / 2297.57
$WW\gamma\gamma$	4653.42	3546.88	2503.64 / 5102.05	1856.57 / 7033.55
$\tau\tau\gamma\gamma$	2853.68	2437.5	1618.06 / 3778.31	1142.58 / 5637.78
Combination	326.77	213.87	149.93 / 308.49	110.28 / 430.01

Table A.15: Upper limits on the HH production cross section at 95% CL for the JHEP04(2016)126 BM8 benchmark. The theoretical uncertainties in the HH ggF signal cross section are not considered because we directly constrain the measured cross section.

Analysis	Observed [fb]	Expected [fb]	Expected $-/+68\%$ [fb]	Expected $-/+95\%$ [fb]
$b\bar{b}b\bar{b}$ resolved jets	156.42	174.8	124.65 / 247.97	93.55 / 337.7
$b\bar{b}b\bar{b}$ merged jets	42.29	21.97	14.89 / 32.83	10.64 / 48.23
$b\bar{b}\tau\tau$	61.37	80.08	55.56 / 117.74	40.35 / 165.4
$b\bar{b}\gamma\gamma$	181.29	97.17	63.61 / 152.17	44.79 / 228.3
$b\bar{b}WW$	317.11	386.72	279.02 / 539.32	209.98 / 715.89
multilepton	495.07	334.96	232.74 / 488.51	171.41 / 685.21
$WW\gamma\gamma$	1893.77	1230.47	845.95 / 1814.13	615.23 / 2574.61
$\tau\tau\gamma\gamma$	620.95	564.45	369.53 / 881.69	260.18 / 1331.66
Combination	35.98	19.04	12.99 / 28.46	9.82 / 40.88

Table A.16: Upper limits on the HH production cross section at 95% CL for the JHEP04(2016)126 BM8a benchmark. The theoretical uncertainties in the HH ggF signal cross section are not considered because we directly constrain the measured cross section.

Analysis	Observed [fb]	Expected [fb]	Expected $-/+68\%$ [fb]	Expected $-/+95\%$ [fb]
$b\bar{b}b\bar{b}$ resolved jets	159.9	179.2	127.79 / 254.2	95.9 / 346.19
$b\bar{b}b\bar{b}$ merged jets	55.29	28.81	19.99 / 43.05	13.95 / 62.19
$b\bar{b}\tau\tau$	62.93	81.54	56.46 / 120.22	41.41 / 169.62
$b\bar{b}\gamma\gamma$	191.66	103.52	67.51 / 162.11	47.31 / 244.41
$b\bar{b}WW$	342.36	412.11	296.35 / 571.45	222.15 / 760.52
multilepton	608.09	352.54	245.45 / 515.55	179.02 / 722.05
$WW\gamma\gamma$	1854.52	1351.56	929.2 / 1992.66	675.78 / 2827.98
$\tau\tau\gamma\gamma$	677.86	619.14	407.94 / 969.59	285.39 / 1461.82
Combination	44.25	23.93	16.32 / 34.99	12.34 / 49.45

Table A.17: Upper limits on the HH production cross section at 95% CL for the JHEP04(2016)126 BM9 benchmark. The theoretical uncertainties in the HH ggF signal cross section are not considered because we directly constrain the measured cross section.

Analysis	Observed [fb]	Expected [fb]	Expected $-/+68\%$ [fb]	Expected $-/+95\%$ [fb]
$b\bar{b}b\bar{b}$ resolved jets	140.98	155.76	111.27 / 220.95	82.75 / 300.91
$b\bar{b}b\bar{b}$ merged jets	36.6	19.04	12.91 / 28.46	9.22 / 41.8
$b\bar{b}\tau\tau$	53.85	70.8	48.68 / 103.82	35.4 / 146.06
$b\bar{b}\gamma\gamma$	167.12	88.38	57.42 / 138.4	40.05 / 208.67
$b\bar{b}WW$	284.46	357.42	257.88 / 497.04	194.07 / 660.63
multilepton	540.83	297.85	206.23 / 436.76	151.25 / 614.45
$WW\gamma\gamma$	1790.22	1167.97	802.98 / 1731.29	583.98 / 2449.47
$\tau\tau\gamma\gamma$	586.01	535.16	352.6 / 838.06	246.67 / 1263.53
Combination	31.4	16.11	11.72 / 24.59	8.31 / 34.89

Table A.18: Upper limits on the HH production cross section at 95% CL for the JHEP04(2016)126 BM10 benchmark. The theoretical uncertainties in the HH ggF signal cross section are not considered because we directly constrain the measured cross section.

Analysis	Observed [fb]	Expected [fb]	Expected $-/+68\%$ [fb]	Expected $-/+95\%$ [fb]
$b\bar{b}b\bar{b}$ resolved jets	543.52	603.52	430.37 / 856.11	322.98 / 1173.55
$b\bar{b}b\bar{b}$ merged jets	145.61	75.68	51.74 / 112.79	37.84 / 164.59
$b\bar{b}\tau\tau$	207.82	263.67	181.27 / 388.74	131.84 / 550.09
$b\bar{b}\gamma\gamma$	458.7	297.85	196.98 / 460.5	138.45 / 681.37
$b\bar{b}WW$	1286.37	1441.41	1039.97 / 1998.72	782.64 / 2660.01
multilepton	989.32	855.47	596.49 / 1247.61	441.1 / 1739.4
$WW\gamma\gamma$	3944.23	3171.88	2223.64 / 4587.92	1635.5 / 6346.12
$\tau\tau\gamma\gamma$	2251.15	2015.62	1324.6 / 3148.47	936.95 / 4708.71
Combination	112.78	64.94	45.46 / 96.0	32.98 / 136.83

Table A.19: Upper limits on the HH production cross section at 95% CL for the JHEP04(2016)126 BM11 benchmark. The theoretical uncertainties in the HH ggF signal cross section are not considered because we directly constrain the measured cross section.

Analysis	Observed [fb]	Expected [fb]	Expected $-/+68\%$ [fb]	Expected $-/+95\%$ [fb]
$b\bar{b}b\bar{b}$ resolved jets	336.07	367.19	261.84 / 520.87	196.5 / 709.35
$b\bar{b}b\bar{b}$ merged jets	68.5	35.64	24.05 / 53.26	17.54 / 78.67
$b\bar{b}\tau\tau$	120.66	156.74	108.14 / 230.46	78.98 / 325.65
$b\bar{b}\gamma\gamma$	315.53	184.08	120.51 / 286.07	84.85 / 427.2
$b\bar{b}WW$	672.8	744.14	536.89 / 1031.86	404.05 / 1373.26
multilepton	793.05	572.27	398.43 / 834.59	290.6 / 1170.65
$WW\gamma\gamma$	2748.0	2148.44	1487.54 / 3150.4	1091.0 / 4405.69
$\tau\tau\gamma\gamma$	1204.53	1082.03	712.92 / 1690.17	498.75 / 2527.74
Combination	58.28	31.74	21.82 / 47.17	15.87 / 68.37

Table A.20: Upper limits on the HH production cross section at 95% CL for the JHEP04(2016)126 BM12 benchmark. The theoretical uncertainties in the HH ggF signal cross section are not considered because we directly constrain the measured cross section.

Analysis	Observed [fb]	Expected [fb]	Expected $-/+68\%$ [fb]	Expected $-/+95\%$ [fb]
bbbb resolved jets	571.6	544.92	389.27 / 775.16	289.49 / 1061.08
b $\bar{b}$ b $\bar{b}$ merged jets	560.66	284.18	195.37 / 424.64	142.09 / 618.64
b $\bar{b}$ $\tau\tau$	257.3	310.55	216.21 / 452.9	157.7 / 635.27
b $\bar{b}$ $\gamma\gamma$	380.51	288.09	193.84 / 438.52	137.29 / 638.47
b $\bar{b}$ WW	1216.94	1082.03	778.11 / 1509.02	583.28 / 2030.88
multilepton	896.73	898.44	629.85 / 1295.95	463.26 / 1800.82
WW $\gamma\gamma$	3890.59	2742.19	1905.34 / 3977.33	1403.23 / 5527.62
$\tau\tau\gamma\gamma$	1559.83	1359.38	896.74 / 2112.55	637.21 / 3170.48
Combination	214.08	140.62	98.59 / 202.84	72.51 / 280.99

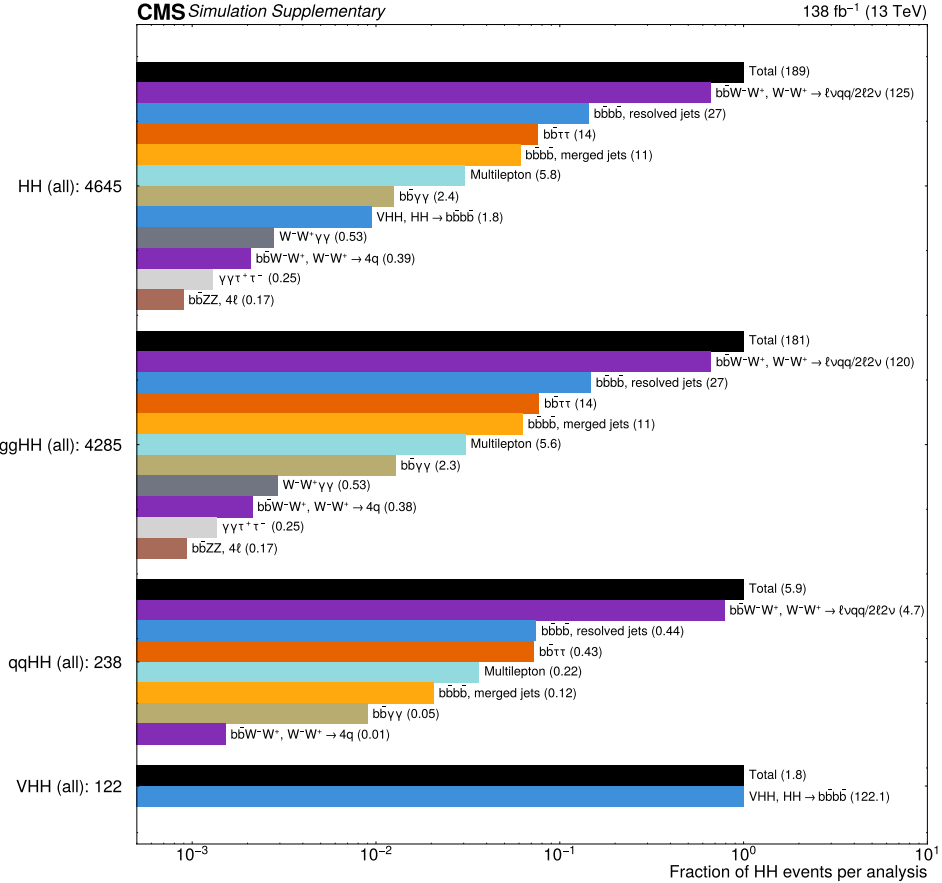


Figure A.16: A bar chart showing the fraction of all HH events that are selected in each analysis. The numbers shown, correspond to the total of selected events per analysis. The results are calculated inclusively and per production mode.

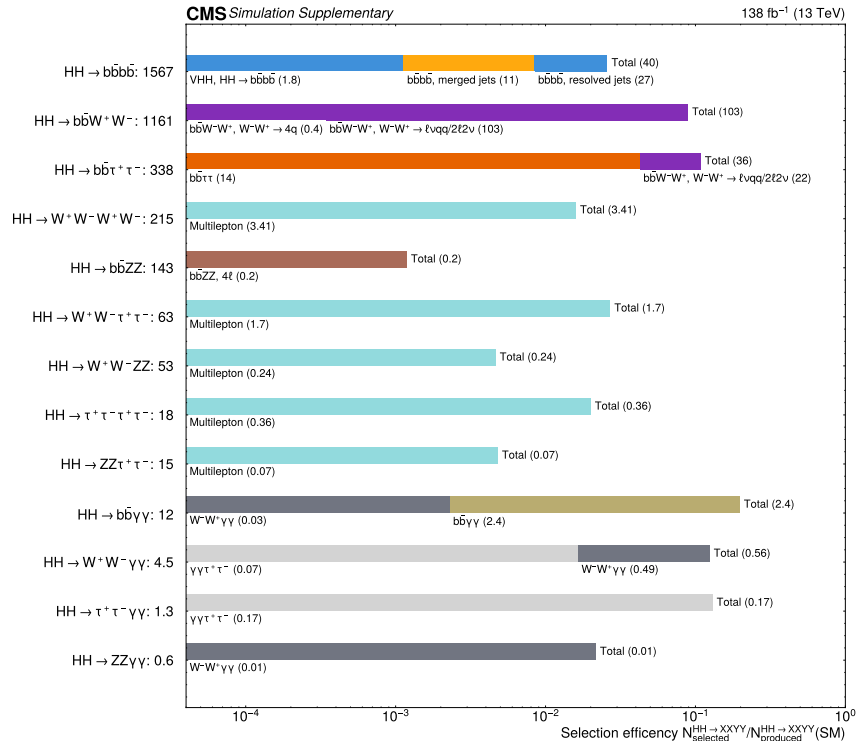


Figure A.17: A bar chart showing the selection efficiency for the HH signal per channel. The number of selected events per channel is also shown.